**Title**

Rational design of efficient and durable Pt-based electrocatalysts for fuel cells



**Author**

Peng, Bosi

**Publication Date**

2022

Peer reviewed|Thesis/dissertation

UNIVERSITY OF CALIFORNIA

Los Angeles

# Rational design of efficient and durable Pt-based electrocatalysts for fuel cells

A dissertation submitted in partial satisfaction of the requirements

for the degree Doctor of Philosophy in Chemistry

by

Bosi Peng

2022

ABSTRACT OF THE DISSERTATION

Rational design of efficient and durable Pt-based electrocatalysts for fuel cells

by

Bosi Peng

Doctor of Philosophy in Chemistry

University of California, Los Angeles, 2022

Professor Xiangfeng Duan, Co-Chair

Professor Yu Huang, Co-Chair

Proton exchange membrane fuel cells (PEMFCs) offer an attractive zero-emission power generation technology to realize a carbon-neutral future. However, the competitiveness of fuel cell technology is currently constrained by the high cost of precious metal. To this end, advanced nanocatalysts are developed with improved catalytic activity, which promise a considerable reduction of precious metal loading, but they are typically plagued by a well-acknowledged trade-off between activity and durability. As fuel cells must meet performance requirements throughout their service lifetime, the end-of-life performance ultimately determines the amount of Pt needed

and impacts the total system cost. Therefore, my research aims to develop durable, high-performance, and cost-effective fuel cell catalysts and validates their performance in the membrane electrode assembly (MEA) to pave the way for the widespread adoption of fuel cell applications.

In Chapter 2, I developed a facile molecular surface modification approach using dimethylformamide (DMF) to improve the ORR performance of Pt-based catalysts successfully. The prevailing Sabatier plot has been applied to modulate electrocatalytic activity through structural and compositional engineering, which predicted optimum binding energy for the highest ORR activity point. Nevertheless, the catalyst-electrolyte interface can influence the microkinetic of the physisorption/desorption process, which could further upper the abovementioned activity limitation. However, this effect has not yet been sufficiently explored. We found that DMF could work as a surface molecular pump to facilitate the entrapment of oxygen and outflux of the water by disrupting the interfacial water network, which led to enhanced ORR kinetics. This strategy can also be applied to Pt alloy catalysts: we demonstrated an optimal model PtCuNi catalyst with an unprecedented specific activity of 21.8 $mA/cm^2$, nearly double the previous record. Building on the previous rotating disk electrode studies in our group, many highly promising ORR catalysts were developed, but not all promising RDE ORR activity results have translated to real-world MEA performance. In my second project (Chapter 3), I developed an ultralow Pt loading and high-performance MEA using PtCo nanowires (PtCoNWs) as cathode catalysts. The PtCoNWs achieved an unprecedented mass activity (MA) of 1.06 $A/mg_{Pt}$, far surpassing the Department of Energy target. Chapter 4 shifted the focus of catalyst design from the delicate shape-controlled nanocatalyst to more stable catalysts with practical potential. The ever-increasing attention to heavy-duty applications of fuel cells has exacerbated the challenge in catalyst durability. In this project, I presented a unique design of ultrafine Pt nanocatalysts with embedded

cobalt oxide clusters, which exploits the strong Pt/oxide interaction. This design grants exceptional structural and chemical durability without sacrificing activity. The developed nanocatalyst delivers an outstanding initial mass activity of 1.10 $A/mg_{Pt}$, a rated power density of 1.04 $W/cm^2$. It exhibits exceptional durability featuring a MA retention of 88.2%, an ultrasmall rated power loss of 7.5% after the accelerated durability test.

During my PhD studies, I have explored new catalyst design strategies and translated understanding in fundamental RDE studies to better improve catalyst performance in practical fuel cells. These works can offer new thinking in material design which can attract interest from diverse fields.

The dissertation of Bosi Peng is approved.

Richard B. Kaner

Chong Liu

Jeffrey I. Zink

Yu Huang, Committee Co-Chair

Xiangfeng Duan, Committee Co-Chair

University of California, Los Angeles

2022

# DEDICATION

*I dedicate this thesis to my mom Chun Wu, and dad Tianyou Peng*

*for supporting me along the way, for their unconditional love.*

# Table of Contents

# List of Figures

# List of Tables

# Acknowledgments

My past five years at UCLA have been filled with excitement, pride, frustration, and everything in-between. I am so lucky to have many people who helped me get through it and made my Ph.D. journey memorable. First, I would like to thank my advisor, Dr. Xiangfeng Duan, for his help and instructions. I have always been impressed by his profound knowledge and keen insight or even instinct to always ask those critical questions and find interesting scientific problems. I admire his passion and enthusiasm for exploring new ideas, and his persistence in bringing those ideas into reality. Another person who has had a huge impact on my Ph.D life is Dr. Yu Huang from MSE department, I have actually spent most of my time working in her lab. She is a very supportive mentor who cares about not only every detail of my projects, but also my career development. Their passion and enthusiasm for transformative new findings and their rigorous attitude and great taste of science with high standards have profoundly benefited me and allowed me to perform all the works presented in this thesis. I especially appreciate the freedom and support they offered me to explore, which really helped me to learn and grow into an independent researcher. It has been a real privilege to join their lab and learn from their great mind.

I would like to thank the members serving on my committee for their time and advice. I am fortunate to have taken the courses they taught. Prof. Chong Liu, who taught me the basics of electrochemistry in my first year, his course is helpful as I came in with little experience in electrochemistry. He is not only an amazing teacher, but also he is a mentor who cares about a student's personal development. I appreciate his encouragement and advice when I was so depressed and had difficulties adjusting to graduate school. Prof. Kaner's solid-state chemistry course is intriguing and eye-opening for me. I enjoyed his teaching style and his humor, and I appreciate him for being approachable and supportive. Prof. Jeffrey Zink's group theory was a fantastic but pretty challenging journey for me. I admired his sharp mind and enthusiasm for fundamental problems and connecting

them to applications. Also, I would like to thank Prof. Sarah Tolbert for holding the MCTP. It was a rewarding journey, where she taught us how to propose and start a new project. She also taught me how to give a presentation and pay attention to details in slides, which are invaluable skills.

I would like to thank Prof. Johnny Pang for being so organized and well-prepared as an instructor. It was an absolute pleasure to work with him and I love him as a person. He is thoughtful and caring and always generous in expressing appreciation for my work. He always has a warm smile whenever we meet, and I found his smile like sunshine that could lighten up my day. I would also thank Dr. Ignacio Martini for his help and support in training and maintenance of instruments in MIC. He likes to check on me to see if I need anything while working on XPS. He is very responsible and warm-hearted under a seemingly cold face, and I feel I could always turn to him whenever I need help.

Over the years, I have benefited from many former and current group members. First, I would like to thank Dr. Zipeng Zhao, Zeyan Liu, and Dr. Jin Huang for generously offering help in instrument training and experiences in synthesis and electrochemistry when I joined the group and started new projects. They not only offered help and guidance in the lab but also cared about me in life. They gave me invaluable advice and help on both my life and career in grad-school, especially during those darkest days in my life. I would like to thank Zeyan Liu and Dr. Jin Huang for their close collaboration on my projects. I always enjoyed working with them. We supported each other and had great times together no matter how frustrating life/work was. I would also like to thank those group members that I have not directly worked with, but we had a great time together. Dr. Jingyuan Zhou is a very persistent scientist and also a creative cute lady, I admire her for being young at heart and having a great passion for both life and work. Dr. Zhaoyang Lin, Dr. Lele Peng and Dr. Enbo Zhu are reliable seniors in the group, it is always a joy to chat with them. Zhaoyang and Lele shared many life experiences with me, and they always tried to cheer me up when I was sad. Lele also instructed me on the synthesis of graphene and even offered help remotely when he was back in China. Enbo has a good sense of humor, and he can always bring laughter into our office. Dr. Haotian Liu, Jin Cai, Dr. Guangyan Zhong, Dong

Xu, Dr. Peiqi Wang, we had great fun both in and outside the lab. I would like to thank them for hosting and organizing our get-togethers, I have learned many new games during those parties.

Outside my group, I have come across many great friends and my time at UCLA wouldn't have been so colorful without them. I want to thank my friends from the 2017 cohort, Jiahui Lu, Yao Gong, Joe Mazetti, Chengxiang Wang, Xun Guan, Wenfei Liu. We took classes together and always supported each other through these years. I would like to thank my dear friend Jiahui and Yao for their close company, I enjoyed our fun conversations and trips, and those times we spend together (especially when we hung out or went shopping). Joe and I have been good friends ever since MCTP. He is a great partner and even a better friend. I appreciate him being so supportive and inspiring. We are so comfortable together that we can never run out of things to talk about. I also want to thank Dr. Zhiyu Liu, we knew each other when we were undergraduates. He offered tremendous help during these years, especially when I first moved to LA and tried to adopt to the new environment. I would also like to express my gratitude to all my old friends, who are always there to talk and share joys and sorrows in our life, despite distance or time difference between us.

A special acknowledgment goes to my collaborators, who are professional and talented scientists worldwide. I enjoyed working with them, and their contributions are essential to my work. Dr. Qingying Jia from Northeastern University offered tremendous help in helping me analyze and understand XAS data. I would like to thank Dr. Alessandro Fortunelli and his colleagues Dr. Luca Sementa from the Italian national research council, Prof. Hendrik Heinz, and his postdoc Dr. Cheng Zhu from the University of Colorado Boulder for their help and insight into simulation work, and Dr. Mingjie Xu from the University of California, Irvine for his help in JEOL Grand ARM EM training.

The deepest appreciation goes to my parents, Chun Wu and Tianyou Peng. Their deep love and encouragement throughout my entire life are definitely my motivation to achieve our goals. I'd like to thank Zeyan for being my biggest supporter and best partner, I can't wait to see where our future takes us. I would also like to thank my four-legged friend Berber, he has filled my life with laughter and joy.

Chapter 2 is a version of [Submitted manuscript] Author list: Jin Huang, Bosi Peng (co-first), Cheng Zhu, Mingjie Xu, Zeyan Liu, Rui Wang, Denis Leshchev, Yang Liu, Xiangfeng Duan, Qingying Jia, Hendrik Heinz, Yu Huang

Chapter 3 is a version of *Science China Materials,* Author list: Jin Huang, Bosi Peng (co-first), Thomas Stracensky, Zeyan Liu, Ao Zhang, Mingjie Xu, Yang Liu, Zipeng Zhao, Xiangfeng Duan, Qingying Jia, and Yu Huang.

Chapter 4 is a version of [submitted manuscript] Author list: Bosi Peng, Zeyan Liu, Luca Sementa, Qiang Sun, Qingying Jia, Zipeng Zhao, Jin Huang, Mingjie Xu, Alessandro Fortunelli, Xiangfeng Duan, Yu Huang

# VITA

| | |
|---|---|
| 2017 | B.S. in Chemistry, Wuhan University, Wuhan, China |
| 2017 | UCLA University Fellowship |
| 2019 | Advanced to Candidacy, UCLA |
| 2021 | John Alan Walker Excellence in Research Award |
| 2021 | Michael E. Jung Excellence in Teaching Award |

# Chapter 1. Introduction

## 1.1 Background and Impact of Fuel Cell

Energy crisis and climate change are the imminent challenges that demand instant solutions in replacing fossil fuels with alternative clean energy sources. The development of renewable energy has provided a huge potential to address the challenges, which is a game-changer to a sustainable energy future. Hydrogen is one of the most promising energy carriers in a sustainable economy. Proton-exchange membrane fuel cells (PEMFCs), which convert the chemical energy of hydrogen to electricity (Figure 1. 1), represent one of the most attractive and sustainable power generation technologies in all sectors given its benefits, including zero-emission, high efficiency, high power density, and reduced fossil fuel consumption.[1-4] Hydrogen-powered fuel cells are not only pollution-free but also have more than two times the efficiency of traditional combustion technologies. Recently, Toyota released the second generation of Toyota Mirai, which can achieve a maximum driving mileage of 402 miles with only 5 minutes of refueling. Obviously, PEMFC vehicles show considerable advantages with shorter refuel time and more extended driving range due to the intrinsic high mass-specific energy of hydrogen as the energy carrier compared to the most commercialized battery electrical vehicles (BEVs).[4]

The principle of a hydrogen fuel cell is illustrated in Figure 1.1. The hydrogen fuel is fed and oxidized at the anode, generating protons. The protons then transport through the proton-exchange membrane and react with oxygen to form water, and electricity is generated in the meantime. However, the cathode oxygen reduction reaction (ORR), as the rate-determining step (RDS), significantly slows down the overall reaction kinetics. Therefore, to accelerate sluggish ORR, a large amount of platinum-group metals (PGM) is required, which limits the spread of PEMFCs. As the Pt-based catalyst cost is projected to account for more than 40% of the fuel cell

stack cost even at high production volume,[5] it is vital to improving the mass activity (MA) of Pt (the catalytic activity per unit mass of Pt). Moreover, the Pt loading, activity and durability of PEMFEC catalysts often display an intrinsic trade-off relationship and are difficult to meet the targets simultaneously. In specific, if Pt usage is reduced, obviously the power performance would decrease due to less active Pt area as catalytic sites. Also, durability problems are exacerbated when Pt is at low loading. These challenges have motivated immense efforts to improve both the mass specific catalytic activity and durability.

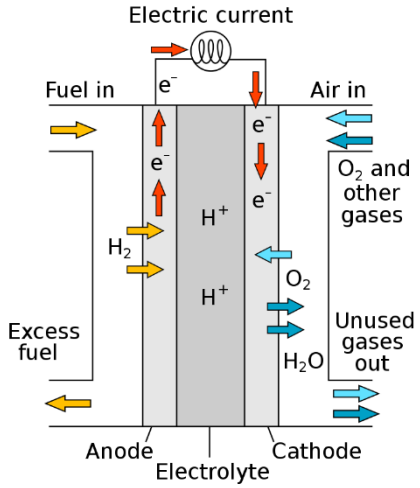


**Figure 1. 1** The schematic diagram and working principle of proton-exchange membrane fuel cells (PEMFCs). Adapted from https://en.wikipedia.org/wiki/Fuel_cell.

### 1.2 Catalysis Design Strategies in Improving Oxygen Reduction Reaction Kinetics

Fundamentally, MA is defined as the product of the electrochemically active surface area (ECSA) and specific activity (SA). The ECSA of catalysts is related to the nanostructures and morphologies, or the surface-to-volume ratio. Higher the ECSA, larger the active Pt area. As the oxygen transport resistance is inversely proportional to the active Pt area, it is desirable to design catalysts with ultrahigh ECSA. Meanwhile, the SA is defined as activity per unit active area, which is known as the intrinsic activity of catalysts. High SA reflects the optimum adsorption behavior

of reaction intermediates at catalytic sites, which can be tuned by electronic structure of catalysts. Enhancing intrinsic activity requires a thorough understanding of reaction mechanisms.

In the past decades, extensive investigation has been devoted experimentally and computationally to uncover the ORR mechanism.[2, 6-9] In general, oxygen is reduced to water involving four protons and four electrons pathway $[O_2 + 4(H^+ + e^-) \rightarrow 2H_2O]$.[10] The $O_2$ can either be directly reduced to $H_2O$ through a direct four-electron pathway or through an indirect two-electron reduction pathway in which $O_2$ reduces to hydrogen peroxide and then transforms into $H_2O$ (Figure 1. 2).[6] With Pt as the catalytic surface, ORR usually adopts the four-electron pathway, which can occur through either a dissociative or an associative route, depending on whether the $O_2$ molecule dissociates before the reduction. The dissociation pathway is preferred when the surface binds $O_2$ strongly or when the oxygen surface coverage is low, while the association pathway is favored when the surface $O_2$ adsorption is weak or when the surface oxygen coverage is high.[6, 11] According to the associative mechanism (Figure 1.2) and the scaling relation[12], the binding energy of OH* and OOH* are all linear to that of the O*, which leads to the final "volcano plot" (Figure 1.3) with the x-axis as the O* binding energy and y-axis as the activity[13-14]. Furthermore, it has been proposed that the OOH* formation or the $O_2$* dissociation is the RDS for the right-slope catalysts, while the OH* desorption and further water formation is the RDS for the left-slope catalysts. For example, pure Pt binds O* too strongly, leading to sluggish OH* desorption.

Currently, the most explored enhancement strategy is tuning the electronic structure of catalysts to reach the optimum activity in the volcano plot. For example, alloying Pt with other transition metals to induce strain effect[15-16] or ligand effect[17-18] is commonly used to modulate the O-binding energy and lower the overpotential of the reaction and enhance the ORR kinetics.[19-20]

Alternatively, tailoring the average coordination number can also optimize the O binding energy, achieving better activity for specific concave sites.[21-22] Despite considerable progress, it would be interesting to further upshift the activity limit by designing the catalyst-electrolyte interface to improve the microkinetic.

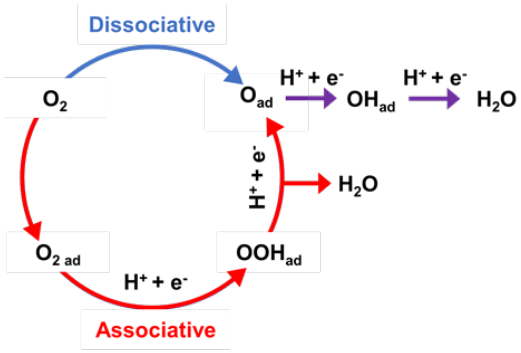


**Figure 1. 2.** Schematic illustration for the direct four-electron ORR path-ways. The red and blue arrows represent the associative and the dissociative pathway, respectively. The purple arrows represent the reactions that include in both pathways. Adapted with permission from Ref.[23] Copyright 2020 American Chemical Society.

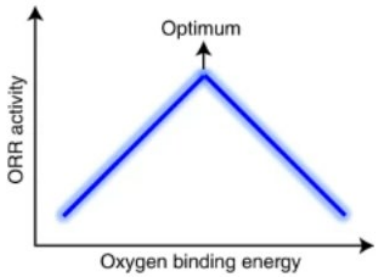


**Figure 1.3.** Illustration of ORR volcano plot, showing that the O* binding energy should be neither too strong nor too weak. Adapted with permission from Ref.[24]

### 1.3 Motivation to translate RDE activity to MEA performance

Half-cell techniques based on thin film rotating disk electrode (RDE) have been the most widely used evaluation method for rapid catalysts screening and are regarded as an indicator of its performance in the MEA. Also, the well-controlled RDE tests are perceived to give the intrinsic

activities of catalysts by compensation of mass transport and excluding the influence of other engineering factors. However, an increasing number of studies have reported that not all promising RDE ORR activity results have translated to the actual performance in MEA[25] (Figure 1. 3). Many catalysts with excellent activity and stability in RDE measurements failed to demonstrate similar promising performance in MEA tests, while some catalysts with less-encouraging RDE results showed impressive MEA performance.[26-27] The reason that RDE results tend to be an unreliable predictor of MEA performance is mainly due to the distinctive operating condition: 1) the high operating current densities level in MEA compared to RDE with low mass loading on the thin film and poor mass transfer in electrolytes, 2) different electrode structure, 3) testing conditions and protocols, 4) the higher stability requirement of catalysts in MEA environment and other factors. The risk of RDE-to-MEA discrepancy warrants the importance of including MEA development in the early stages of catalyst material exploration.

Moreover, the fuel cell and thus the Pt-based catalysts undergo continuous potential fluctuations between high and low potential during operation, which promotes Pt dissolution. As a result, the facet structure and surface compositions of the shaped-controlled catalysts turned out to be hard to stabilize during MEA testing, and the carefully designed morphology would not last. Thus, the catalyst stability issue becomes a major challenge, which inspires the researcher to re-examine the catalyst design principle and shift our focus from designing delicate shape-controlled nanocatalysts to more stable catalysts with practical potential.

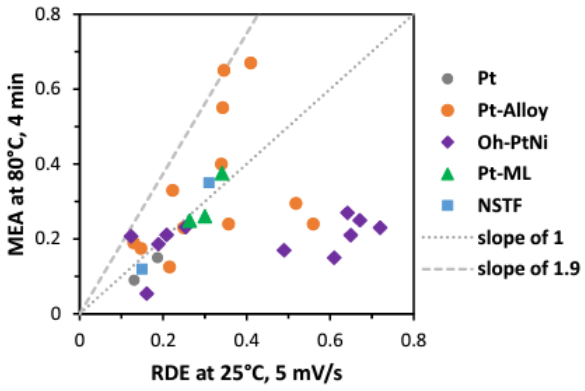


**Figure 1. 3** Comparison of ORR Pt-mass activity measurements (in $A/mg_{Pt}$) at $0.9V_{RHE}$ by RDE and MEA. MEA results are compared with RDE measured by GM and with published RDE results. Adapted with permission from Ref.[28]

## 1.4 References


1. Greeley, J.; Stephens, I. E. L.; Bondarenko, A. S.; Johansson, T. P.; Hansen, H. A.; Jaramillo, T. F.; Rossmeisl, J.; Chorkendorff, I.; Nørskov, J. K., Alloys of platinum and early transition metals as oxygen reduction electrocatalysts. *Nature Chemistry* **2009,** *1* (7), 552-556.

2. Zhao, Z.; Chen, C.; Liu, Z.; Huang, J.; Wu, M.; Liu, H.; Li, Y.; Huang, Y., Pt-based nanocrystal for electrocatalytic oxygen reduction. *Advanced Materials* **2019,** *31* (31), 1808115.

3. Kodama, K.; Nagai, T.; Kuwaki, A.; Jinnouchi, R.; Morimoto, Y., Challenges in applying highly active Pt-based nanostructured catalysts for oxygen reduction reactions to fuel cell vehicles. *Nature Nanotechnology* **2021,** *16* (2), 140-147.

4. Fan, J.; Chen, M.; Zhao, Z.; Zhang, Z.; Ye, S.; Xu, S.; Wang, H.; Li, H., Bridging the gap between highly active oxygen reduction reaction catalysts and effective catalyst layers for proton exchange membrane fuel cells. *Nat. Energy* **2021,** *6* (5), 475-486.

5. Kongkanand, A.; Mathias, M. F., The priority and challenge of high-power performance of low-platinum proton-exchange membrane fuel cells. *J. Phys. Chem. Lett.* **2016,** *7* (7), 1127-1137.

6. Nørskov, J. K.; Rossmeisl, J.; Logadottir, A.; Lindqvist, L.; Kitchin, J. R.; Bligaard, T.; Jónsson, H., Origin of the Overpotential for Oxygen Reduction at a Fuel-Cell Cathode. *The Journal of Physical Chemistry B* **2004,** *108* (46), 17886-17892.

7. Nie, Y.; Li, L.; Wei, Z., Recent advancements in Pt and Pt-free catalysts for oxygen reduction reaction. *Chemical Society Reviews* **2015,** *44* (8), 2168-2201.

8. Seh, Z. W.; Kibsgaard, J.; Dickens, C. F.; Chorkendorff, I.; Nørskov, J. K.; Jaramillo, T. F., Combining theory and experiment in electrocatalysis: Insights into materials design. *Science* **2017,** *355* (6321), eaad4998.

9. Tripković, V.; Skúlason, E.; Siahrostami, S.; Nørskov, J. K.; Rossmeisl, J., The oxygen reduction reaction mechanism on Pt(111) from density functional theory calculations. *Electrochimica Acta* **2010,** *55* (27), 7975-7981.

10. O'Hayre, R.; Cha, S. W.; Colella, W.; Prinz, F. B., *Fuel Cell Fundamentals*. Wiley: 2016.

11. Kulkarni, A.; Siahrostami, S.; Patel, A.; Nørskov, J. K., Understanding Catalytic Activity Trends in the Oxygen Reduction Reaction. *Chemical Reviews* **2018,** *118* (5), 2302-2312.

12. Stephens, I. E. L.; Bondarenko, A. S.; Grønbjerg, U.; Rossmeisl, J.; Chorkendorff, I., Understanding the electrocatalysis of oxygen reduction on platinum and its alloys. *Energy Environ. Sci.* **2012,** *5* (5), 6744-6762.

13. Nørskov, J. K.; Rossmeisl, J.; Logadottir, A.; Lindqvist, L.; Kitchin, J. R.; Bligaard, T.; Jónsson, H., Origin of the overpotential for oxygen reduction at a fuel-cell cathode. *J. Phys. Chem. B* **2004,** *108* (46), 17886-17892.

14. Greeley, J.; Stephens, I. E. L.; Bondarenko, A. S.; Johansson, T. P.; Hansen, H. A.; Jaramillo, T. F.; Rossmeisl, J.; Chorkendorff, I.; Norskov, J. K., Alloys of platinum and early transition metals as oxygen reduction electrocatalysts. *Nat. Chem.* **2009,** *1* (7), 552-556.

15. Strasser, P.; Koh, S.; Anniyev, T.; Greeley, J.; More, K.; Yu, C.; Liu, Z.; Kaya, S.; Nordlund, D.; Ogasawara, H.; Toney, M. F.; Nilsson, A., Lattice-strain control of the activity in dealloyed core–shell fuel cell catalysts. *Nat. Chem.* **2010,** *2* (6), 454-460.

16. Escudero-Escribano, M.; Malacrida, P.; Hansen, M. H.; Vej-Hansen, U. G.; Velázquez-Palenzuela, A.; Tripkovic, V.; Schiøtz, J.; Rossmeisl, J.; Stephens, I. E. L.; Chorkendorff, I., Tuning the activity of Pt alloy electrocatalysts by means of the lanthanide contraction. *Science* **2016,** *352* (6281), 73-76.

17. Stamenkovic, V. R.; Fowler, B.; Mun, B. S.; Wang, G.; Ross, P. N.; Lucas, C. A.; Marković, N. M., Improved oxygen reduction activity on $Pt_3Ni(111)$ via increased surface site availability. *Science* **2007,** *315* (5811), 493.

18. Stamenkovic, V.; Mun, B. S.; Mayrhofer, K. J. J.; Ross, P. N.; Markovic, N. M.; Rossmeisl, J.; Greeley, J.; Nørskov, J. K., Changing the activity of electrocatalysts for oxygen reduction by tuning the surface electronic structure. *Angew. Chem. Int. Ed.* **2006,** *45* (18), 2897-2901.

19. Kitchin, J. R.; Nørskov, J. K.; Barteau, M. A.; Chen, J. G., Role of strain and ligand effects in the modification of the electronic and chemical properties of bimetallic surfaces. *Phys. Rev. Lett.* **2004,** *93* (15), 156801.

20. Stamenkovic, V. R.; Fowler, B.; Mun, B. S.; Wang, G.; Ross, P. N.; Lucas, C. A.; Marković, N. M., Improved oxygen reduction activity on $Pt_3Ni(111)$ via increased surface site availability. *Science* **2007,** *315* (5811), 493-497.

21. Calle-Vallejo, F.; Pohl, M. D.; Reinisch, D.; Loffreda, D.; Sautet, P.; Bandarenka, A. S., Why conclusions from platinum model surfaces do not necessarily lead to enhanced nanoparticle catalysts for the oxygen reduction reaction. *Chem. Sci.* **2017,** *8* (3), 2283-2289.

22. Calle-Vallejo, F.; Tymoczko, J.; Colic, V.; Vu, Q. H.; Pohl, M. D.; Morgenstern, K.; Loffreda, D.; Sautet, P.; Schuhmann, W.; Bandarenka, A. S., Finding optimal surface sites on heterogeneous catalysts by counting nearest neighbors. *Science* **2015,** *350* (6257), 185-189.

23. Liu, Z.; Zhao, Z.; Peng, B.; Duan, X.; Huang, Y., Beyond Extended Surfaces: Understanding the Oxygen Reduction Reaction on Nanocatalysts. *Journal of the American Chemical Society* **2020,** *142* (42), 17812-17827.

24. Luo, M.; Koper, M. T. M., A kinetic descriptor for the electrolyte effect on the oxygen reduction kinetics on Pt(111). *Nature Catalysis* **2022,** *5* (7), 615-623.

25. Kongkanand, A.; Mathias, M. F., The Priority and Challenge of High-Power Performance of Low-Platinum Proton-Exchange Membrane Fuel Cells. *J Phys Chem Lett* **2016,** *7* (7), 1127-1137.

26. Debe, M. K., Electrocatalyst approaches and challenges for automotive fuel cells. *Nature* **2012,** *486* (7401), 43-51.

27. Huang, Y.; Zhang, J. L.; Kongkanand, A.; Wagner, F. T.; Li, J. C. M.; Jorne, J., Transient Platinum Oxide Formation and Oxygen Reduction on Carbon-Supported Platinum and Platinum-Cobalt Alloy Electrocatalysts. *J Electrochem Soc* **2014,** *161* (1), F10-F15.

28. Yarlagadda, V.; McKinney, S. E.; Keary, C. L.; Thompson, L.; Zulevi, B.; Kongkanand, A., Preparation of PEMFC Electrodes from Milligram-Amounts of Catalyst Powder. *Journal of The Electrochemical Society* **2017,** *164* (7), F845.

# Chapter 2. Surface molecular modification enables ultrahigh activity catalyst for ORR

## 2.1 Introduction

Improvements in the performance of costly catalysts (e.g., Pt) is critical for the storage and conversion of renewable clean energy[1]. Intensive efforts have been devoted to searching for catalysts with higher catalytic activity[2-5] and longer-term stability[6-7]. A generally adopted strategy is through strain effect[2, 8] or ligand effect[3, 9] to achieve an optimal binding energy between catalyst surface and reaction species, which can lower the overpotential of the reaction and enhance the activity. Despite considerable progress made so far, further enhancement is required. In the meanwhile, such guidance has been largely motivated by theoretical considerations in vacuum, while microkinetic at the catalyst-electrolyte interface was not taken into consideration. A long-standing yet overlooked issue for many electrochemical reactions is the insufficient reactant supply at the catalyst surface. For example, the low oxygen solubility ($2.56\times10^{-4}$ M) in 0.1 M $HClO_4$ and small equilibrium constants for initial physisorption largely impede the already sluggish ORR kinetics.[10-11] Using hydrophobic ionic liquids (ILs) with a higher bulk $O_2$ solubility (ca. 2.4 times compared to that of 0.1 M $HClO_4$) has been shown to mitigate this problem and improve the ORR activity.[12-14] However, the high cost of ILs brings additional economic penalties for fuel cells. In parallel, the timely removal of water is of equally importance to accelerate reaction, following the Le Chatelier's principle. Therefore, in ORR, it is highly desirable to facilitate the influx of oxygen and outflux of water to further propel the activity. Recently, the addition of cations[15], pyridine[16], melamine[17], and tetrahexylammonium cations[18] in the electrolyte has been shown to effectively improve the ORR kinetics of pure Pt, through either alleviating surface poisoning or modification of surface electronic states by competitive binding to Pt surface.

Herein, we demonstrated that a ligand can act as an oxygen trap and surface molecular pump to significantly accelerate reactant supply and product removal in ORR (Figure 2. 1)**[19].** The local Pt-$O_2$ concentration, $c_{Pt-O_2}$, could be approximately doubled and the surface molecular pump allows for reduced surface water concentration and retention time, leading to faster outflux of water. Together, the surface molecular pump can further enhance the specific activity (SA) of electrocatalytic reactions (e.g., ORR). Our experimental studies revealed that adsorbed dimethylformamide (DMF) molecules, as a surface molecular pump, can effectively improve the SA of Pt/C by two-fold in 0.1 M $HClO_4$ electrolyte. Molecular dynamics (MD) simulations suggest that physisorption of DMF on the Pt surface can accelerate $O_2$ transport from the electrolyte towards the Pt surface, lower the oxygen Gibbs physisorption energy and prolong the oxygen contact time. DMF thus greatly affects the physisorption behavior of $O_2$ towards Pt, which was recently compared to the overall chemical reaction process[11]. Interestingly, reactions require milliseconds at the nanometer scale to occur and therefore strongly depend on preceding physisorption equilibria (Figure 2. 1). Due to a much shorter time scale of nanoseconds and low binding free energies of $O_2$ below -0.6 kcal/mol (-0.025 eV), physisorption has an immense effect on the interfacial microenvironment, which directly correlates with the ORR kinetic current[11, 20]. The MD simulations show that DMF physisorption on Pt surface leads to increased interfacial $O_2$ concentration and reduced water concentration on the Pt surface, which collectively boosts the ORR activity by way of Le Chatelier's Principle (Figure 2. 1). We further applied this approach to a model Pt-alloy catalyst (PtCuNi), achieving an unprecedented ORR SA of 21.8 ± 2.1 mA/cm$^2$ at 0.9 V versus the reversible hydrogen electrode (RHE), which nearly doubles the previously reported record in the literature, leading to an ultrahigh mass activity (MA) of 10.7 ± 1.1 A/mg$_{Pt}$.

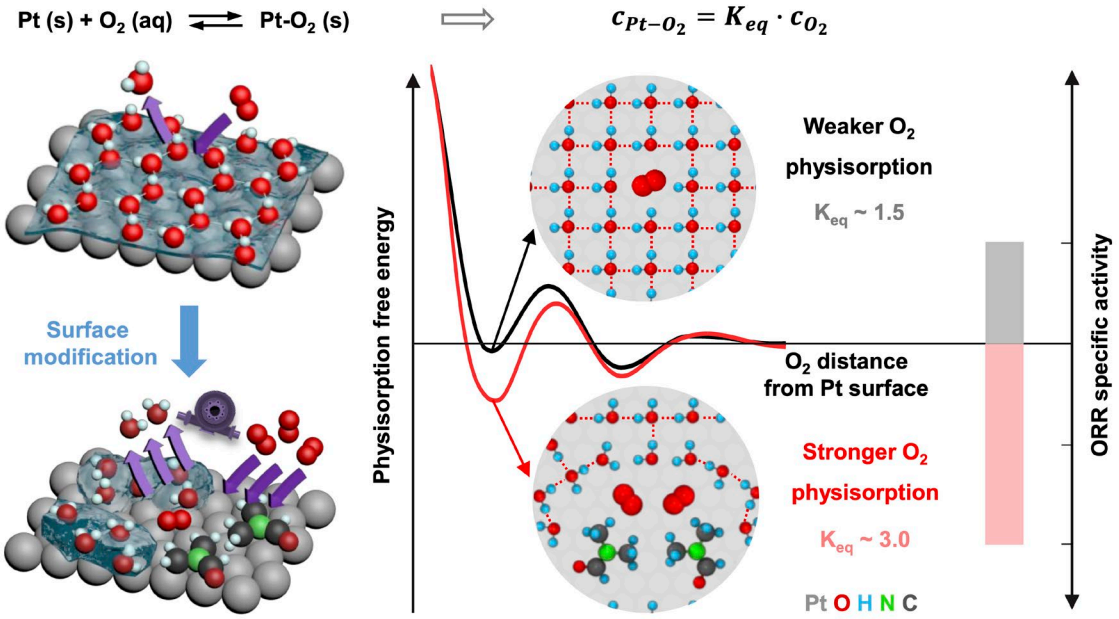


**Figure 2. 1** Schematic illustration of the boosted ORR kinetics by surface modification of Pt. The application of DMF as oxygen trap and surface molecular pump can facilitate higher interfacial oxygen concentration ($c_{Pt-O_2}$) and lower interfacial water concentration (left) by breaking the network of hydrogen bonds in water adlayers on the Pt surface (left). The surface molecular pump lowers the physisorption free energy of $O_2$ on the surface and shifts the physisorption equilibrium constant towards higher ORR specific activity (length of light red bar). The SA is shown in arbitrary units for simplicity and a color legend for the atoms is included on the lower right.

## 2.2 Methods

### Materials and Chemicals

Platinum(II) acetylacetonate ($Pt(acac)_2$, 97%), nickel(II) acetylacetonate ($Ni(acac)_2$, 95%), copper (II) acetate ($Cu(AC)_2$, 97%), perchloric acid ($HClO_4$, 70%, PPT Grade), glucose, oleylamine [OAm; $CH_3(CH_2)_7CH{=}CH(CH_2)_7CH_2NH_2$, >70%], 1-octadecene [ODE; $CH_2{=}CH(CH_2)_{15}CH_3$; technical grade, >90%], 5 wt % Nafion were all purchased from Sigma-Aldrich. Commercial Pt/C catalyst (40 wt% Pt) were purchased from Alfa Aesar. N, N-dimethylformamide (DMF, ≥99.8%), ethanol (200 proof), cyclohexane ($C_6H_{12}$; analytical reagent, >99.5%) were obtained from EMD Millipore and Decon. Isopropanol (≥99.5%) were purchased from Fisher Scientific. All reagents were used as received without further purification.

Carbon black (Vulcan XC-72) was received from Carbot Corporation and annealed in 280 ℃ air before used. The deionized water (18 MΩ/cm) was obtained from an ultra-pure purification system (Milli-Q advantage A10). Ultrahigh purity CO was purchased from Airgas, Inc.

**Preparation of PtCuNi catalysts**

The synthesis of PtCuNi catalysts is similar to a previous report[21]. In a typical preparation, $Pt(acac)_2$ (20 mg), $Cu(AC)_2$ (6 mg), $Ni(acac)_2$ (6 mg), glucose (135 mg), OAm (3 ml), and ODE (2 ml) were added into a vial (volume, 35 ml). The mixture was ultrasonicated for 1 hour and then purged with ultrahigh purity carbon monoxide (CO) for 5 minutes and heated from room temperature to 170 °C in 30 minutes and kept at 170 ℃ for 12 hours in an oil bath with stirring of 300 r.p.m. The colloidal products were collected by centrifugation and washed with cyclohexane/ethanol (v/v = 1:5) mixture for two times. The PtCuNi catalysts were loaded onto 20 mg of carbon black (Vulcan XC-72) by sonication for 2 hours. The as-prepared PtCuNi catalysts were suspended in 20 mL cyclohexane/ethanol (v/v = 1:1) mixture. To load the sample onto carbon black, 20 mg of carbon black was added and sonicated for 2 hours. The resulting catalysts were collected by centrifugation, washed with cyclohexane/ethanol mixture, and annealed at 130 °C for 6 hours in a home-build tube furnace with 100 sccm Ar flow.

**Application of surface-modified on PtCuNi catalyst and Pt/C catalyst**

The resulting dried PtCuNi catalysts or as-received Pt/C catalysts were first dispersed DMF with a concentration of 1 mg/mL and ultrasonicated for 20 minutes. The resulting solution was heated with magnetic stirring in an oil bath at 120 ℃ for desired time. After the modification, the resulting catalysts were washed with IPA three times and further dried in a vacuum dryer.

**Structure and composition characterization**

High-resolution TEM images (HRTEM), energy-dispersive X-ray spectroscopy (EDX) line-scan file and the high-angle annular dark-field scanning transmission electron microscope (HAADF-STEM) images were taken on JEM-ARM300F Grand ARM Transmission Electron Microscope operated at 300 kV. TEM samples were prepared by dropping ethanol dispersion of catalysts onto carbon-coated aluminum TEM grids (Ted Pella, Redding, CA). The Pt loading of catalysts was determined by the inductively coupled plasma atomic emission spectroscopy (ICP-AES). The Pt loading is determined before electrochemical measurement. X-ray photoelectron spectroscopy (XPS) tests were carried out on a Kratos AXIS Ultra DLD spectrometer. All samples were electrochemically activated prior to XPS tests.

**Electrochemical measurements**

A three-electrode cell system was used to conduct all electrochemical tests. The working electrode was a glassy carbon rotating disk electrode (RDE) with a 0.196 $cm^2$ glassy carbon geometry area from Pine Instruments. The counter and reference electrodes are Pt wire and Ag/AgCl (1 M $Cl^-$). For activity measurement, Pt loadings were 10.2 $\mu g/cm^2$ and 7.85 $\mu g/cm^2$ for Pt/C catalysts and all PtCuNi catalysts. Cyclic voltammetry (CV) activations were performed in $N_2$-saturated 0.1 M $HClO_4$ electrolyte with potential scan rate of 100 $mVs^{-1}$. Electrochemical active surface area (ECSA) determined by $H_{upd}$ was calculated by integrating hydrogen adsorption charge on CV curve by taking a value of 210 $\mu C/cm^2$ for the adsorption of a hydrogen monolayer. Oxygen reduction reaction (ORR) was tested in an $O_2$-saturated 0.1 M $HClO_4$ electrolyte with a potential scan rate of 20 mV/s. The measurement temperature was set at 25 °C using a water bath 5-neck flask. The current density of ORR polarization curve was iR-corrected during the measurements. The accelerated durability test (ADT) was done at room temperature in $O_2$-saturated 0.1 M $HClO_4$ solutions by applying CV sweep between 0.6 and 1.1 V versus RHE at a sweep rate of 100 $mVs^{-1}$

for 20,000 cycles. ORR tests were performed before the stability test, after 20,000 cycles of ADT.

**Computational methods**

All atomic/molecular models were prepared using the Materials Studio program[22] under 3D periodic boundary conditions, including the Pt(111) surfaces, $H_2O$ molecules (flexible simple point charge, SPC water model), DMF molecules, $O_2$ molecules, perchlorate anions, and hydronium cations.

The INTERFACE Force Field (IFF) was used for Pt atoms, $O_2$ molecules, perchloride anions, the flexible SPC water model, and hydronium cations using 12-6 LJ format (CHARMM), along with CHARMM36 parameters for DMF molecules. IFF uses a classical Hamiltonian and covers parameters for inorganic and organic compounds with systematic validation of chemical bonding (polarity), structures, energies, and physical-chemical interpretability[23]. IFF parameters for FCC metals are thermodynamically consistent Lennard-Jones (LJ) parameters that include excellent reproduction of lattice parameters (0.1% accuracy) and surface energies (3% accuracy) relative to experiments[11, 24]. The IFF parameters for molecular $O_2$ reproduce the liquid density, vaporization energy (at boiling point and 1 atm), and solvation free energy (298.15 K) within 3% deviation from experimental measurements down to an accuracy of 0.03 kcal/mol[25], about one to two orders of magnitude more accurate than other force fields. The accurate prediction of metal-organic and metal-aqueous interactions with IFF has been demonstrated including very high accuracy of computed binding energies within 5% of experimental measurements without additional fit parameters, comparable to uncertainties in experiments[26-28].

A Pt(111) slab with six Pt layers (600 Pt atoms) and a box size of 27.744 × 24.027 × 45.000 $Å^3$ was constructed. The zone above the Pt layers was filled with up to 175 DMF molecules, corresponding to a thickness of the liquid slab of approximately 30 Å. To correlate with the

conditions of surface modification of Pt catalyst in DMF, the simulation temperature was set to 393.15 K (equivalent to 120 °C, treatment temperature) and water was excluded here. The simulation was carried out in the isothermal-isobaric ensemble (NPT) under 1 atm for 8 ns to reach equilibrium as previously demonstrated for similar systems[29-30]. The equilibrium conformations were utilized to determine the number of DMF molecules per unit area corresponding to monolayer coverage.

The same Pt(111) model surface of a 6-layer Pt(111) slab with dimensions of 27.744×24.027×45.000 $Å^3$ was used to determine the number of DMF molecules equivalent to monolayer coverage. Various numbers of DMF molecules near monolayer coverage were placed flat on the Pt surface and the zone above was kept as a vacuum. MD simulations were carried out in the canonical (NVT) ensemble for 8 ns at 298.15 K, the electrochemical measurement temperature. The structure with the highest number of DMF molecules lying flat on the Pt(111) surface was defined as one monolayer (ML) coverage and determined to be 20 DMF molecules for the chosen slab, equal to 33.3 Å surface area per DMF molecule. This average value was used to determine the number of DMF molecules needed to represent different surface coverage in follow-on simulations.

The physisorption of $O_2$ molecules on the modified Pt(111) surfaces was investigated using models of supersaturated $O_2$ solutions that facilitate extensive physisorption statistics using moderate computation time. The models featured a box size of 69.360×62.470×53.000 $Å^3$ with 3900 Pt atoms (6 atomic layers of Pt), 5557 $H_2O$ molecules (flexible SPC model), and 100 $O_2$ molecules (equivalent to 1.0 M concentration), 10 hydronium ions and perchloride anions (equivalent to pH = 1.0). This concentration of $O_2$ was still low enough to avoid correlations between different $O_2$ molecules. Five model systems with different surface coverage by DMF

molecules were built to represent conditions in experiments. The surface coverage was chosen as 0.0, 0.1, 0.3, 0.5, and 0.7 with a corresponding number of 0, 13, 39, 65, and 91 DMF molecules for the chosen box size, respectively.

We employed the Nanoscale Molecular Dynamics program (NAMD) for all adsorption simulations[31]. For the analysis of $O_2$ physisorption, simulations were first equilibrated for 1 ns in the NPT ensemble at a pressure of 1 atm and then continued for 50 ns in the NVT ensemble to sample $O_2$ contacts, using equilibrium lattice parameters from the NPT period. All simulations involved 3D periodic boundary conditions, a timestep of 1 fs, a summation of Lennard-Jones interactions with a spherical cutoff at 1.2 nm, and a summation of electrostatic interaction using the PME method with a tolerance of $10^{-4}$ (high accuracy). 3D snapshots were collected every 1 ps to trace the abundant $O_2$ physisorption-desorption dynamics on the Pt(111) surfaces with various amounts of DMF. The temperature was maintained at 298.15 K consistent with electrochemical measurement conditions.

Equilibrium trajectories of 50 ns duration were analyzed across the time window from 10 ns to 50 ns for all models, equal to 40,000 snapshots for each system, using self-developed Python code with the MD Analysis package[32-33]. $O_2$ molecules (or $H_2O$ molecules) at a distance of 3.5 Å or less from Pt atoms on the surface were categorized to be in an adsorbed state[20]. All molecules that ever approached the surface within 3.5 Å were counted to determine the physisorption time (hereby, trends would not change if minimum physisorption times up to 100 ps were required). The total physisorption time was the sum of the physisorption time for every validly adsorbed molecule. The average physisorption time was then obtained by dividing the total physisorption time by the number of validly adsorbed molecules.

The thickness of the interfacial $O_2$ and $H_2O$ concentration are crucial for electrochemical reactions, was defined with a cutoff of 5 Å above the top atomic layer of the Pt(111) surface. The interfacial concentration of $O_2$ and $H_2O$ was defined as the average number of $O_2$ and $H_2O$ molecules per unit volume within the interfacial layer with an uncertainty equal to the standard error of the mean. All simulations were repeated 3 times and averaged to gain high accuracy and assure reproducibility.

The number of hydrogen bonds per water molecule were counted within the nearest molecular layer of water atop the Pt(111) surface. The maximum number are 2 hydrogen bonds per $H_2O$ molecule, equal to 4 shared hydrogen bonds, as found in ice or bulk water, with a strength of about 4.7 kcal/mol per hydrogen bond (equal to approximately half the vaporization energy of water). The criterion of identification of a hydrogen bond (H)O–H···O($H_2$) in water was a distance of less than 3.5 Å between the two oxygen atoms and an O–H···O angle within 180° ± 30°[34]. The average number of H-bonds was calculated by dividing the total number of H-bonds by the total number of $H_2O$ molecules in the adlayer, including periodic images across box boundaries.

The profiles of the free energy of $O_2$ physisorption were obtained by steered molecular dynamics (SMD) simulation with the Large-scale Atomic/Molecular Massively Parallel Simulator (LAMMPS) program[35]. Pt(111) slabs with and without DMF, respectively, were constructed for comparison. The box size was 24.969 × 24.027 × 65.550 $Å^3$, including 6 atomic layers of Pt atoms at the bottom, with periodic boundary conditions. DMF molecules were placed flatly on the Pt(111) surface at 50% surface coverage, in the same manner as previously described. The model system contained 1000 flexible SPC $H_2O$ molecules and one $O_2$ molecule only. Hydronium ions were not included as they can interact with the $O_2$ molecule during the pulling process and cause poor sampling. The $O_2$ molecule was initially placed at least 12 Å away from the Pt(111) surface in the

*z*-direction. It was coupled via a harmonic spring to a virtual point closer to the surface, which was pulled with a constant velocity towards the Pt(111) surface. The free energy was sampled using a pulling velocity of 1 Å/ns at distances larger than 6 Å. When the $O_2$ molecule moved closer than ~6 Å to the surface atomic layer of Pt, the pulling velocity of the virtual point was decreased to 0.03 Å/ns. This velocity was slow enough to achieve equilibrium sampling of $O_2$ interactions within the metal-water interfacial region, especially while passing through the immediate water adlayers that have strong interactions with both the metal surface and their neighbor molecules. Using the pulling velocity of 0.03 Å/ns or less then mimics a reversible process and served to obtain an accurate free energy profile. To avoid movement of the platinum slab, the bottom atomic layer of the slab was constrained in the pulling direction (*z*-direction) while allowing mobility in the other directions. The SMD simulations captured the approach of $O_2$ molecules from solution to physisorption on the surface for the entire electrode-electrolyte interface including the Pt (111) surface, surface-adsorbed DMF molecules to the extent present, explicit $H_2O$ molecules, $O_2$ molecules, as well as dynamics over a period of 140 ns.

The model systems were first pre-equilibrated for 1 ns in the NPT ensemble, and then the SMD protocol was carried out in the NVT ensemble. The trajectory frames and corresponding free energies were collected every 1 ps to generate a high-quality free energy profile. The Visual Molecular Dynamics (VMD) program was used to determine the distance between the geometric center of the $O_2$ molecule and the Pt(111) surface atomic layer in each frame. The calculated free energies were then plotted versus the distances between $O_2$ and Pt (111) surface layer.

Representative small molecular clusters were cut out from the snapshots of the MD trajectories, typically consisting of 1 $O_2$ molecule, the surrounding $H_2O$ and DMF molecules, and 2 atomic layers of Pt atoms below. First, 200 steps of geometry optimization and energy

minimization were carried out for each cluster to obtain a reasonable starting structure. Then, single-point energy calculations were conducted using the Materials Studio Discover module [22]. For this purpose, two systems, namely the surface system and the away system, were created with the same number and types of atoms. Typically, for the surface system, the $O_2$ molecule was in contact with the Pt(111) surface, while the $O_2$ molecule in the away system was at least 20 Å detached from the Pt(111) surface. At least 4 independent clusters were analyzed in this manner to obtain an average $O_2$ stabilization energy for each DMF coordination system as well as the standard deviation. The $O_2$ stabilization energy was calculated using the following equation:

$$E_{st} = E_{sur} - E_{away} \quad (1)$$

where $E_{st}$ is the $O_2$ stabilization energy, $E_{sur}$ represents the total energy of the surface system, and $E_{away}$ is the total energy of the away system.

Three model systems were built to calculate the physisorption energy of DMF. The box size was 27.744×24.027×45.000 $Å^3$ for all three systems. The first model was the surface system, which included 6 Pt layers, 652 $H_2O$ molecules, and 1 physiosorbed DMF molecule were included. The second model was the water system, which included 6 Pt layers and 652 $H_2O$ molecules. The third model system was the vacuum system, which contained only 1 DMF molecule in the same, otherwise empty box. The simulation settings were the same as described above for standard molecular dynamics over 50 ns. The physisorption energy $E_{ads}$ was calculated using the following equation:

$$E_{ads} = E_{sur} - E_{wat} - E_{vac} \quad (2)$$

where $E_{sur}$ is the average energy of the surface system, $E_{wat}$ represents the average energy of the water system, and $E_{vac}$ denotes the average energy of the vacuum system.

## 2.3 Results and discussion

### Surface molecular modification on Pt/C catalyst.

We first used Pt/C catalysts (40 wt% Pt, HiSPEC 4000, Johnson Matthey) as a model system to explore the effect of surface molecular pumps. DMF was chosen as the surface ligand due to its stability in a wide potential window[36] and the strong physisorption of amides in close contact following a soft epitaxial pattern, which has been previously described[28]. The Pt/C catalyst was treated in a pure DMF solution at 120 °C for a varied period of time to allow gradual molecular adsorption on the surface[37]. Cyclic voltammetry (CV) revealed that the Pt/C catalysts exhibited an initial electrochemically active surface area (ECSA) (based on hydrogen underpotential deposition, $H_{upd}$) of 51.6 ± 1.5 $m^2/g_{Pt}$, which decreased to 21.8 ± 0.2 $m^2/g_{Pt}$ after 48 hours of modification evidenced by a decreased $H_{upd}$ area (Figure 2. 2a). The Pt/C catalysts did not show noticeable size changes upon surface modification (Figure 2. 3), suggesting that the reduction of ECSA upon treatment time can be attributed to the blocking of available Pt surface sites with increasing DMF surface coverage (defined as the reduced ECSA, Figure 2. 2b). Indeed, X-ray photoelectron spectroscopy (XPS) studies (Figure 2. 4) revealed that the presence of N-species increased with longer modification time, indicating an increased amount of adsorbed DMF, which is consistent with the decreased ECSA (Figure 2. 2b). No apparent shift was observed in the XPS peak position for both $4f_{7/2}$ and $4f_{5/2}$ peaks, suggesting that surface-adsorbed ligands do not induce notable electronic effects on Pt (Figure 2. 4b).

The ORR activities of Pt/C catalysts were further evaluated using the linear sweep voltammetry (LSV) method (Figure 2. 2c). The SA of Pt/C catalysts increased from 0.48 ± 0.06 $mA/cm^2$ to 0.89 ± 0.04 $mA/cm^2$ after 24 h modification (surface coverage of 37.1%) and then decreased to 0.55 ± 0.02 $mA/cm^2$ after 48 h modification (surface coverage of 58.0%) (Figure 2.

2d). Accordingly, the MA of Pt/C catalyst increased from 0.23 ± 0.03 A/$mg_{Pt}$ to 0.28 ± 0.03 A/$mg_{Pt}$ after 24 h modification (Figure 2. 2d). These intriguing enhancements of both SA and MA motivated us to conduct multi-scale computational studies to understand the role of DMF in modulating the ORR activity at the catalyst-electrolyte interfaces.

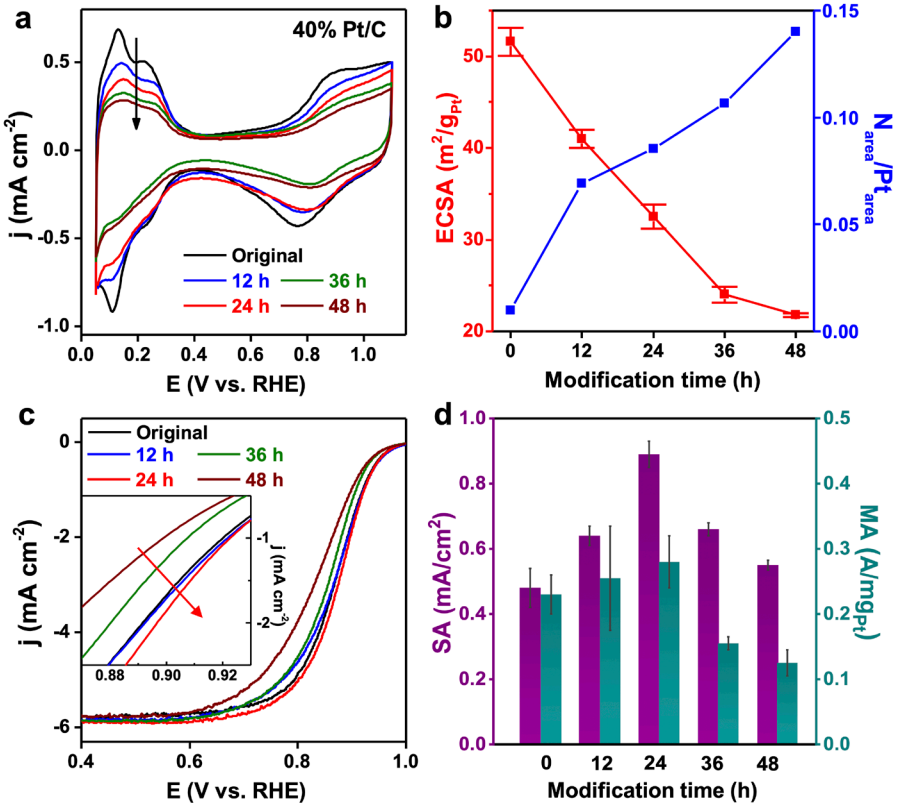


**Figure 2. 2** Electrochemical measurements in 0.1 M $HClO_4$ electrolyte of the 40% Pt/C catalysts modified with DMF at different treatment time. (a) CV curves of Pt/C catalysts at original stage (black), 12 h (blue), 24 h (red), 36 h (green), and 48 h (wine) modification time. (b) ECSA and N/Pt ratio obtained from XPS peak integration as a function of modification time. (c) ORR LSV curves of Pt/C catalysts at original stage (black), 12 h (blue), 24 h (red), 36 h (green), and 48 h (wine) modification time. The inset of the panel (c) is the enlarged potential window. (d) The evolution of SA (purple, left y-axis) and MA (olive, right y-axis) with modification time.

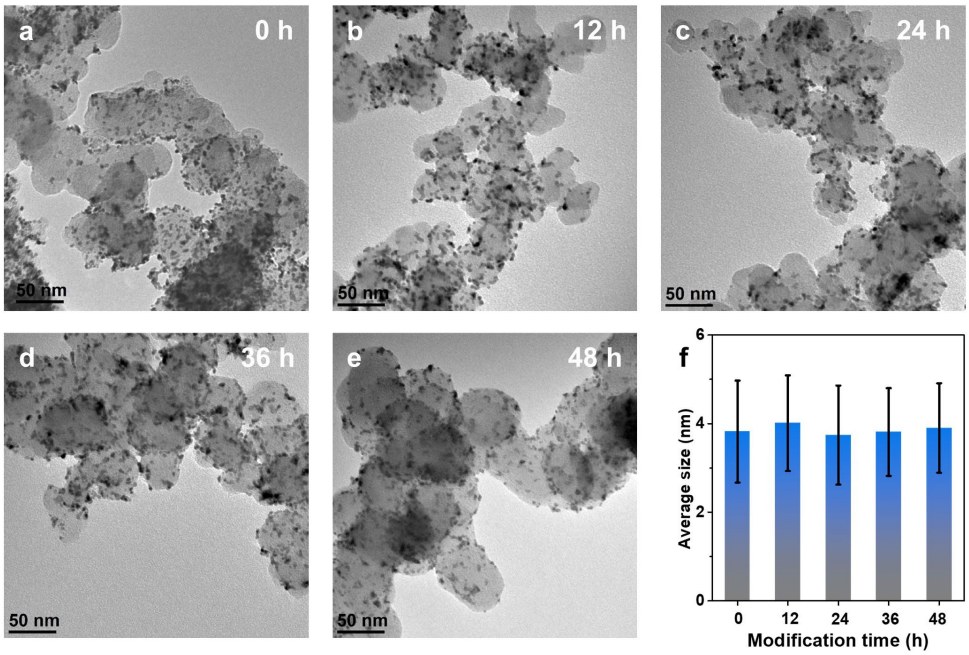


**Figure 2. 3** TEM characterizations of Pt/C catalysts. (a-e) TEM images of the Pt/C catalysts at different modification time. (f) the average size of the Pt/C catalysts at different modification time.

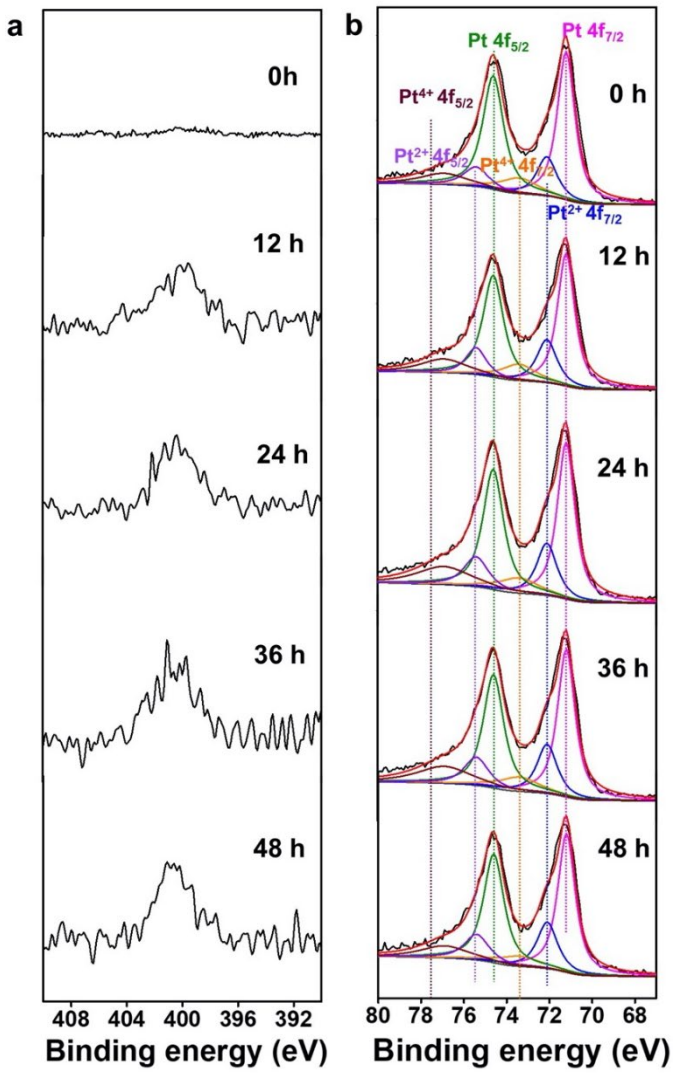


**Figure 2. 4** (a) XPS N 1s spectra of commercial Pt/C catalysts and (b) XPS Pt 4f spectra of Pt/C catalysts at different modification time.

**MD simulations of kinetics at the catalyst-electrolyte interfaces**

MD simulations were carried out with the INTERFACE force field (IFF)[23] (see Supplementary Information for simulation details) on a representative Pt(111) slab in a 0.1 M $HClO_4$ electrolyte to compare the dynamics and local concentration of $O_2$ and $H_2O$ at different DMF surface coverage from 0 to 70%. IFF MD simulations for catalyst-electrolyte interfaces were earlier shown to be of high reliability and efficient, suitable for analyzing realistically sized nanostructures and dynamics[11]. Without the addition of DMF (Figure 2. 5a), adsorbed $O_2$

molecules on the Pt(111) surface were surrounded by approximately 7 to 8 $H_2O$ molecules, forming a dense network of hydrogen bonds (blue circles). DMF molecules preferred to be flatly adsorbed on the Pt(111) surface with a physisorption energy of -26.5 ± 2 kcal/mol in an aqueous solution (Figure 2. 5b, c and Figure 2. 6b to e), which is strong enough to permanently replace $H_2O$ molecules and significantly modify the adlayer structure of $H_2O$. The circles with decreasing blue segments indicate that the number of surrounding $H_2O$ molecules near $O_2$ molecules adsorbed onto Pt considerably decreased for higher coverage with DMF molecules (Figure 2. 5a to c). When approaching the catalyst surface to gain direct access to the metal, $O_2$ molecules have to overcome free energy barriers to penetrate the hydrogen-bonded network of water molecules on the Pt surface and replace between one and two surface-bound $H_2O$ molecules (Figure 2. 5a, d, e)[11]. In the presence of the molecular pump DMF, $O_2$ molecules can more conveniently reach the Pt surface near the methyl groups of DMF molecules, enabling multiple van der Waals (vdW) interactions with $O_2$ molecules that increase their interaction with and retention on the Pt surface (Figure 2. 5b-e). The free energy barriers for physisorption are hereby small enough (<3 kcal/mol or <0.13 eV) to be crossed within hundreds of picoseconds and have no effect on the statistical physisorption equilibrium beyond nanoseconds (Figure 2. 5e).

Thus, we analyzed the equilibrium properties such as the interfacial concentration and physisorption time of $O_2$ and $H_2O$ (Figure 2. 1a). Within an interfacial layer of 0.5 nm[38], the interfacial $O_2$ concentration increased from 0.29 to 0.69 $nm^{-3}$, i.e., by a factor of 2.4, with a corresponding increase in DMF coverage from 0 to 50%; and then decreased to 0.64 $nm^{-3}$ when DMF coverage reached to 70% (Figure 2. 5f). The average physisorption time of $O_2$ on the Pt (111) surface was prolonged to 6.2 ns at 50% DMF coverage compared to 3.0 ns for the pure Pt(111) surface (Figure 2. 5g and Figure 2. 7), corresponding to an increase by a factor of 2.1. In addition

to local oxygen entrapment, by increasing the DMF coverage from 0% to 70%, the interfacial $H_2O$ concentration decreased from 30.1 $nm^{-3}$ to 12.6 $nm^{-3}$ within the interfacial layer (Figure 2. 8a) and the average physisorption time of $H_2O$ declined from 3.5 to 1.5 ns (Figure 2. 8b), which signified that the surface molecular pump also facilitated product removal (water), thereby speeding up the ORR. The average number of H-bonds per $H_2O$ molecule within the adlayer (see supplementary materials for simulation details) also showed a continuous decrease from 1.18 to 0.81 with increasing DMF coverage, indicating a notable reduction of the H-bond network due to the molecular pump effect of DMF (Figure 2. 5h and Figure 2. 9).

To confirm the more favorable $O_2$-DMF configuration compared to $O_2$-$H_2O$ configuration near the Pt surface, we further analyzed the stabilization energy of small clusters consisting of Pt, DMF, $H_2O$, and $O_2$, which represent the local environment of molecular pumps at the catalyst-electrolyte interface (Figure 2. 10a, b). The results manifested that an increasing number of DMF molecules in the cluster increased the oxygen stabilization energy (Figure 2. 10c). Hereby, coordination of $O_2$ with one DMF "pump" molecule replaces approximately two $H_2O$ molecules and increases the stabilization energy by -0.24 ± 0.02 kcal/mol (Figure 2. 10d). Therefore, DMF stabilizes $O_2$ physisorption on Pt, and at the same time destabilizes $H_2O$ physisorption, which leads to a higher interfacial $O_2$ concentration and lower $H_2O$ concentration, creating a surface molecular pump and improving the ORR kinetics[39].

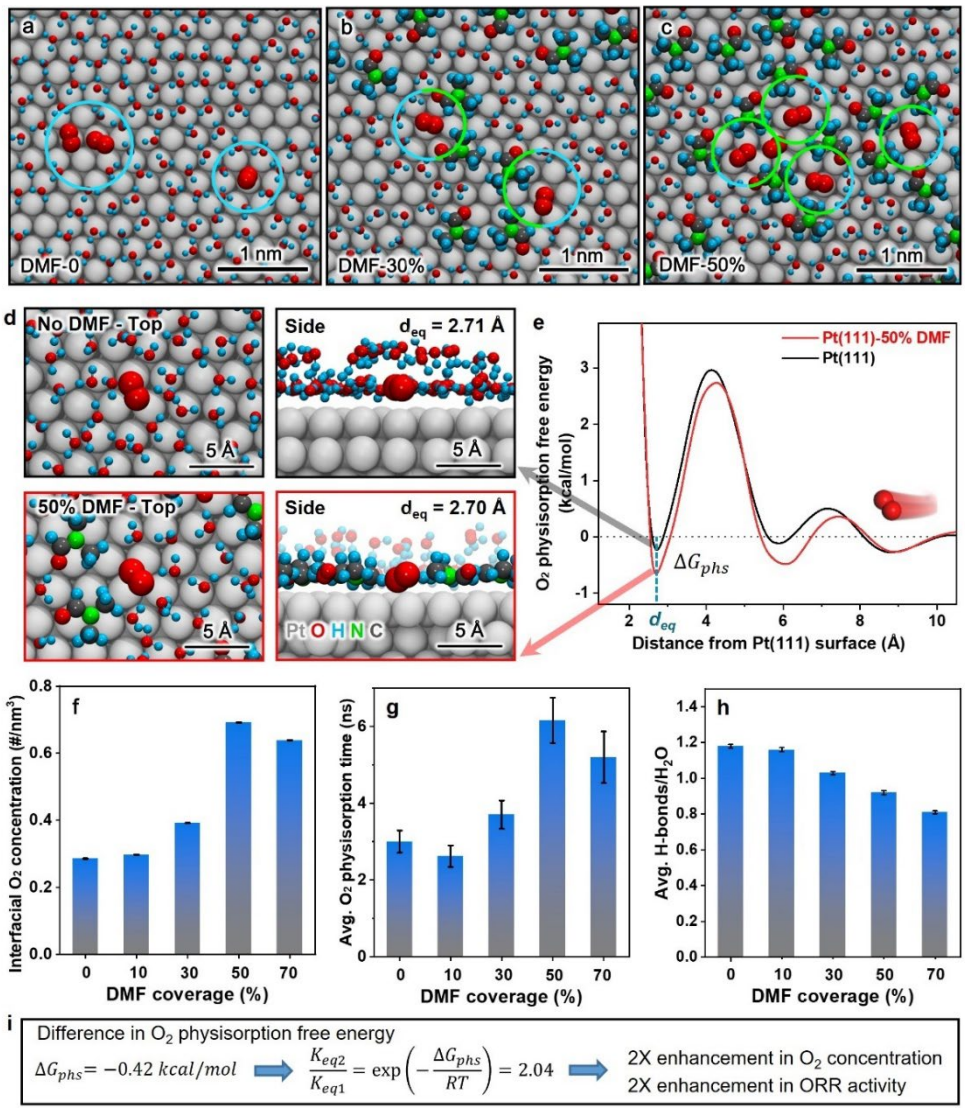


**Figure 2. 5** Molecular structure and dynamics of the catalyst-electrolyte interface, and the effect of the DMF from IFF MD simulations. (a-c) Snapshots of the molecular conformations of $O_2$, water, and DMF on the Pt(111) surface at DMF coverage of (a) 0%, (b) 30%, and (c) 50%. The circles represent the distribution of $H_2O$ (blue) and DMF methyl groups (green) surrounding adsorbed $O_2$ molecules. (d) Top and side views of the Pt(111) and Pt(111)-50% DMF surface, showing how DMF disrupts the water adlayer integrity and $O_2$ molecules are attracted by van-der-Waals interactions to both DMF and Pt. (e) Comparison of $O_2$ physisorption free energy on Pt(111) and Pt(111)-50% DMF surface from steered molecular dynamics simulations. The $O_2$ molecule is approaching the Pt(111) surface along the vertical direction during the simulations. $d_{eq}$ is the equilibrium distance for $O_2$ contact with the Pt(111) surface. (f) The relationship between DMF surface coverage and interfacial $O_2$ concentration (number of molecules/nm$^3$). The time-average number of $O_2$ molecules per unit volume of the interfacial layer within 0.5 nm distance from the Pt surface is shown[38]. (g) Average physisorption time of $O_2$ molecules. (h) Average number of H-bonds per $H_2O$ molecule in the first molecular layer on Pt. (i) The equations show the change in the physisorption free energy $\Delta G$ for 0% and 50% DMF coverage, the relationship between the

two equilibrium constants $K_{eq}$, and implications for the observed relative ORR activity. The gray, blue, red, green, and black spheres represent Pt, H, O, N and C, respectively. Electrolyte ions are hidden for clarity. Error bars represent the standard error of the mean. The analysis of hydrogen bonds assumes a maximum O−O distance of 3.5 Å and a maximum deviation of 30° from the linear (H)O−H ⋯ O($H_2$) angle[34].

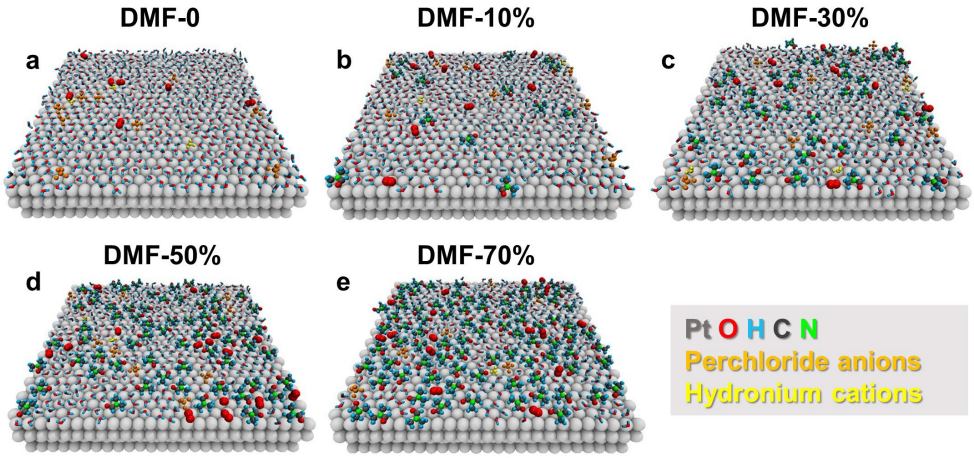


**Figure 2. 6** Snapshots of the Pt(111) surface with different coverage of DMF in equilibrium after simulation times of 50 ns. (a) 0% DMF. (b) 10% DMF. (c) 30% DMF. (d) 50% DMF. (e) 70% DMF. Molecules above the first adlayer are hidden for clarity.

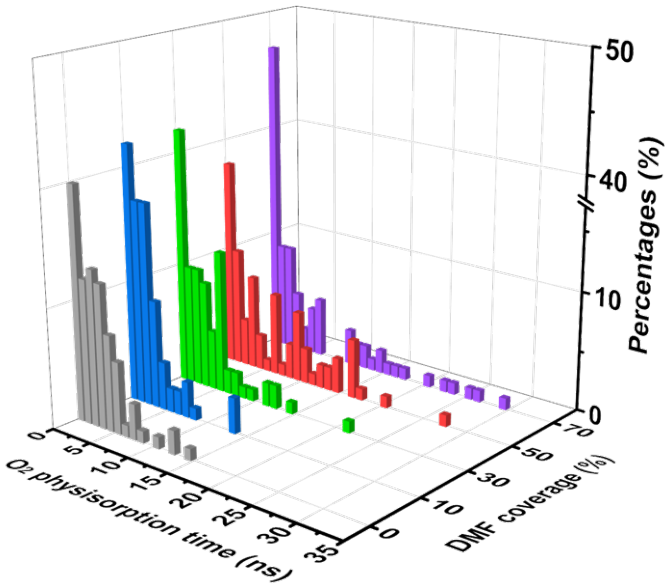


**Figure 2. 7** Statistical analysis of the physisorption time distribution for $O_2$ at different DMF surface coverage. The percentage axis represents the percentage of $O_2$ molecules for each time interval of physisorption. With an increase of DMF coverage, the physisorption time distribution broadens from 0-15 ns to 0-30 ns, i.e., DMF allows more $O_2$ molecules to adsorb for a longer time

on the Pt(111) surface. However, when the coverage reaches 70%, even though the physisorption time distribution is broadest, about half the $O_2$ molecules no longer had contact with the Pt surface. This percentage is higher than for any other surface coverage and, therefore, a DMF coverage of 50% exhibits the longest average $O_2$ physisorption time.

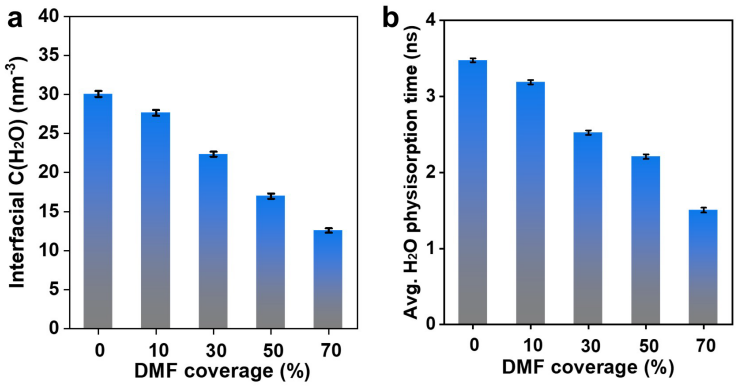


**Figure 2. 8** Interfacial concentration and physisorption time of $H_2O$ molecules on the Pt(111) surface for different coverage with DMF. (a) Interfacial $H_2O$ concentration and (b) average $H_2O$ physisorption time at different surface coverage with DMF. The error bars represent the standard error of the mean. Both the average interfacial $H_2O$ concentration and the $H_2O$ physisorption time are inversely proportional to the DMF coverage. The decrease in average physisorption time can be attributed to the interrupted water adlayer (less H-bonds) for higher DMF content, which facilitates faster $H_2O$ exchange at the catalyst-electrolyte interface.

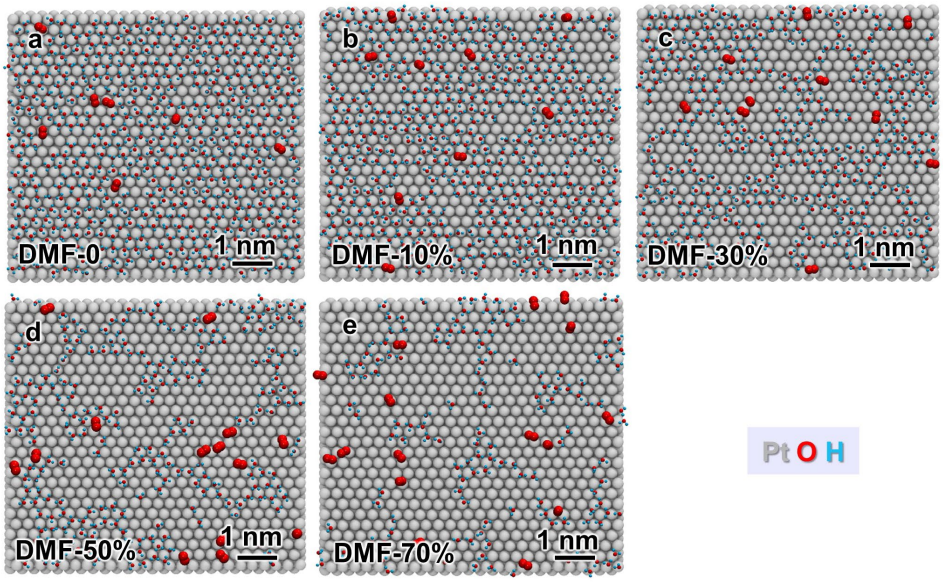


**Figure 2. 9** Snapshots of adlayer $H_2O$ and $O_2$ distributions on Pt(111) for different coverage with DMF in equilibrium after 50 ns simulation time. (a) 0% DMF, (b) 10% DMF, (c) 30% DMF, (d) 50% DMF, and (e) 70% DMF. DMF, hydronium cations, and $ClO_4^-$ anions are hidden to show the configuration of the broken water adlayers. For the calculation of the average number of H-bonds

(Figure 3H), a maximum O(H) ⋯ O distance of 3.5 Å and up to 30° deviation from linear geometry were applied as the criterion. The average number of H-bonds per water molecule were calculated by dividing the total number of formed H-bonds by the total number of $H_2O$ molecules in the adlayer.

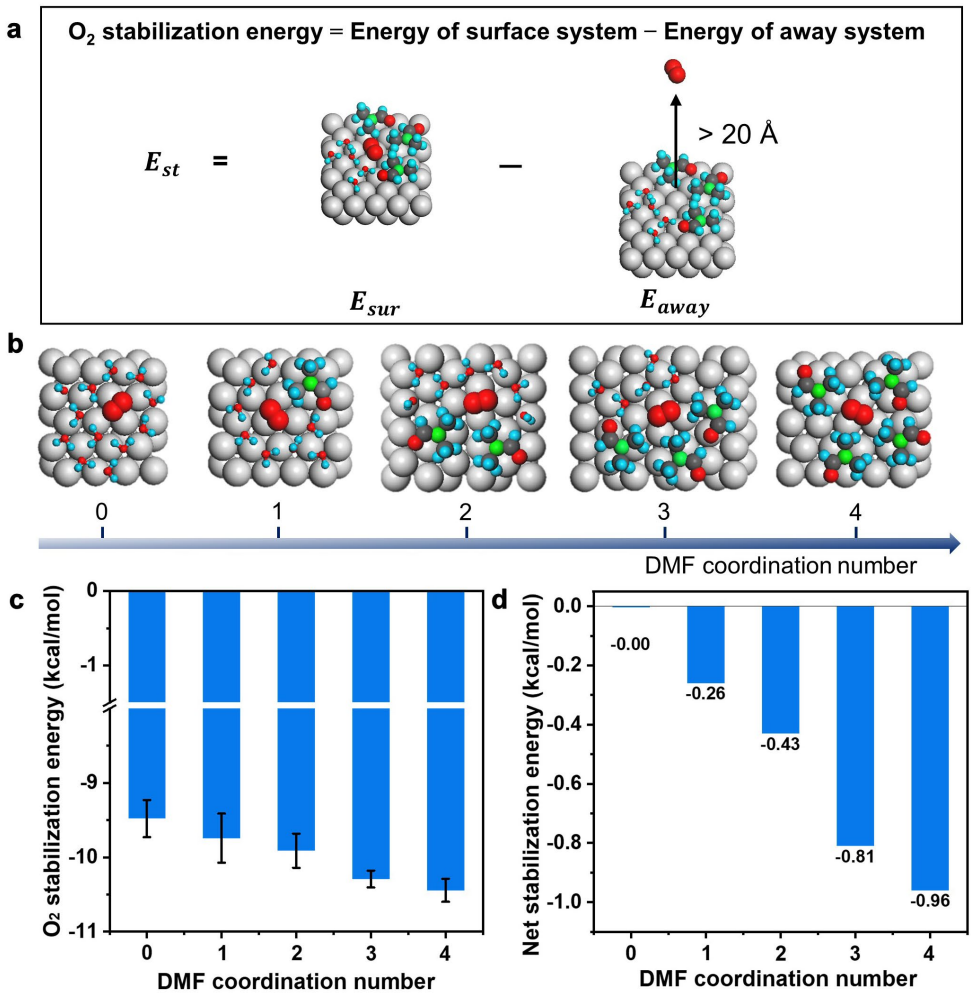


**Figure 2. 10** $O_2$ stabilization energy by DMF calculated using small Pt(111) surface clusters. (a) Schematic of the calculation protocol. We utilized equilibrium conformations of $O_2$ on a surface cluster versus the same conformations with the $O_2$ molecule moved >20 Å away into vacuum. (b) Typical structures of clusters with DMF coordination numbers from 0 to 4. (c) $O_2$ Stabilization energy ($E_{st}$) of clusters consisting of Pt, DMF, $H_2O$, and $O_2$ as a function of the number of close contacts of the $O_2$ molecule with neighboring DMF molecules (= DMF coordination number). A larger number of DMF molecules increases the stabilization energy of $O_2$. (d) The net stabilization energy of $O_2$ by DMF relative to pure water coordination (DMF coordination number = 0). The results indicate that coordination of $O_2$ with of 1 DMF molecule would increase the $O_2$ stabilization energy by ~0.24 kcal/mol on average. The typical net stabilization energy of about -0.48 kcal/mol by approximately 2 DMF molecules at 50% surface coverage is close to the increase in physisorption free energy of -0.42 kcal/mol of $O_2$ as independently determined by steered MD simulations of the entire electrode-electrolyte interface in Fig. 3e, i.

In specifics, the MD simulations of Pt(111) with 50% DMF (Figure 2. 5d, e) showed the highest interfacial $O_2$ concentration (0.69 $nm^{-3}$) within a 0.5 nm distance from the surface[38] and the longest $O_2$ physisorption time (6.2 ns), equal to a higher equilibrium concentration of $O_2$ on the Pt surface, thus leading to accelerated ORR kinetics. The expected increase in physisorption free energy of $O_2$ in the presence of DMF is quantitatively shown by the free energy profiles of $O_2$ molecules using steered molecular dynamics (SMD) for two control cases of 0% and 50% DMF coverage (Figure 2. 5d, e, I, Figure 2. 11 and Figure 2. 12), respectively. The global minimum at 2.7 Å distance from the Pt(111) surface atoms ($d_{eq}$) represents direct contact of $O_2$ with the Pt surface, and the associated physisorption free energy ($\Delta G$) of $O_2$ was, as expected, lower at -0.65 kcal/mol for Pt(111)-50% DMF compared to -0.23 kcal/mol for pure Pt(111) (Figure 2. 5e). The resulting free energy difference of -0.42 kcal/mol ($\Delta G_{phs}$ in Figure 2. 5e, i) matches the estimate of -0.48 kcal/mol from the small cluster calculation assuming an average of two DMF neighbors per $O_2$ molecule at 50% coverage (Figure 2. 5d, bottom, and Figure 2. 10). The peaks at 4 Å represent the energy barriers associated with $O_2$ penetration through the network of H-bonds in the closest adlayer of $H_2O$ molecules and the simultaneous replacement of $H_2O$ by $O_2$. The maximum energy barrier for transport of $O_2$ from bulk electrolyte (at infinity) to the surface is lower for the 50% DMF modified surface. The physisorption free energy ($\Delta G$) is directly related to the thermodynamic equilibrium constant ($K_{eq} = \exp\left(-\frac{\Delta G}{RT}\right) = \frac{c(Pt-O_2)_s}{c(O_2)_{aq}}$) (Figure 2. 1 and Figure 2. 5i). Accordingly, an increase in $K_{eq}$ by a factor of two using DMF can effectively increase the availability of adlayer $O_2$ for ORR, $c(Pt-O_2)_s$. Although the enhanced $O_2$ coverage is still low on an absolute scale, a small difference of 1 $RT$ (~0.59 kcal/mol at 298.15 K) can approximately change the coverage by 2.7 times. The difference in free energy minima of $\Delta G_{phs}$ of -0.42 kcal/mol

(Figure 2. 5e) increases the equilibrium constant $K_{eq}$ and the surface $O_2$ concentration $c(Pt-O_2)_s$ by a factor of ~2.0, semi-quantitatively matching the enhancement factor in ORR SA observed in the experiments (0.48 mA/cm$^2$ to 0.89 mA/cm$^2$) (Figure 2. 5f, g, i and Figure 2. 2d). This order of magnitude, while comparable to thermal motion, is statistically significant and critical over time like in other equilibrium and kinetic processes, such as conformation equilibria in chain molecules[40]. The interfacial $O_2$ concentration and average $O_2$ physisorption time decrease when DMF coverage reaches 70%, which is attributed to a substantially reduced number of available Pt surface sites for $O_2$ molecules. Although a fraction of $O_2$ molecules has much-prolonged physisorption times (> 20 ns) due to van-der-Waals interactions with DMF, 47% of $O_2$ molecules had barely any contact with the Pt(111) surface (Figure 2. 7). As a result, the average $O_2$ physisorption time at 70% DMF coverage (5.2 ns) is shorter than that at 50% DMF coverage (6.2 ns) (Figure 2. 5g). These observations agree with our experimental results and observations that excessive surface modification will lead to lower activity[41-42].

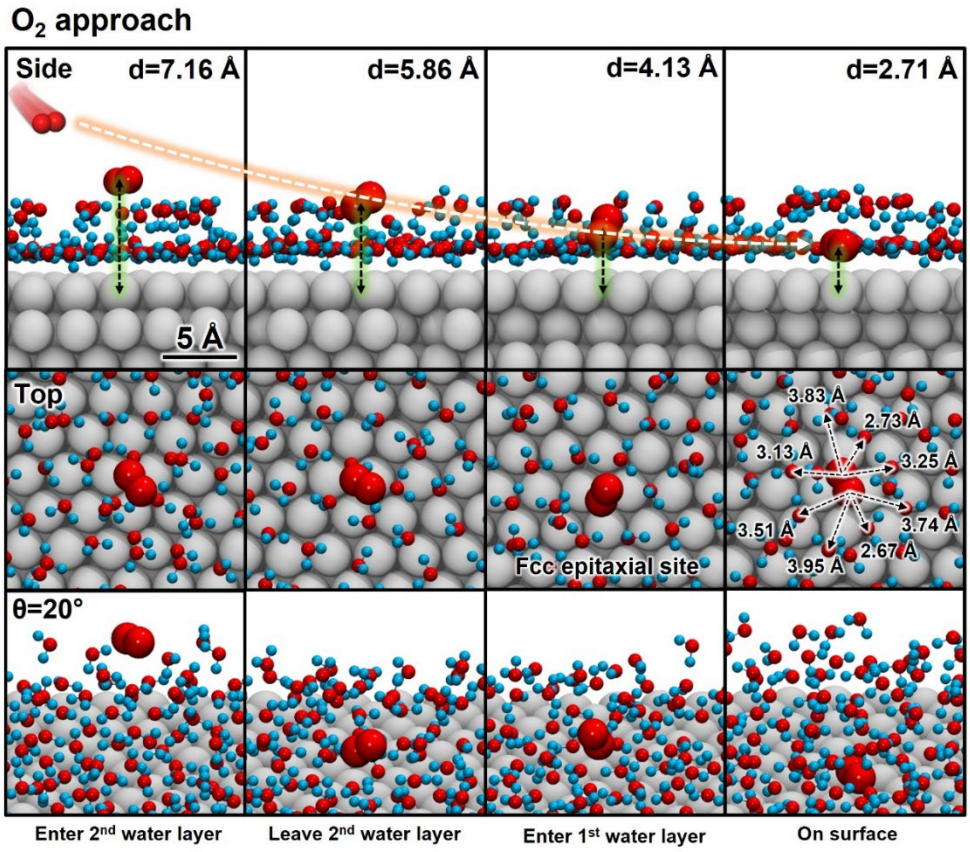


**Figure 2. 11** Side, top, and θ = 20° views of the surface configuration of Pt(111) without DMF in water at different stages of $O_2$ approach during steered molecular dynamics (SMD) simulation. The $O_2$ molecule was approaching the Pt(111) surface from the *z*-direction with a speed of 0.03 Å/ns. The distance *d* in the side views represents the vertical distance of the geometric center of the $O_2$ molecule from the plane of Pt(111) surface atoms. The evolutionary process visualizes the penetration of $O_2$ molecules through the water layers and eventual contact with the Pt(111) surface. When the $O_2$ molecule adsorbs on the Pt(111) surface, it tends to bind at the fcc epitaxial sites (top views). Moreover, the adsorbed $O_2$ molecule is surrounded by a dense hydrogen-bonded adlayer of approximately 8 $H_2O$ molecules with an average distance of 3.35 Å. The dense $H_2O$ network leads to a much higher free energy of $O_2$ penetration and physisorption, i.e., much less favorable, than in a vacuum. All panels use the same scale bar as shown in the top left.

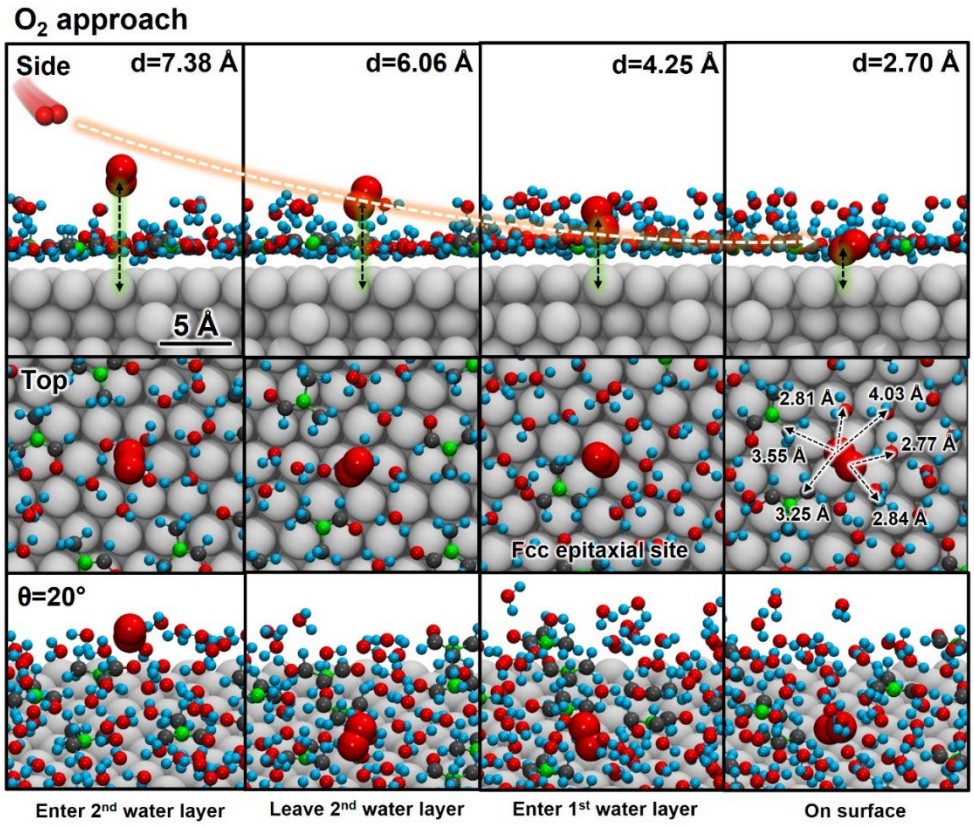


**Figure 2. 12** Side, top, and θ = 20° views of the surface configuration of Pt(111) with 50% DMF coverage in water at different stages of the $O_2$ approach during SMD simulation. The $O_2$ molecule was approaching the Pt(111) surface from the *z*-direction with a speed of 0.03 Å/ns. The distance *d* in the side views represents the vertical distance of the geometric center of the $O_2$ molecule to the plane of Pt(111) surface atoms. The evolutionary process shows how the $O_2$ molecule penetrates the water layers and finally adsorbs on the Pt(111) surface. Hereby, the DMF, as a surface ligand, disrupts the dense hydrogen-bonded $H_2O$ layers in the catalyst-electrolyte interface. The adsorbing $O_2$ molecule tends to bind at an epitaxial fcc site (top views), and close to the methyl groups of DMF. The number of surrounding $H_2O$ molecules is reduced from more than 8 to 4 with an average distance of 3.21 Å, and DMF disrupts the H-bonding network. These changes lower the free energy of $O_2$ penetration and $O_2$ physisorption. DMF acts as a surface "sink" for $O_2$ that modulates the adsorption kinetics of $O_2$ and $H_2O$ molecules. The enhancement of $O_2$ physisorption, Pt-$O_2$ contact time, and $H_2O$ removal boosts the ORR activity at the solid-electrolyte interface, following the Le Chatelier's Principle for the adsorption equilibrium. All panels use the same scale bar as shown in the top left.

**The universality of molecular pumps on catalyst surfaces**

The above experimental results and MD analyses suggested that the proper surface molecular pump on Pt facilitates the influx of $O_2$ and outflux of water, which leads to increased

$O_2$ surface concentration and reduced $H_2O$ concentration, and sustainably higher ORR activity. We note that this surface molecular pump is following Le Chatelier's principle, which is fundamentally different and may work independently from strategies used in modifying the electronic structures of the catalyst surface. Therefore, we expect that such effects can work synergistically to further enhance the SA of Pt-alloy catalysts beyond the limits using the Sabatier principle. To this end, we prepared the PtCuNi catalyst using a modified method reported previously[21] and applied the same surface modification protocol. The overall average size, composition, and elemental distribution did not show noticeable change before and after modification (Figure 2. 13a-e, and Figure 2. 14a-e). Similar to Pt/C, the ECSA of modified PtCuNi catalysts decreased from 70 $m^2/g_{Pt}$ to 49 $m^2/g_{Pt}$ after 24 hours of modification and further decreased to 36 $m^2/g_{Pt}$ after 48 hours of modification (Figure 2. 15a and Figure 2. 16a). We noted that the morphology, size, composition, and structures of the modified catalysts remained overall unchanged compared to the original PtCuNi catalysts (Figure 2. 17a to e and Figure 2. 18a to e), suggesting that the decreased ECSA is dominantly attributed to increased DMF coverage, which is consistent with Pt/C model system discussed above (Figure 2. 16a).

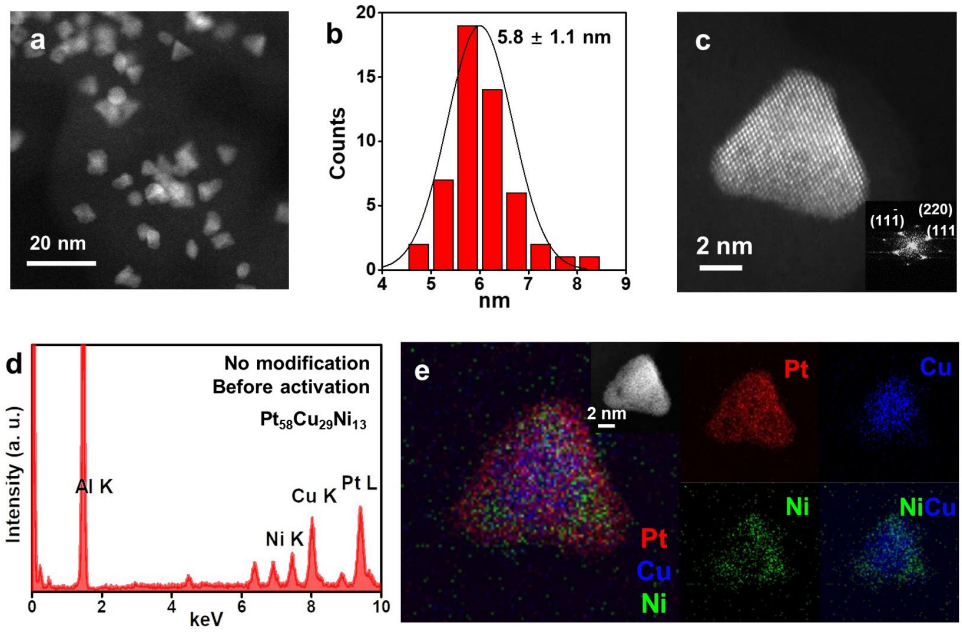


**Figure 2. 13** Characterization of original as-prepared PtCuNi catalysts. (a) Low-magnification STEM image of original as-prepared PtCuNi catalysts loaded on carbon black. (b) Size distribution of original as-prepared PtCuNi catalysts measured according to the edge of tetrahedral-shaped PtCuNi catalysts. (c) Atomic high-resolution HAADF-STEM image of as-prepared PtCuNi catalysts. (d) Representative EDX composition analysis of original as-prepared PtCuNi catalysts. (e) EDX mapping results of as-prepared PtCuNi catalysts, showing a Cu-rich core and PtNi shell.

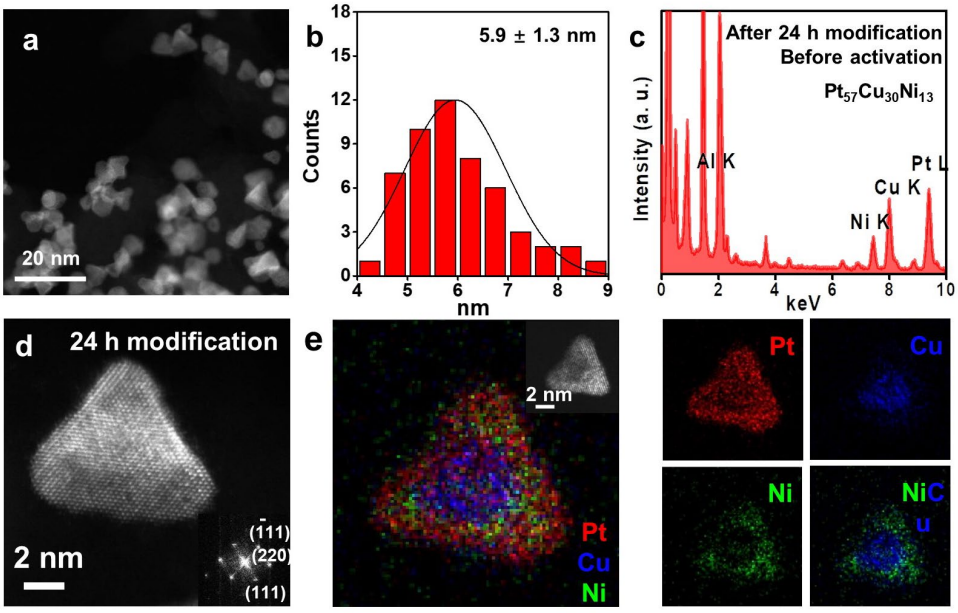


**Figure 2. 14** Characterization of surface-modified PtCuNi catalysts modified for 24 hours in DMF. (**a**) Low-magnification STEM image of surface-modified PtCuNi catalysts loaded on carbon black.

(**b**) Size distribution of surface-modified PtCuNi catalysts measured according to the edge of tetrahedral shaped PtCuNi catalysts. (**c**) Representative EDX composition analysis of surface-modified PtCuNi catalysts. (**d**) High-resolution atomic STEM image of surface-modified Petunia catalyst. (**e**) Representative EDX elemental mapping results of surface-modified PtCuNi catalysts, suggesting no obvious elemental distribution change.

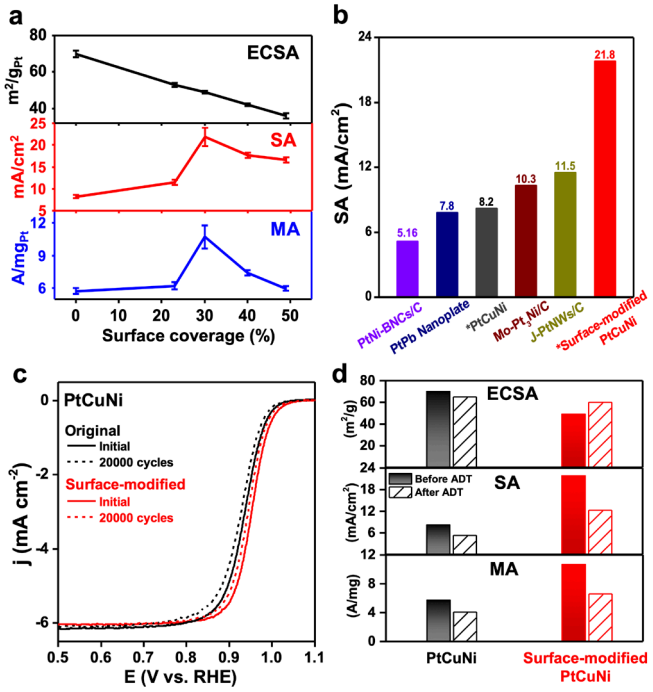


**Figure 2. 15** Performance of PtCuNi catalysts with and without DMF. a, The evolution of ECSA (black), SA (red), and MA (blue) with DMF surface coverage. b, Comparison of SA for optimal surface-modified PtCuNi catalysts and state-of-the-art ORR catalysts. References: PtNi-BNCs/C[43], PtPt Nanoplate[44], Mo-$Pt_3Ni$/C[45], J-PtNWs[46]. *PtCuNi and *Surface-modified PtCuNi catalysts are from this work. c, ORR stability LSV curves for original PtCuNi catalysts (black) and optimal surface-modified PtCuNi catalysts (red) before (black solid line and red solid line) and after (black dashed line and red dashed line) 20,000 cycles. d, ECSA, SA, and MA comparisons of PtCuNi catalysts and surface-modified PtCuNi catalysts before and after ADT.

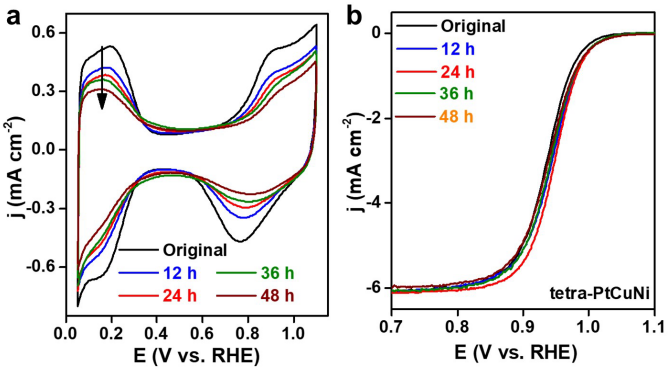

**Figure 2. 16** Electrochemical measurements of PtCuNi catalysts. (a) CV comparison of PtCuNi catalysts at different modification time: original (black), 12 hours modification time (blue), 24 hours modification time (red), 36 hours modification time (green), 48 hours modification time (wine). (b) LSV comparison of PtCuNi catalysts at different modification time: original (black), 12 hours modification time (blue), 24 hours modification time (red), 36 hours modification time (green), 48 hours modification time (wine).

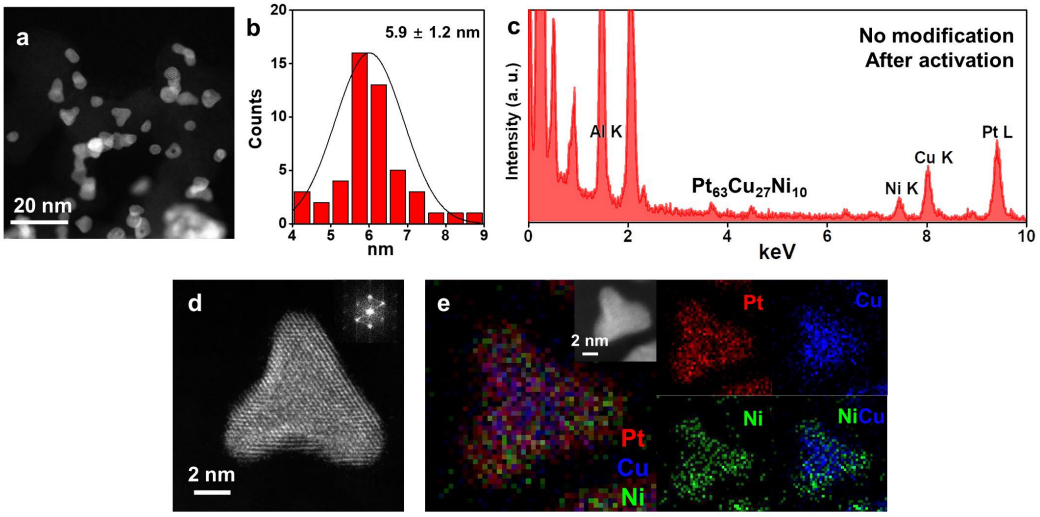


**Figure 2. 17** Characterization of original PtCuNi catalysts after activation. (a) Low-magnification STEM image of original PtCuNi catalysts after activation. (b) Size distribution of original PtCuNi catalysts after activation measured according to the edge of tetrahedral shaped PtCuNi catalysts. (c) Representative EDX composition analysis of original PtCuNi catalysts after activation. (d) Atomic high-resolution HAADF-STEM image of original PtCuNi catalysts after activation. (e) EDX mapping results of original PtCuNi catalysts after activation.

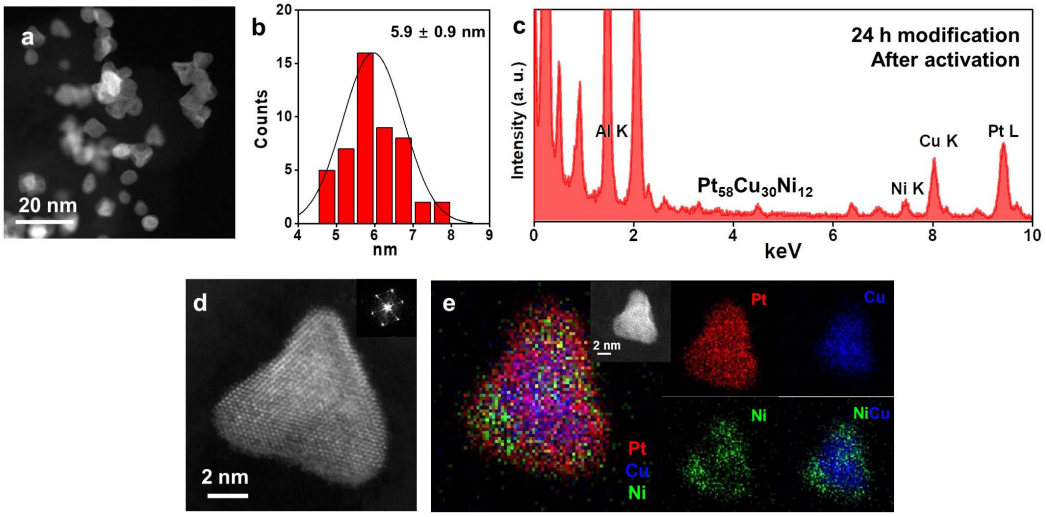

**Figure 2. 18** Characterization of surface-modified PtCuNi catalysts after activation. (a) Low-magnification STEM image of surface-modified PtCuNi catalysts after activation. (b) Size distribution of surface-modified PtCuNi catalysts after activation measured according to the edge of tetrahedral shaped PtCuNi catalysts. (c) Representative EDX composition analysis of surface-modified PtCuNi catalysts after activation. (d) Atomic high-resolution HAADF-STEM image of surface-modified PtCuNi catalysts after activation. (e) EDX mapping results of surface-modified PtCuNi catalysts after activation.

We further evaluated the ORR activity of surface-modified PtCuNi catalysts (Figure 2. 16b) and found the optimal surface-modified PtCuNi catalysts exhibited an unprecedented high SA of 21.8 ± 2.1 mA/cm$^2$ and an ultrahigh MA of 10.7 ± 1.1 A/mg$_{Pt}$ at 0.9 V vs. RHE (Figure 2. 15a), which are ca. 2.6 times and 1.9 times those of original PtCuNi catalysts (8.2 ± 0.4 mA/cm$^2$ and 5.7 ± 0.3 A/mg$_{Pt}$) and ca. 45.4 times and 46.5 times those of Pt/C catalysts (0.48 ± 0.06 mA/cm$^2$ and 0.23 ± 0.03 A/mg$_{Pt}$). The SA of our surface-modified PtCuNi catalysts outperforms all current state-of-the-art catalysts and nearly doubles the SA performance of previous reported J-PtNWs (11.5 mA/cm$^2$)[46] (Figure 2. 15b and Table 2. 1).

We further evaluated the durability of the surface-modified PtCuNi catalysts and original PtCuNi catalysts by conducting 20,000 cycles of accelerated degradation test (ADT) and performing postmortem characterizations. After ADT, the surface-modified PtCuNi catalysts still showed a highly respectable SA and MA of 12.3 mA/cm$^2$ and 6.6 A/mg$_{Pt}$ (Figure 2. 15c and Table 2. 1), respectively, exceeding the initial performance of unmodified PtCuNi catalysts, which is also much higher than the as-prepared PtCuNi catalysts after ADT (SA of 5.3 mA/cm$^2$, MA of 4.1 A/mg$_{Pt}$). Interestingly, despite similar size after ADT (Figure 2. 19 and 20), the surface-modified PtCuNi catalyst showed ECSA retention of 123%, which is higher than that of original PtCuNi catalysts (93%). This high number may be associated with partial stripping of the surface-adsorbed molecules (DMF) during long-term ADT cycling, exposing more available Pt sites. At the beginning of the reaction, the introduction of the surface molecular pump sacrifices ECSA while

boosting SA (or turn over frequency per site) to achieve a high MA. With the progress of the reaction, while the SA of the catalyst decreases with stripped ligands its ECSA recovers in order to maintain a decent MA after ADT. This suggests the surface modification can effectively extend the lifetime of catalysts while maintaining performance.

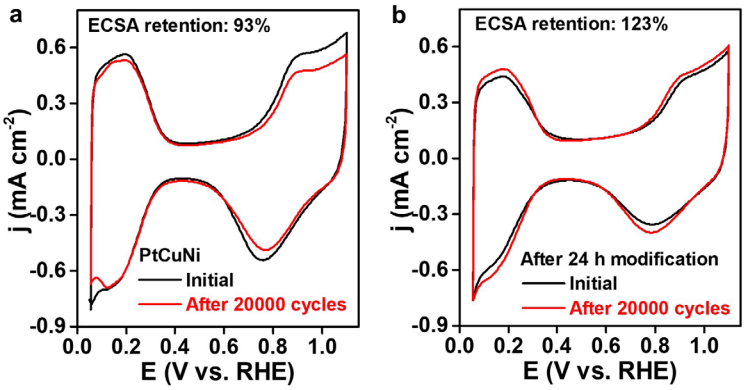


**Figure 2. 19** Comparison of ECSA change of original PtCuNi catalysts (left) and suface-modified PtCuNi catalysts (right). (**a**) CV comparison of original PtCuNi catalysts before (black) and after (red), showing 7% loss of ECSA after 20,000 cycles. (**b**) CV comparison of surface-modified PtCuNi catalysts before (black) and after (red), showing a 23% increase of ECSA after 20,000 cycles.

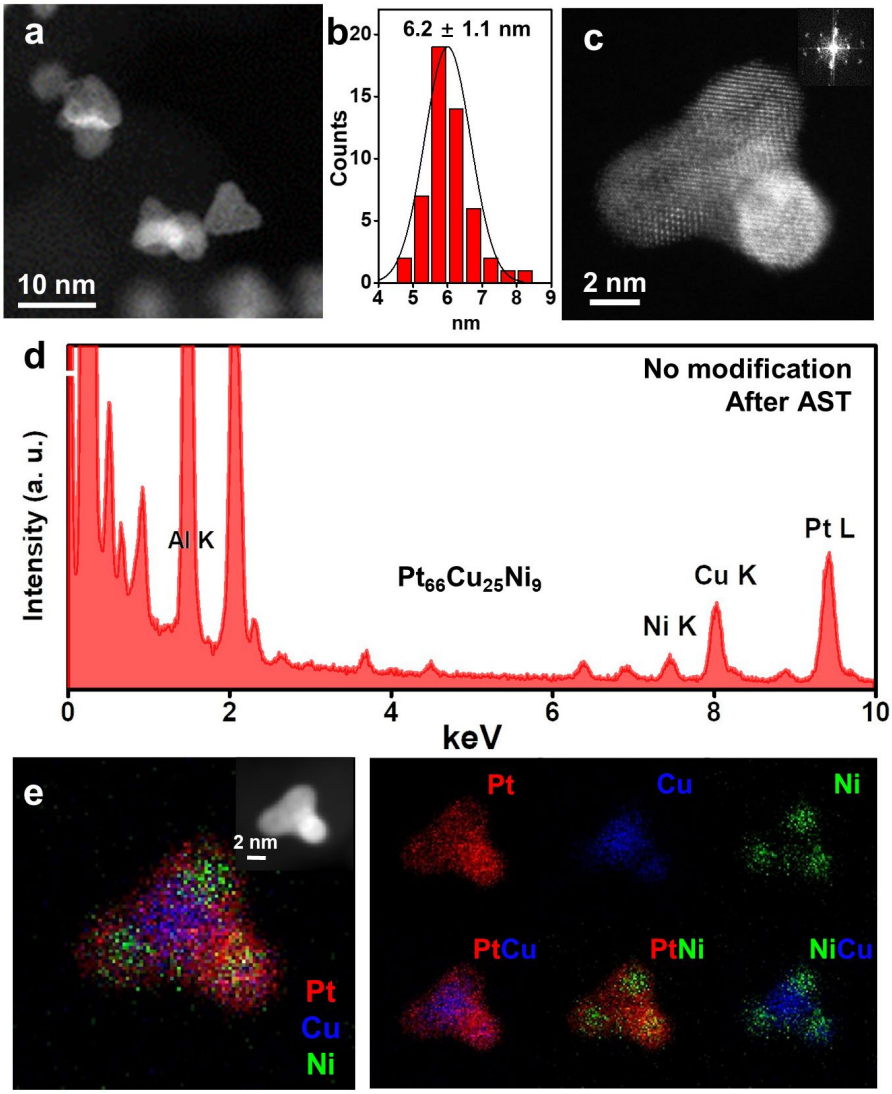


**Figure 2. 20** Characterization of original PtCuNi catalysts after ADT. (a) Low-magnification STEM image of original PtCuNi catalysts after ADT. (b) Size distribution of original PtCuNi catalysts after ADT measured according to the edge of tetrahedral shaped PtCuNi catalysts. (c) Atomic high-resolution HAADF-STEM image of original PtCuNi catalysts after activation. (d) Representative EDX composition analysis of original PtCuNi catalysts after ADT. (e) EDX mapping results of original PtCuNi catalysts after activation.

| Catalyst | SA (mA/cm²) | | MA (A/mg$_{Pt}$) | | ECSA (m²/g$_{Pt}$) | ADT cycles |
|---|---|---|---|---|---|---|
| | BOL | ADT | BOL | ADT | | |
| Surface-modified PtCuNi (this work) | 21.8 | 12.3 | 10.7 | 6.6 | 49 | 20,000 |

| | | | | | | |
|---|---|---|---|---|---|---|
| As-prepared PtCuNi (this work) | 8.2 | 5.3 | 5.7 | 4.1 | 70 | 20,000 |
| $Pt_3Ni$ nanoframe[47] | 8.4* | NA | 5.7 | NA | 67.2 | 10,000 |
| PtNi-BNCs/C[43] | 5.16 | 5.15* | 3.52 | 3.47 | 68.2 | 50,000 |
| fct-Pt-Co@Pt octahedron[48] | 9.16 | 7.21 | 2.82 | 2.23 | 30.8 | 30,000 |
| PtPb nanoplate[44] | 7.8 | 7.0 | 4.3 | 3.97 | 55.0 | 50,000 |
| PtNi/Ni–B/C[49] | 9.05 | NA | 5.3 | NA | 59 | 5,000 |
| J-PtNWs[46] | 11.5 | 10.9* | 13.6 | 12.0 | 118 | 6,000 |

**Table 2. 1** RDE performance of surface-modified PtCuNi catalysts in comparison to those in several representative reports. BOL: the beginning of life, ADT: accelerated degradation test, NA: not available, * calculated from the literature.

### 2.4 Conclusion

In summary, we reported that the surface modification can greatly enhance the ORR activity of Pt-based catalysts by interrupting the surface water adlayer network and hence facilitating the influx of $O_2$ and outflux of $H_2O$ at the catalyst-electrolyte interface, functioning as a surface molecular pump to promote the reaction. In specific, combining experimental design and accurate MD simulation, we found that DMF-modified Pt surfaces lower the $O_2$ physisorption free energy leading to a 2-3 fold increase in local $O_2$ concentration and hence a 2-3 fold increase in SA towards ORR, following the Le Chatelier's principle. We further showed that this effect can be used independently and in conjunction with the Sabatier principle (strain-ligand effect). Accordingly, we demonstrated a record-high SA of 21.8 ± 2.1 mA/cm$^2$ (at 0.9 V vs. RHE) on DMF-modified PtCuNi. This study opens new exciting avenues to modulate catalytic activities through designing and constructing local environments at the molecular level that enhance reaction kinetics at the catalyst-electrolyte interface.

## 2.5 References


1. Seh, Z. W.; Kibsgaard, J.; Dickens, C. F.; Chorkendorff, I.; Nørskov, J. K.; Jaramillo, T. F., Combining theory and experiment in electrocatalysis: Insights into materials design. *Science* **2017,** *355* (6321), eaad4998.

2. Strasser, P.; Koh, S.; Anniyev, T.; Greeley, J.; More, K.; Yu, C.; Liu, Z.; Kaya, S.; Nordlund, D.; Ogasawara, H.; Toney, M. F.; Nilsson, A., Lattice-strain control of the activity in dealloyed core–shell fuel cell catalysts. *Nat. Chem.* **2010,** *2* (6), 454-460.

3. Stamenkovic, V. R.; Fowler, B.; Mun, B. S.; Wang, G.; Ross, P. N.; Lucas, C. A.; Marković, N. M., Improved oxygen reduction activity on $Pt_3Ni(111)$ via increased surface site availability. *Science* **2007,** *315* (5811), 493.

4. Cui, C.; Gan, L.; Heggen, M.; Rudi, S.; Strasser, P., Compositional segregation in shaped Pt alloy nanoparticles and their structural behaviour during electrocatalysis. *Nat. Mater.* **2013,** *12* (8), 765-771.

5. Chung, D. Y.; Jun, S. W.; Yoon, G.; Kwon, S. G.; Shin, D. Y.; Seo, P.; Yoo, J. M.; Shin, H.; Chung, Y.-H.; Kim, H.; Mun, B. S.; Lee, K.-S.; Lee, N.-S.; Yoo, S. J.; Lim, D.-H.; Kang, K.; Sung, Y.-E.; Hyeon, T., Highly durable and active PtFe nanocatalyst for electrochemical oxygen reduction reaction. *J. Am. Chem. Soc.* **2015,** *137* (49), 15478-15485.

6. Li, J.; Sharma, S.; Liu, X.; Pan, Y.-T.; Spendelow, J. S.; Chi, M.; Jia, Y.; Zhang, P.; Cullen, D. A.; Xi, Z.; Lin, H.; Yin, Z.; Shen, B.; Muzzio, M.; Yu, C.; Kim, Y. S.; Peterson, A. A.; More, K. L.; Zhu, H.; Sun, S., Hard-magnet L10-CoPt nanoparticles advance fuel cell catalysis. *Joule* **2019,** *3* (1), 124-135.

7. Han, B.; Carlton, C. E.; Kongkanand, A.; Kukreja, R. S.; Theobald, B. R.; Gan, L.; O'Malley, R.; Strasser, P.; Wagner, F. T.; Shao-Horn, Y., Record activity and stability of dealloyed

bimetallic catalysts for proton exchange membrane fuel cells. *Energy Environ. Sci.* **2015,** *8* (1), 258-266.

8. Escudero-Escribano, M.; Malacrida, P.; Hansen, M. H.; Vej-Hansen, U. G.; Velázquez-Palenzuela, A.; Tripkovic, V.; Schiøtz, J.; Rossmeisl, J.; Stephens, I. E. L.; Chorkendorff, I., Tuning the activity of Pt alloy electrocatalysts by means of the lanthanide contraction. *Science* **2016,** *352* (6281), 73-76.

9. Stamenkovic, V.; Mun, B. S.; Mayrhofer, K. J. J.; Ross, P. N.; Markovic, N. M.; Rossmeisl, J.; Greeley, J.; Nørskov, J. K., Changing the activity of electrocatalysts for oxygen reduction by tuning the surface electronic structure. *Angew. Chem. Int. Ed.* **2006,** *45* (18), 2897-2901.

10. Rumble, J. R., CRC Handbook of Chemistry and Physics, 101st Edition. Abingdon. CRC Press: 2020.

11. Wang, S. Y.; Zhu, E. B.; Huang, Y.; Heinz, H., Direct correlation of oxygen adsorption on platinum-electrolyte interfaces with the activity in the oxygen reduction reaction. *Science Advances* **2021,** *7* (24), eabb1435.

12. Benn, E.; Uvegi, H.; Erlebacher, J., Characterization of nanoporous metal-ionic liquid composites for the electrochemical oxygen reduction reaction. *J. Electrochem. Soc.* **2015,** *162* (10), H759-H766.

13. Snyder, J.; Fujita, T.; Chen, M. W.; Erlebacher, J., Oxygen reduction in nanoporous metal–ionic liquid composite electrocatalysts. *Nat. Mater.* **2010,** *9* (11), 904-907.

14. Favero, S.; Stephens, I. E. L.; Titirici, M. M., Engineering the electrochemical interface of oxygen reduction electrocatalysts with ionic liquids: a review. *Adv. Energy Sustainability Res.* **2021,** *2* (1), 2000062.

15. Strmcnik, D.; Kodama, K.; van der Vliet, D.; Greeley, J.; Stamenkovic, V. R.; Marković, N. M., The role of non-covalent interactions in electrocatalytic fuel-cell reactions on platinum. *Nature Chemistry* **2009,** *1* (6), 466-472.

16. Lu, L.; Wang, Z.; Zou, S.; Zhou, Y.; Hong, W.; Li, R.; Xiao, L.; Liu, J.; Gong, X.-Q.; Fan, J., Ligand-mediated bifunctional catalysis for enhanced oxygen reduction and methanol oxidation tolerance in fuel cells. *J. Mater. Chem. A* **2018,** *6* (39), 18884-18890.

17. Zorko, M.; Farinazzo Bergamo Dias Martins, P.; Connell, J. G.; Lopes, P. P.; Markovic, N. M.; Stamenkovic, V. R.; Strmcnik, D., Improved rate for the oxygen reduction reaction in a sulfuric acid electrolyte using a Pt(111) surface modified with melamine. *ACS Appl. Mater. Interfaces* **2021,** *13* (2), 3369-3376.

18. Kumeda, T.; Hoshi, N.; Nakamura, M., Effect of Hydrophobic Cations on the Inhibitors for the Oxygen Reduction Reaction on Anions and Ionomers Adsorbed on Single-Crystal Pt Electrodes. *ACS Appl. Mater. Interfaces* **2021,** *13* (13), 15866-15871.

19. Chen, R.; McAllister, A. B.; Shen, M., Detection of zwitterion at an electrified liquid-liquid interface: A chemical equilibrium perspective. *J. Electroanal. Chem.* **2020,** *873*, 114303.

20. Zhu, E. B.; Xue, W.; Wang, S. Y.; Yan, X. C.; Zhou, J. X.; Liu, Y.; Cai, J.; Liu, E. S.; Jia, Q. Y.; Duan, X. F.; Li, Y. J.; Heinz, H.; Huang, Y., Enhancement of oxygen reduction reaction activity by grain boundaries in platinum nanostructures. *Nano Res* **2020,** *13* (12), 3310-3314.

21. Huang, J.; Liu, Y.; Xu, M.; Wan, C.; Liu, H.; Li, M.; Huang, Z.; Duan, X.; Pan, X.; Huang, Y., PtCuNi tetrahedra catalysts with tailored surfaces for efficient alcohol oxidation. *Nano Lett.* **2019,** *19* (8), 5431-5436.

22. Dassault Systèmes BIOVIA, Materials Studio, v7.0.200, San Diego: Dassault Systèmes, 2013.

23. Heinz, H.; Lin, T. J.; Mishra, R. K.; Emami, F. S., Thermodynamically consistent force fields for the assembly of inorganic, organic, and biological nanostructures: the INTERFACE force field. *Langmuir* **2013,** *29* (6), 1754-65.

24. Heinz, H.; Vaia, R. A.; Farmer, B. L.; Naik, R. R., Accurate simulation of surfaces and interfaces of face-centered cubic metals using 12−6 and 9−6 Lennard-Jones potentials. *J. Phys. Chem. C* **2008,** *112* (44), 17281-17290.

25. Wang, S.; Hou, K.; Heinz, H., Accurate Compatible Force Fields for Molecular Oxygen, Nitrogen and Hydrogen to Simulate Heterogeneous Electrolytes and Interfaces. *J. Chem. Theor. Comput.* **2021,** *17* (8), 5198-5213.

26. Mark, L. O.; Zhu, C.; Medlin, J. W.; Heinz, H., Understanding the Surface Reactivity of Ligand-Protected Metal Nanoparticles for Biomass Upgrading. *ACS Catalysis* **2020,** *10* (10), 5462-5474.

27. Geada, I. L.; Ramezani-Dakhel, H.; Jamil, T.; Sulpizi, M.; Heinz, H., Insight into induced charges at metal surfaces and biointerfaces using a polarizable Lennard-Jones potential. *Nat Commun* **2018,** *9* (1), 716.

28. Ruan, L.; Ramezani-Dakhel, H.; Chiu, C. Y.; Zhu, E.; Li, Y.; Heinz, H.; Huang, Y., Tailoring molecular specificity toward a crystal facet: a lesson from biorecognition toward Pt{111}. *Nano Lett* **2013,** *13* (2), 840-6.

29. Heinz, H.; Farmer, B. L.; Pandey, R. B.; Slocik, J. M.; Patnaik, S. S.; Pachter, R.; Naik, R. R., Nature of Molecular Interactions of Peptides with Gold, Palladium, and Pd-Au Bimetal Surfaces in Aqueous Solution. *J. Am. Chem. Soc.* **2009,** *131* (28), 9704-9714.

30. Ramezani-Dakhel, H.; Ruan, L. Y.; Huang, Y.; Heinz, H., Molecular Mechanism of Specific Recognition of Cubic Pt Nanocrystals by Peptides and the Concentration-Dependent Formation from Seed Crystals. *Adv. Funct. Mater.* **2015,** *25*, 1374-1384.

31. Phillips, J. C.; Braun, R.; Wang, W.; Gumbart, J.; Tajkhorshid, E.; Villa, E.; Chipot, C.; Skeel, R. D.; Kalé, L.; Schulten, K., Scalable molecular dynamics with NAMD. *J. Comput. Chem.* **2005,** *26* (16), 1781-1802.

32. Michaud-Agrawal, N.; Denning, E. J.; Woolf, T. B.; Beckstein, O., MDAnalysis: A toolkit for the analysis of molecular dynamics simulations. *J. Comput. Chem.* **2011,** *32* (10), 2319-2327.

33. Gowers, R. J., Linke, Max, Barnoud, Jonathan, Reddy, Tyler John Edward, Melo, Manuel N., Seyler, Sean L., Domanski, Jan, Dotson, David L., Buchoux Sébastien, Kenney, Ian M. , Beckstein Oliver MDAnalysis: A Python Package for the Rapid Analysis of Molecular Dynamics Simulations. In *in Proceedings of the 15th Python in Science Conference. (SciPy Austin, TX, 2016), vol. 98.*, 2016.

34. Schwierz, N.; Frost, C. V.; Geissler, P. L.; Zacharias, M., Dynamics of Seeded Abeta40-Fibril Growth from Atomistic Molecular Dynamics Simulations: Kinetic Trapping and Reduced Water Mobility in the Locking Step. *J Am Chem Soc* **2016,** *138* (2), 527-39.

35. Plimpton, S., Fast parallel algorithms for short-range molecular dynamics. *J. Comput. Phys.* **1995,** *117* (1), 1-19.

36. Appendix B: Tables of Physical Data. In *Fundamentals and Applications of Organic Electrochemistry*, 2014; pp 217-222.

37. Fuchigami, T.; Inagi, S.; Atobe, M., *Fundamentals and applications of organic electrochemistry: synthesis, materials, devices*. 2015; p 1-226.

38. Wang, J.; Cheng, T.; Fenwick, A. Q.; Baroud, T. N.; Rosas-Hernández, A.; Ko, J. H.; Gan, Q.; Goddard Iii, W. A.; Grubbs, R. H., Selective $CO_2$ electrochemical reduction enabled by a tricomponent copolymer modifier on a copper surface. *J. Am. Chem. Soc.* **2021,** *143* (7), 2857-2865.

39. Pegis, M. L.; Wise, C. F.; Martin, D. J.; Mayer, J. M., Oxygen reduction by homogeneous molecular catalysts and electrocatalysts. *Chem. Rev.* **2018,** *118* (5), 2340-2391.

40. Herrebout, W. A.; Vanderveken, B. J.; Wang, A.; Durig, J. R., Enthalpy Differences between Conformers of n-Butane and the Potential Function Governing Conformational Interchange. *J. Phys. Chem.* **1995,** *99* (2), 578-585.

41. Chung, Y.-H.; Chung, D. Y.; Jung, N.; Sung, Y.-E., Tailoring the Electronic Structure of Nanoelectrocatalysts Induced by a Surface-Capping Organic Molecule for the Oxygen Reduction Reaction. *The Journal of Physical Chemistry Letters* **2013,** *4* (8), 1304-1309.

42. George, M.; Zhang, G.-R.; Schmitt, N.; Brunnengräber, K.; Sandbeck, D. J. S.; Mayrhofer, K. J. J.; Cherevko, S.; Etzold, B. J. M., Effect of Ionic Liquid Modification on the ORR Performance and Degradation Mechanism of Trimetallic PtNiMo/C Catalysts. *ACS Catal.* **2019,** *9* (9), 8682-8692.

43. Tian, X.; Zhao, X.; Su, Y.-Q.; Wang, L.; Wang, H.; Dang, D.; Chi, B.; Liu, H.; Hensen, E. J. M.; Lou, X. W.; Xia, B. Y., Engineering bunched Pt-Ni alloy nanocages for efficient oxygen reduction in practical fuel cells. *Science* **2019,** *366* (6467), 850.

44. Bu, L.; Zhang, N.; Guo, S.; Zhang, X.; Li, J.; Yao, J.; Wu, T.; Lu, G.; Ma, J.-Y.; Su, D.; Huang, X., Biaxially strained PtPb/Pt core/shell nanoplate boosts oxygen reduction catalysis. *Science* **2016,** *354* (6318), 1410.

45. Huang, X.; Zhao, Z.; Cao, L.; Chen, Y.; Zhu, E.; Lin, Z.; Li, M.; Yan, A.; Zettl, A.; Wang, Y. M.; Duan, X.; Mueller, T.; Huang, Y., High-performance transition metal–doped $Pt_3Ni$ octahedra for oxygen reduction reaction. *Science* **2015,** *348* (6240), 1230.

46. Li, M.; Zhao, Z.; Cheng, T.; Fortunelli, A.; Chen, C.-Y.; Yu, R.; Zhang, Q.; Gu, L.; Merinov, B. V.; Lin, Z.; Zhu, E.; Yu, T.; Jia, Q.; Guo, J.; Zhang, L.; Goddard, W. A.; Huang, Y.; Duan, X., Ultrafine jagged platinum nanowires enable ultrahigh mass activity for the oxygen reduction reaction. *Science* **2016,** *354* (6318), 1414.

47. Chen, C.; Kang, Y.; Huo, Z.; Zhu, Z.; Huang, W.; Xin, H. L.; Snyder, J. D.; Li, D.; Herron, J. A.; Mavrikakis, M.; Chi, M.; More, K. L.; Li, Y.; Markovic, N. M.; Somorjai, G. A.; Yang, P.; Stamenkovic, V. R., Highly crystalline multimetallic nanoframes with three-dimensional electrocatalytic surfaces. *Science* **2014,** *343* (6177), 1339.

48. Xie, M.; Lyu, Z.; Chen, R.; Shen, M.; Cao, Z.; Xia, Y., Pt–Co@Pt octahedraln nanocrystals: enhancing their activity and durability toward oxygen reduction with an intermetallic core and an ultrathin shell. *J. Am. Chem. Soc.* **2021,** *143* (22), 8509-8518.

49. He, D.; Zhang, L.; He, D.; Zhou, G.; Lin, Y.; Deng, Z.; Hong, X.; Wu, Y.; Chen, C.; Li, Y., Amorphous nickel boride membrane on a platinum–nickel alloy surface for enhanced oxygen reduction reaction. *Nat. Commun.* **2016,** *7* (1), 12362.

# Chapter 3. Ultralow loading 1D PtCo nanowires as cathode catalysts for high-performance PEMFCs

## 3.1 Introduction

Proton-exchange membrane fuel cells (PEMFCs) represent an attractive and sustainable power generation technology in automotive applications[1-3]. Although platinum group metal (PGM) materials represent the most efficient catalysts facilitating the sluggish oxygen reduction reaction (ORR) in PEMFCs[2, 4], the high cost of Pt and related components has severely impeded the broad dissemination of PEMFCs[5-6]. In principle, it is highly desirable to minimize the usage of Pt while achieving high performance. The Department of Energy (DOE) has set a beginning of life (BOL) mass activity (MA) target of 0.44 A/$mg_{PGM}$ and a total loading target of 0.125 $mg_{PGM}/cm^2$ by 2020, and planned to further lower the loading to 0.1 $mg_{PGM}/cm^2$[6-7]. To this end, developing practical high-performance ORR catalysts for a MEA with high MA and high power density is essential for minimizing Pt usage[3, 8-9]. In general, Pt-alloy catalysts show much improved catalytic activity than pure Pt in RDE measurements owing to their adjusted Pt-O binding strength[10-13]. However, the higher activity does not necessarily translate directly to MEA. In addition, reducing the PGM loading while keeping the power density performance and stability adds more challenges due to the more severe mass transport issues and harsher testing conditions in MEA[3, 6, 14]. Large losses of power density were widely observed for cells with low Pt loadings (< 0.1 $mg/cm^2$) due to the decreasing Pt roughness factor (r.f., units of $cm^2_{Pt}/cm^2_{MEA}$) and the consequently increasing $O_2$ transport resistance[3, 6, 14]. In essence, to decrease loading while maintaining the same catalyst layer thickness, the interparticle distance became larger, leading to a faster Pt dissolution rate and worse structural stability[14]. This represents an intrinsic dilemma for currently low PGM loading MEAs: i.e. the decrease in usage of Pt usually comes with a substantial sacrifice in power density and

stability that leads to low Pt utilization. Therefore, it is of primary importance to design catalysts to overcome the above said dilemma.

One-dimensional (1D) nanostructures can simultaneously achieve high ECSA and MA, offering considerable potential for lowering the Pt loading in PEMFCs[15-16]. In addition, 1D nanostructures showed better structural stability than nanoparticles, which can effectively mitigate aggregation and dissolution[17] and can potentially help retain high power density at low PGM loading in MEA. Previously, the Jagged-Pt nanowires developed by Li et al. showed a record-high MA of 13.6 $A/mg_{Pt}$ towards ORR on the rotating disk electrode (RDE)[13]. During the electrochemical dealloying process, nanowires could maintain the 1D structure, proving its high structural stability. Bu et al. and Jiang et al. also prepared a series of Pt-alloy NWs, showing respectable activity and stability[18-19]. Despite promising performance reported for 1D catalysts in half-cell RDE measurements, the outstanding performance of this new generation of catalysts has not yet been incorporated and investigated in a MEA[2-3, 20-21]. Furthermore, low PGM loading MEA (e.g. $\leq 0.1$ $mg_{PGM}/cm^2$ planned by 2025)[6] has been rarely reported. Therefore, it is highly desirable to incorporate Pt-based nanowires into MEAs to fully demonstrate and capture their merit in practical PEMFCs with low Pt loading, owing to their demonstrated high MA and ECSA.

Herein, we demonstrated an ultralow Pt loading (total loading of 0.072 $mg_{Pt}/cm^2$) and high-performance MEA using ultrathin platinum-cobalt nanowires (PtCoNWs) as cathode catalysts. The PtCoNWs showed a high ECSA of 73.2 $m^2/g_{Pt}$ and achieved a unprecedented MA of $1.06 \pm 0.14$ $A/mg_{Pt}$ [0.9 $V_{iR\text{-}free}$] at the BOL stage in MEA. This MA is 3.3 times that of the commercial Pt/C (0.32 $A/mg_{Pt}$) and far surpasses the DOE 2020 target (0.44 $A/mg_{PGM}$). The PtCoNWs reached a peak power density of 1016 $mW/cm^2$, outperforming the PtNWs

(830 mW/cm$^2$) and Pt/C (773 mW/cm$^2$) with comparable Pt loading. After the AST, the PtCoNWs showed a respectable end of life (EOL) MA of 0.45 A/mg$_{Pt}$, remaining above the DOE 2020 BOL target.

### 3.2 Methods

#### Materials and chemicals

All chemicals were purchased from Sigma-Aldrich unless otherwise specified. Commercial Pt/C catalyst (10 wt% and 40 wt% Pt) were purchased from Alfa Aesar. Isopropanol (≥ 99.5%) were purchased from Fisher Scientific. All reagents were used as received without further purification. For MEA test, Ketjen-300J carbon was obtained from Lion Specialty Chemicals Co., Ltd. The deionized water (18 MΩ/cm) was obtained from an ultra-pure purification system (Milli-Q advantage A10). The Nafion HP membranes were purchased from fuel cell store.

#### Synthesis of PtCoNWs catalysts

In typical synthesis of PtCoNWs, 200 mg Pt(acac)$_2$ and 100 mg Co(acac)$_2$ were mixed with 675 mg glucose, 16mg W(CO)$_6$ and 150 mg PVP-10,000 in a glass vial, with 50 ml of oleylamine and octadecene (3:2 volume ratio) as co-solvent. The mixture was heated to 180 °C for 6 h to form as-prepared PtCo alloy nanowires. The resulting nanowires were collected via centrifuge at 3,000 r.p.m. for 10 min. After loading the nanowires on carbon (Kejten black), the catalysts were then annealed under 450 °C in argon/hydrogen (97:3) atmosphere for 6 h. After annealing, the resulting product was dealloyed in 0.5 M sulfuric acid at 80 °C for 4 hours and washed till the pH is neutral, then annealed in Ar/$H_2$ (3% $H_2$) atmosphere at 200 °C for 2 hours to obtain the final ultrafine PtCoNWs.

#### Synthesis of PtNWs catalysts

For comparison, PtNWs were also prepared via a similar synthesis and processing method. 200 mg $Pt(acac)_2$ and 100 mg $Co(acac)_2$ were mixed with 675 mg glucose, 16mg $W(CO)_6$ and 150 mg PVP-10,000 in a 250 ml glass vial, with 50 ml of oleylamine and octadecene (3:2 volume ratio) as co-solvent. The mixture was heated to 120 °C for 6 h to form Pt nanowires. The resulting nanowires were collected via centrifuge at 3,000 r.p.m. for 10 min. After loading the nanowires on carbon (Kejten black), the catalysts were then annealed under 400 °C in argon/hydrogen (97:3) atmosphere for 6 h. After annealing, the resulting product was dealloyed in 0.5 M sulfuric acid at 80 °C for 4 hours and washed till the pH is neutral, then annealed in $Ar/H_2$ (3% $H_2$) atmosphere at 200 °C for 2 hours to obtain the final ultrafine PtNWs.

**Structure and composition characterization**

Low magnification transmission electron microscopy (TEM) images were taken on a FEI T12 transmission electron microscope operated at 120 kV. High-resolution TEM images (HRTEM), energy-dispersive X-ray spectroscopy (EDX) line-scan file and the high-angle annular dark-field scanning transmission electron microscope (HAADF-STEM) images were taken on JEM-ARM300F Grand ARM transmission electron microscope operated at 300 kV. TEM samples were prepared by dropping ethanol dispersion of catalysts onto carbon-coated aluminum TEM grids. The elementary concentration of catalysts was determined by the inductively coupled plasma (ICP) atomic emission spectroscopy. The Pt loading the catalysts is determined by the catalyst before electrochemical ink preparation. The MEA loading is determined by ICP before and after the MA and power density measurement. In specific, 2 pieces of sprayed catalysts (2 $cm^2$) were cut and soaked in the aqua regia for one day and were used to prepare ICP solution for metal content measurement. The loading after the MEA measurements was also checked for the accuracy of our results.

**Electrochemical measurement**

A three-electrode cell system was used to conduct all electrochemical tests. The working electrode was a glassy carbon rotating disk electrode (RDE) with a 0.196 $cm^2$ glassy carbon geometry area from Pine Instruments. The counter and reference electrodes are Pt wire and Ag/AgCl (1 M $Cl^-$) were used respectively. The loading of the catalysts was controlled to be 7.5 $\mu g_{Pt}/cm^2$. Cyclic voltammetry (CV) activations were performed in $N_2$-saturated 0.1 M $HClO_4$ electrolyte with a potential scan rate of 100 mV/s. Electrochemical active surface area (ECSA) determined by $H_{upd}$ was calculated by integrating the hydrogen adsorption charge on the CV curve by taking a value of 210 $\mu C/cm^2$ for the adsorption of a hydrogen monolayer. Double-layer correction was also applied. Oxygen reduction reaction (ORR) was tested in an $O_2$-saturated 0.1 M $HClO_4$ electrolyte with a potential scan rate of 20 mV/s. The measurement temperature was set at 25 ℃ using a water bath 5-neck flask. The current density of the ORR polarization curve was iR corrected. The accelerated stress testing (AST) was done at room temperature in $O_2$-saturated 0.1 M $HClO_4$ solutions by applying CV sweep between 0.6 and 1.0 V versus RHE at a sweep rate of 100 mV/s for 10,000 cycles.

**MEA preparation and single fuel cell test**

The single fuel cell performance of the catalysts as the cathode was tested at an 850e Fuel Cell Test System (Scribner, USA). The MEAs with an active area of 5.0 $cm^2$ were fabricated using the catalyst-spray membrane method. Catalysts were incorporated into MEAs by direct ultrasonic spraying of a water/2-propanol based ink onto a Nafion HP membrane with desired loading. The anode loading was set to be 0.025 $mg_{Pt}/cm^2$. The mass activity was measured via measuring the current at 0.9 V (iR-free) in 150 kPa absolute pressure (abs) $H_2/O_2$ (80 °C, 100% RH, 835/2,000 sccm) with correction for measured $H_2$ crossover. The $H_2$-Air tests were measured under 150 $kPa_{abs}$

$H_2$/Air (80 °C, 100% RH, 835/2,000 sccm). The AST was conducted using the square wave method from 0.6 V to 0.95 V with 3 s hold time at each potential (150 $kPa_{abs}$, 80 °C, 100% RH, $H_2/N_2$ = 100/100 sccm). Rated power voltage = (77.6 / (22.1 + T(°C))) V, based on target of $Q/\Delta Ti$ = 1.45 kW/°C. [rated voltage = 0.76 V for 80 °C]. The Pt utilization was calculated by normalizing the rated power by total Pt loading.

**XAS data collection and analysis**

The electrode inks for the XAS electrodes were composed of ethanol, 5 wt % Nafion solution, and the catalyst powder. The ink was drop cast onto a carbon paper with a total catalyst loading about 8 $mg/cm^2$. The ADT samples for XAS were cycled on the carbon paper for 20,000 cycles at room temperature in $O_2$-saturated 0.1 M $HClO_4$ solutions by applying CV sweep between 0.6 and 1.1 V versus RHE at a sweep rate of 100 mV/s. The XAS experiments were conducted at room temperature in a previously described *in-situ* spectro-electrochemical half-cell in which a continuously $O_2$ purged 0.1 M $HClO_4$ aqueous solution was circulated[22], at the beamline ISS 6-BM and 8-ID in National Synchrotron Light Source II (NSLS-II) (Brookhaven National Laboratory, NY). Before transferred into the cell, the electrodes were conditioned in 0.1 M $HClO_4$ under vacuum for 40 minutes to remove surface oxides and contaminants. Potentiostatic control was maintained with an Autolab PGSTAT30 potentiostat (Metrohm USA, formerly Brinkman Instruments). Full range Pt $L_3$-edge and Co K-edge spectra were taken at various static potentials along the anodic sweep of the CV. Data were collected on the same electrode in transmission mode at the Pt $L_3$-edge, and fluorescence mode at the Co K-edge, with a Pt/Co reference foil positioned between the ionization chambers I2 and I3 as a reference. The voltage cycling limits were 0.05 to 1.00 V vs. RHE. Data collection was performed at the chosen potentials held during anodic sweeps. The electrode was fully cycled following each potential hold to clean the electrode surfaces after

each potential hold. Typical experimental procedures were utilized with details provided in our previous work[23]. The data were processed and fitted using the Ifeffit−based Athena[24] and Artemis[25] programs. Scans were calibrated, aligned, and normalized with background removed using the IFEFFIT suite[26]. The $\chi(R)$ were modeled using single scattering paths calculated by FEFF6[27].

### 3.3 Results and discussion

#### Structural and compositional characterizations

To prepare ultrathin PtCoNWs, PtCo alloy NWs were first prepared by reducing platinum(II) acetylacetonate [$Pt(acac)_2$] and cobalt(II) acetylacetonate [$Co(acac)_2$] in the mixed solvent of 1-octadecene and oleylamine according to a revised synthesis process reported previously[13]. The as-prepared PtCoNWs were then loaded onto carbon black (Ketjen black, denoted as KB), followed by annealing and acid dealloying processes to produce the final ultrathin PtCoNWs (Figure 3. 1). Transmission electron microscopy (TEM) and high-angle annular dark-field scanning transmission electron microscopy (HAADF-STEM) showed that the as-prepared PtCoNWs have a well-defined 1D structure (Figures 3. 1b, Figure 3. 2) with a typical length of 200-300 nm and an average diameter of $1.8 \pm 0.3$ nm (Figures 3. 2b). The average lattice spacing of 0.191 nm (Figure 3. 1d) derived from the fast Fourier transform (FFT) was attributed to the interplane distance of (200) plane of PtCo alloy. After annealing and dealloying, the resulting PtCoNWs maintained the ultrathin 1D structure (Figures 3. 1c, Figure 3. 3a) with an average diameter of $2.3 \pm 0.7$ nm (Figure 3. 3b). The enlarged diameter may be attributed to ripening during the treatment process. The average lattice spacings of 0.225 nm and 0.191 nm along the [011] zone axis were ascribed to (111) and (200) facets, respectively (Figure 3. 1e). Energy dispersive X-ray (EDX) line scan profiles and mapping results revealed that before annealing and

dealloying, the as-prepared PtCoNWs had a uniform Pt and Co elemental distribution throughout the nanowires (Figures 3. 1f, Figure 3. 2b) with a composition of ca $Pt_{67}Co_{33}$ (Figure 3. 2d and Table 3. 1). The composition of the final PtCoNWs became ca $Pt_{82}Co_{18}$ upon dealloying, indicating the loss of Co during the process (Table 3. 1), which is consistent with the inductively coupled plasma atomic emission spectroscopy (ICP-AES) results. The Pt loading of the PtCoNWs on carbon is determined to be 11.0% by ICP. Moreover, the dealloying process changed the composition distribution from uniformly distributed PtCo alloy NWs to compositional-segregated NWs with PtCo alloy core and Pt-rich skin. As shown in the EDX line scan profiles, the final PtCoNWs have a PtCo core and an ultrathin Pt-rich shell of 0.6 nm (Figure 3. 1g). The inverse FFT analysis suggested that the (111) lattice spacings are different at the core (0.216 nm) and the shell (0.227 nm) regions (Figure 3. 3e and f), indicating higher Pt content in the shell ($Pt_{99}Co_1$) than in the core ($Pt_{52}Co_{48}$) according to the Vegard's law, consistent with the EDX line scan profiles (Figure 3. 1g). We also prepared Pt nanowires (PtNWs) as reference sample following previously reported approach[13], which were subjected to the same treatment process performed on PtCoNWs. Similarly, PtNWs maintained the morphology after the annealing and acid washing with an average diameter of $1.8 \pm 0.5$ nm (Figure 3. 4).

The structural details of PtCoNWs were studied using *in-situ* XAS. The white line intensity of the x-ray absorption near-edge structure (XANES) spectrum of PtCoNWs (Figure 3. 5a) at the Pt $L_3$-edge decreased (red arrow) compared with that of Pt/C reference, indicating decreasing Pt d-band vacancies due to the formation of the PtCo alloy.[28] The extended x-ray absorption fine structure (EXAFS) fitting result showed the first-shell Pt-Pt bond length of PtCoNWs is 2.72 Å (Figure 3. 5c and Table 3. 2), which is about 1.1%

shorter than that in of Pt/C (2.75 Å). Furthermore, the degree of alloying of the bimetallic PtCoNWs structures was indicated by analyzing the extent of alloying (J factor) derived from the first-shell coordination numbers (CNs).[29] In PtCoNWs, the $J_{Pt}$ and $J_{Co}$ values were determined to be 1.3 and 1.0, respectively (Table 3. 2), which are higher than those expected for disordered alloyed structure (J = 1), indicating a well-mixed distribution of Pt and Co atoms.[30] These results showed that PtCoNWs possessed a high degree of alloying, which may promote ligand effect and mitigate Pt dissolution.[31-32]

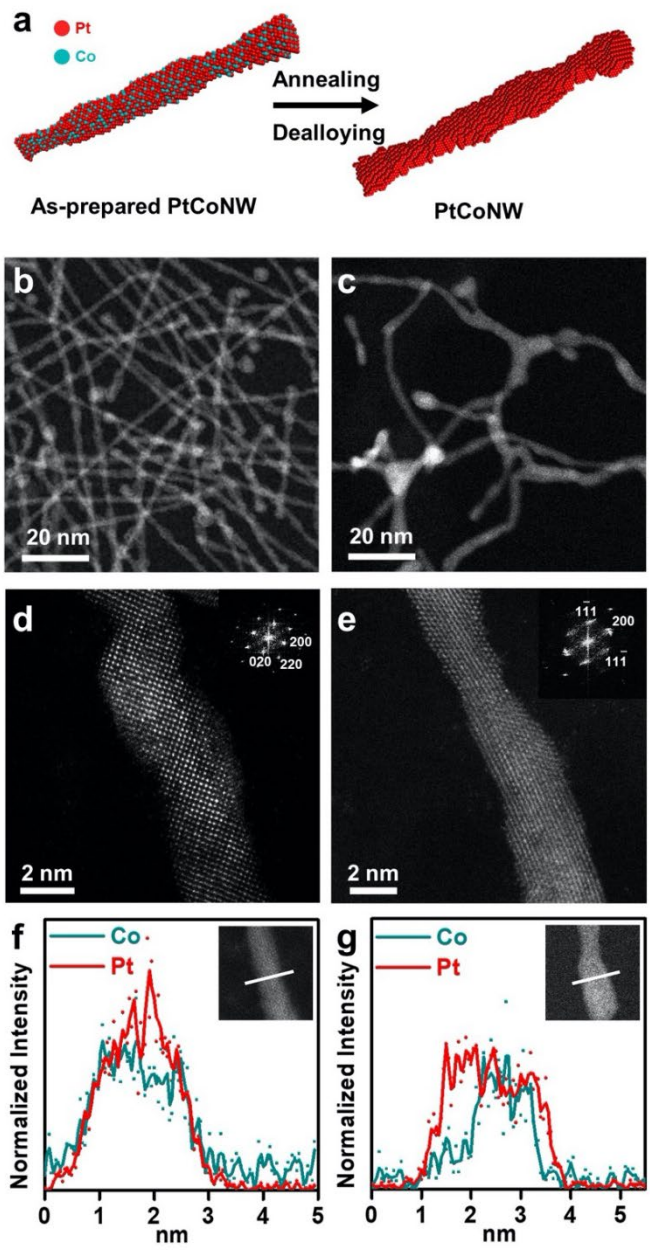


**Figure 3. 1** Structural and compositional characterizations of as-prepared PtCoNWs and ultrathin PtCoNWs after annealing and dealloying. (a) Schematic illustration of transformation from as-prepared alloy PtCoNWs to ultrathin PtCoNWs with a Pt-rich shell and PtCo-alloy core. (b and c) Representative HAADF-STEM images of as-prepared PtCoNWs and ultrathin PtCoNWs. (d and e) Atomic resolution STEM images of as-prepared PtCoNWs and ultrathin PtCoNWs, inset is the fast Fourier-transform pattern. (f and g) EDX spectroscopy line-scan profiles of as-prepared PtCoNWs and ultrathin PtCoNWs.

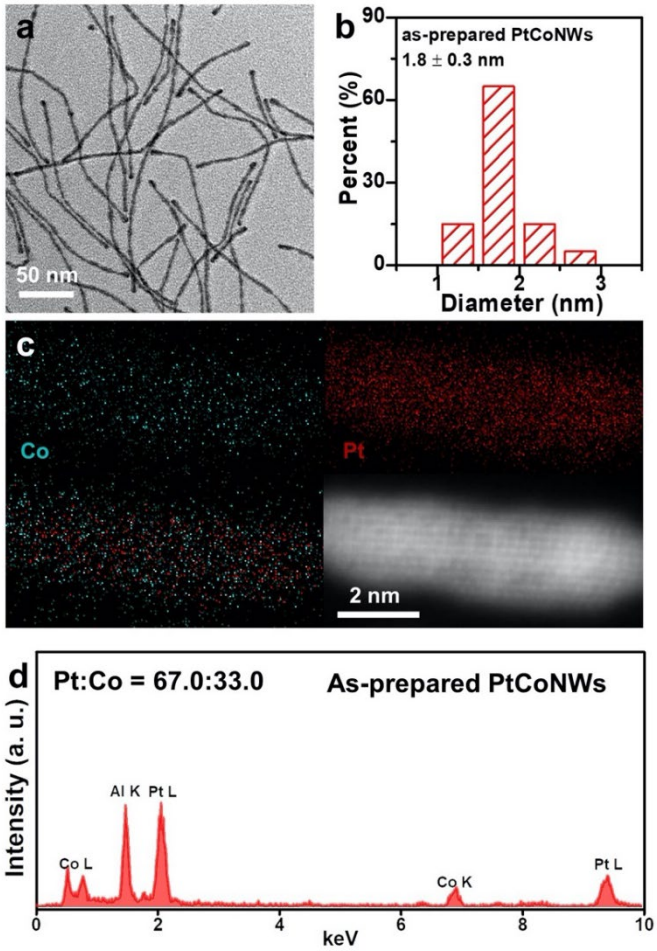


**Figure 3. 2** (**a**) TEM image of as-prepared PtCoNWs. (**b**) Size distribution of the as-prepared PtCoNWs. (**c**) EDX elemental mapping results of as-prepared PtCoNW. (**d**) Representative EDX spectrum of the as-prepared PtCoNWs.

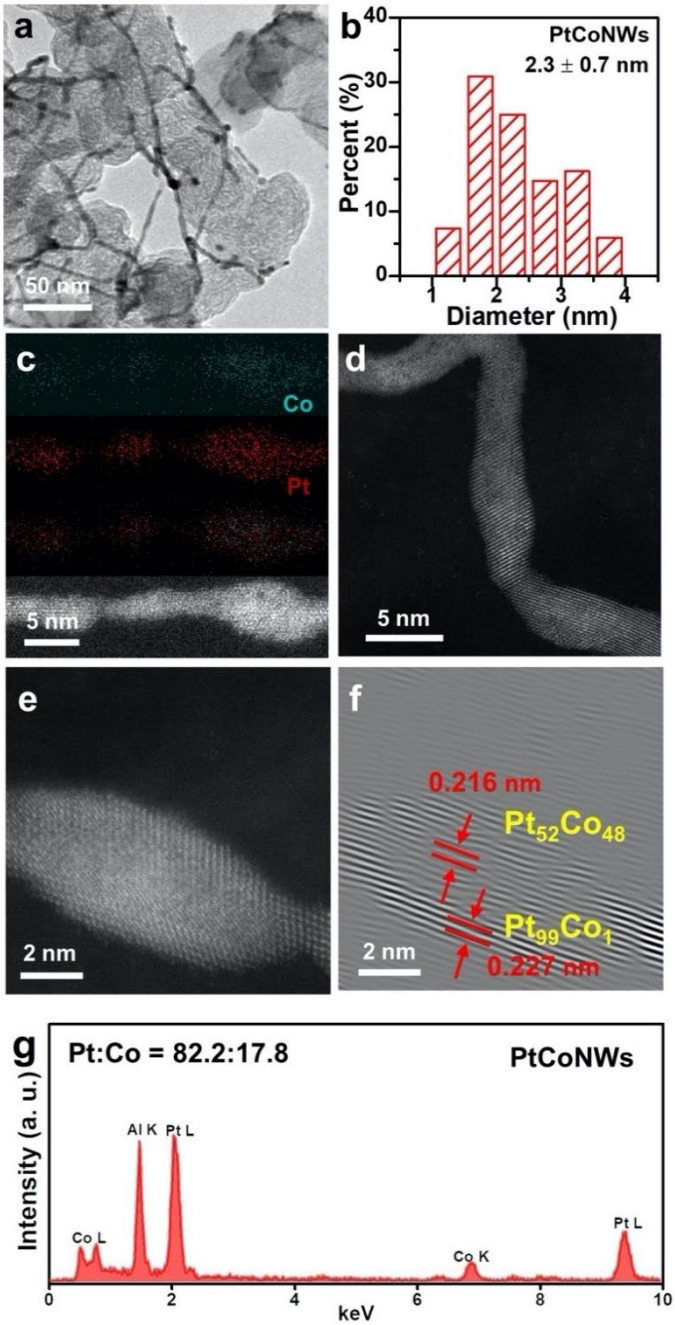


**Figure 3. 3** (**a**) TEM image of ultrathin PtCoNWs. (**b**) Size distribution of ultrathin PtCoNWs. (**c**) EDX elemental mapping of ultrathin PtCoNWs. (**d** and **e**) High-resolution STEM images. (**f**) Inverse FFT of the STEM in panel (**e**). (**g**) Representative EDX spectrum of the ultrathin PtCoNWs.

| Sample | EDX composition | |
|---|---|---|
| | Pt at.% | Co at.% |
| As-prepared PtCoNW | 67.0 ± 4.7 | 33.0 ± 4.7 |
| PtCoNW | 82.2 ± 2.9 | 17.8 ± 2.9 |
| PtCoNW before AST | 86.5 ± 2.6 | 13.5 ± 2.6 |
| PtCoNW after AST | 91.0 ± 1.8 | 9.0 ± 1.8 |

**Table 3. 1** Composition of PtCoNWs at different stages.

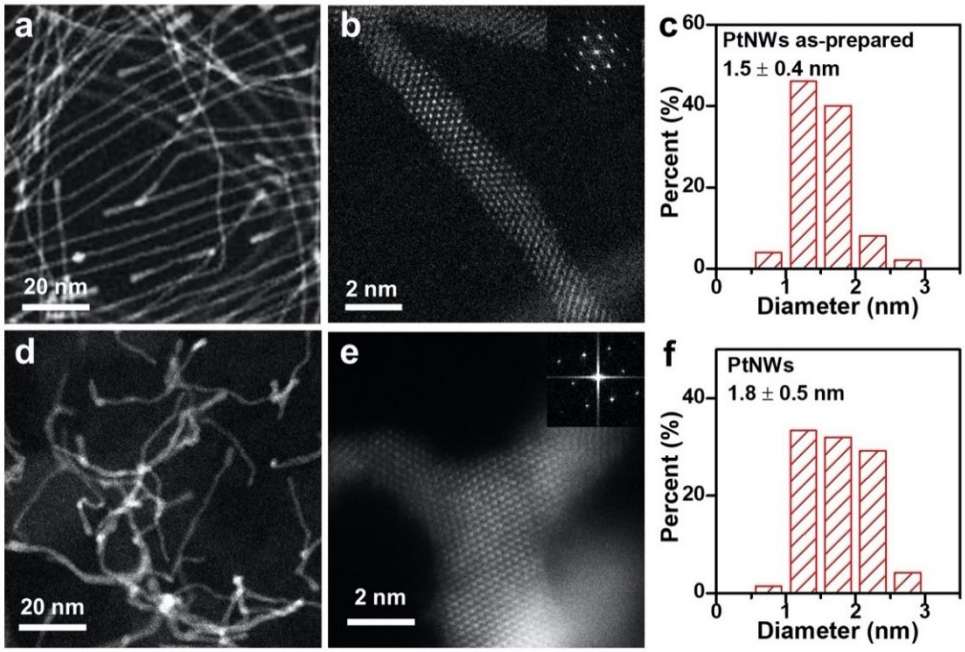


**Figure 3. 4** (**a, b** and **c**) STEM images and size distribution of the as-prepared PtNWs. (**d, e** and **f**) STEM images and size distribution of the PtNWs after annealing and acid wash.

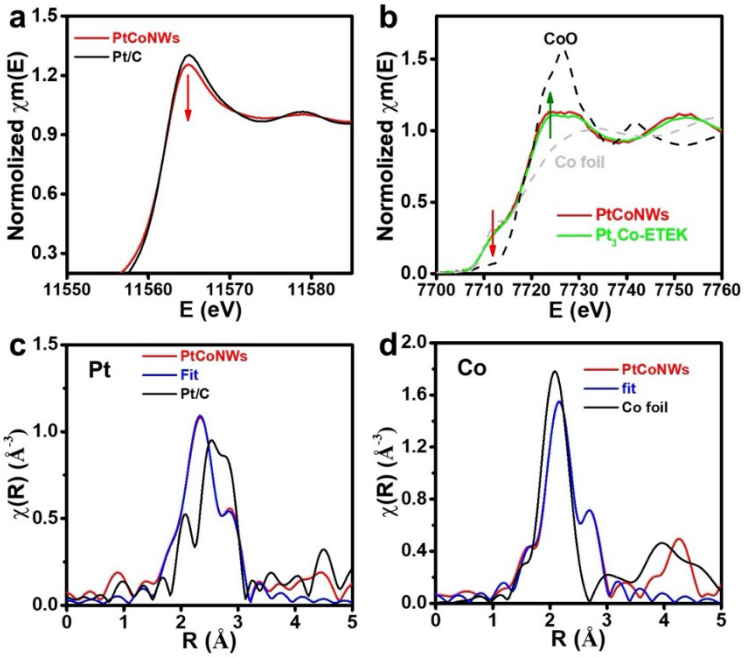


**Figure 3. 5** XAS results of the PtCoNWs in comparison with Pt/C. (**a** and **b**) XANES spectra at the (**a**) Pt $L_3$-edge and (**b**) Co K-edge with Pt/C and $Pt_3Co$-ETEK as references. (**c** and **d**) Fourier-transform EXAFS spectra and the corresponding first shell least-square fit (blue) at the (**c**) Pt $L_3$-edge and (**d**) Co-K edge for the PtCoNWs.

| | Pt-Pt scattering | | | Pt-Co scattering | | |
|---|---|---|---|---|---|---|
| $J_{Pt}$ | $R_{Pt-Pt}$ (Å) | $N_{Pt-Pt}$ | $\sigma^2$ (Å$^2$)×10$^{-3}$ | $R_{Pt-Co}$(Å) | $N_{Pt-Co}$ | $\sigma^2$ (Å$^2$)×10$^{-3}$ |
| 1.3 | 2.724 ± 0.005 | 6.9 ± 0.8 | 5.0 ± 0.9 | 2.65 ± 0.01 | 2.1 ± 0.7 | 10 ± 3 |
| | Co-Co scattering | | | Co-Pt scattering | | |
| $J_{Co}$ | $R_{Co-Co}$ (Å) | $N_{Co-Co}$ | $\sigma^2$ (Å$^2$)×10$^{-3}$ | $R_{Co-Pt}$(Å) | $N_{Co-Pt}$ | $\sigma^2$ (Å$^2$)×10$^{-3}$ |
| 1.0 | 2.60 ± 0.01 | 1.8 ± 0.7 | 3 ± 3 | 2.65 ± 0.01 | 10 ± 1 | 10 ± 3 |

**Table 3. 2** EXAFS fitting results of the PtCoNWs. *Fits were done at the Pt $L_3$-edge and Co K-edge in *R*-space simultaneously, $k^{1,2,3}$ weighting. $1.17 < R < 3.22$ Å and $\Delta k = 2.73 - 11.00$ Å$^{-1}$ were used for fitting of the Pt edge data and $1.17 < R < 3.05$Å and $\Delta k = 2.6 - 10.6$ Å$^{-1}$ were used for fitting of the Co edge data. $S_0^2$ was fixed at 0.83 and 0.80 for Pt and Co, respectively, obtained by fitting the Pt and Co reference foils.

**MEA performance**

We further applied the resulting ultrathin PtCoNWs, PtNWs, and commercial Pt/C (40 wt% Pt, Alfa Aesar) on the cathode of MEAs and compared their performance in a PEMFC single cell with oxygen or air as the cathodic feeding gas. The MEAs were prepared by ultrasonic spraying the catalysts directly on two sides of the proton-exchange membrane. The geometric Pt loading in MEAs was fixed at 0.025 $mg_{Pt}/cm^2$ for anode and about 0.05 $mg_{Pt}/cm^2$ for cathode. The MAs of PtCoNWs, PtNWs, and commercial 40% Pt/C catalysts in MEA were evaluated in the $H_2$-$O_2$ atmosphere at 80 °C, using the hydrogen-crossover corrected current densities at 0.9 $V_{Cell,\ iR\text{-}free}$. In both $H_2$-$O_2$ and $H_2$-Air tests, the PtCoNWs delivered a much higher current density than PtNWs and Pt/C in all potential regions (Figure 3. 6a, b). The PtCoNWs demonstrated an exceptional high MA of $1.06 \pm 0.14$ $A/mg_{Pt}$ at 0.9 V at BOL, which is 2.4 times that of the pure PtNWs (0.44 $A/mg_{Pt}$) and 3.3 times that of the commercial 40% Pt/C catalysts (0.32 $A/mg_{Pt}$) (Figure 3. 6c), far exceeding the 2020 DOE target (0.44 $A/mg_{PGM}$). Impressively, the PtCoNWs exhibited the record-high MA among the state-of-the-art Pt-alloy catalysts in MEAs (Table 3. 3).

Importantly, when incorporated in MEA (ca. 0.025 $mg_{Pt}/cm^2$ for anode and ca. 0.05 $mg_{Pt}/cm^2$ for cathode), the PtCoNWs delivered a large ECSA of 73.2 $m^2/g_{Pt}$, which was much higher than that of PtNWs (47.0 $m^2/g_{Pt}$) and Pt/C (33.0 $m^2/g_{Pt}$) (Figure 3. 7). The PtNWs only demonstrated a modest ECSA despite having a smaller average diameter, suggesting that PtNWs might suffer more coalescence or dissolution during the activation process. Indeed, after the MA measurement, PtCoNWs maintained the 1D morphology with a size distribution of $3.1 \pm 0.9$ nm (Figure 3. 8a). Under the same conditions, however, PtNWs evolved into nanorods and nanoparticles (NPs) with a size distribution of $3.6 \pm 1.1$ nm and $3.91 \pm 0.6$ nm, respectively (Figure 3. 9). Therefore, the large ECSA of PtCoNWs may be

attributed to their 1D structure with a high surface area that was well maintained after the MA measurement. In addition, the inverse FFT analysis of the PtCoNWs after the MEA test further confirmed that the segregated structure of the Pt-rich shell ($Pt_{98}Co_2$) and the alloy core ($Pt_{59}Co_{41}$) was also retained, showing different (111) lattice spacings at the core (0.218 nm) and the shell (0.227 nm) regions (Figure 3. 8e and f). Impressively, the composition changed only slightly from $Pt_{82}Co_{18}$ to $Pt_{86}Co_{14}$ after the MA measurement (Figure 3. 8g). All suggest excellent intrinsic structural and compositional stability of the PtCoNWs in MEA.

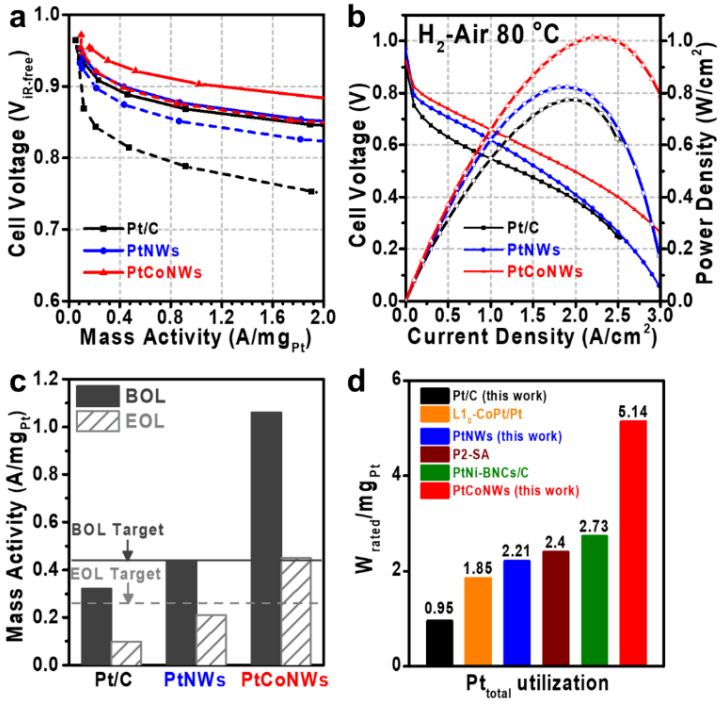


**Figure 3. 6** Comparison of MEA performances of PtCoNWs, PtNWs, Pt/C, and state-of-the-art catalysts. (a) The BOL (solid line) and EOL (dashed line) MA polarization curves of Pt/C, PtNWs and PtCoNWs tested in $H_2$-$O_2$ atmosphere. (b) $H_2$-air I-V polarization (solid marks) and power density (hollow marks) curves of Pt/C, PtNWs, and PtCoNWs. (c) Comparison of MAs at 0.9 $V_{iR\text{-}free}$ for Pt/C, PtNWs and PtCoNWs. DOE 2020 MA target: 0.44 $A/mg_{PGM}$ (BOL) and 60% retention (0.264 $A/mg_{PGM}$) (EOL). (d) Comparison of total Pt utilization of PtCoNWs with the state-of-the-art values reported previously. The total Pt utilization was calculated by normalizing the rated power density over total Pt loading. Reference: $L1_0$-CoPt/Pt: 9 nm $L1_0$-phase intermetallic PtCo nanoparticles.[11] P2-SA: 5 nm PtNi nanoparticles dealloyed 0.5 M sulfuric acid at 80 °C for 24 h in nitrogen.[33] PtNi-BNCs/C: Pt-Ni bunched nanocages.[10]

| Catalyst | Total loading (Anode + Cathode) ($mg_{PGM}/cm^2$) | MA (A/mg) | | AST condition | Power density at 0.6 V ($mW/cm^2$) | Peak power density ($mW/cm^2$) | $H_2$-air test condition |
|---|---|---|---|---|---|---|---|
| | | BOL | EOL | | | | |
| **PtCoNWs (This work)** | **0.072 (0.025 + 0.047)** | **1.06** | **0.45** | Square wave: 0.6 V-0.95 V 30,000 cycles | **840** | **1016** | Nafion HP, 80 °C, 150 kPa, 100% RH |
| **PtNWs (This work)** | **0.077 (0.025 + 0.052)** | **0.44** | **0.21** | | **660** | **830** | |
| **Pt/C (This work)** | **0.075 (0.025 + 0.050)** | **0.32** | **0.098** | | **402** | **773** | |
| PtNi-BNSs/C[10] | 0.25 (0.1 + 0.15) | NA | NA | Air-conditioned at room the temperature of 26 °C for 180 hours | 600 | 770 | Nafion 212, 80 °C, 300 kPa, 100% RH |
| PtNi-BNCs/C[10] | 0.25 (0.1 + 0.15) | NA | NA | | 900 | 920 | |
| $L1_0$-CoPt/Pt[11] | 0.205 (0.1 + 0.105) | 0.56 | 0.45 | Trapezoidal wave: 0.6 V-0.95 V 30,000 cycles | 570 | NA | Nafion 211, 80 °C, 150 kPa, 100% RH |
| PtNi NW array[34] | 0.312* | 0.07 | 0.051 | 0.6-1.2 V (100 mV/s) 3,000 cycles | 541 | NA | Nafion 212, 80 °C, cathode/anode: 230/250 kPa, 30%/50% RH |
| Pt NW array[34] | 0.312* | 0.062 | 0.064 | | 504 | NA | |
| P2-SA[33] | 0.15 (0.05 + 0.1) | 0.64 | 0.5 | Triangle wave: 0.6-1.0 V (50 mV/s) 30,000 cycles | 900 | NA | Nafion 211, 80 °C, 170 kPa, 100% RH |
| P2-NA[33] | 0.15 (0.05 + 0.1) | 0.62 | 0.43 | | 900 | NA | |

**Table 3. 3** Comparisons of the MEA performance among the state-of-the-art catalysts. *: assuming this is the total loading of Pt due to missing specification. NA: not available. Reference: PtNi-BNSs/C: Pt-Ni bunched nanospheres.[10] PtNi-BNCs/C: Pt-Ni bunched nanocages.[10] $L1_0$-CoPt/Pt: 9 nm $L1_0$-phase intermetallic PtCo nanoparticles.[11] PtNi NW array: PtNi nanowire array gas diffusion electrode.[34] Pt NW array: Pt nanowire array gas diffusion electrode.[34] P2-SA: 5 nm PtNi nanoparticles dealloyed 0.5 M sulfuric acid at 80 °C for 24 h in nitrogen.[33] P2-NA: 5 nm PtNi nanoparticles dealloyed 1 M nitric acid at 70 °C for 24 h in nitrogen.[33]

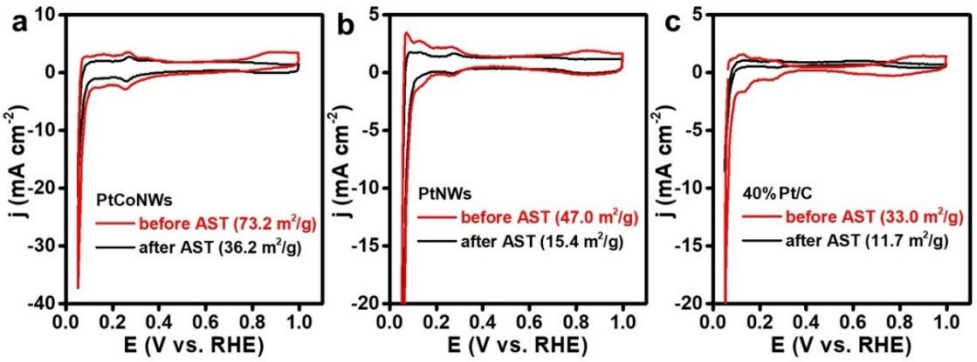


**Figure 3. 7** ECSAs of the PtCoNWs in comparison with Pt/C and PtNWs before and after AST. All ECSAs were measured on MEA.

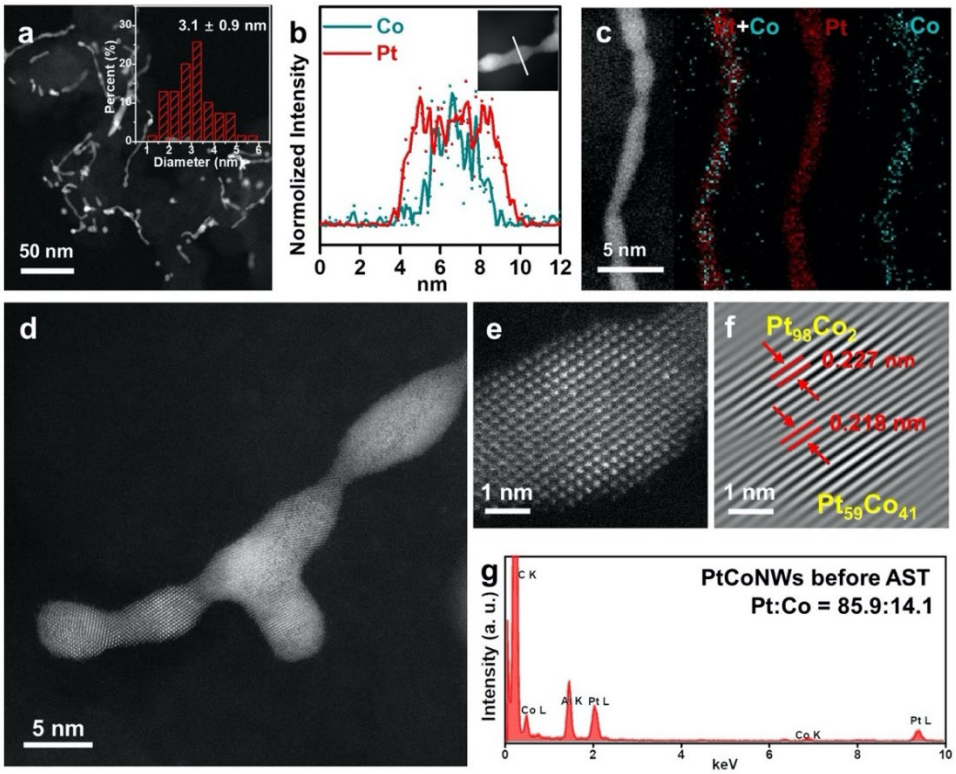


**Figure 3. 8** Characterizations of the PtCoNWs after activation process and MA measurement, which represents the state before AST. (**a**) STEM low magnification image, inset is the size distribution analysis. (**b**) EDX line-scan profiles. (**c**) EDX mapping results. (**d** and **e**) High resolution STEM images. (**f**) Inverse FFT of the STEM in panel (**e**). (**g**) Representative EDX spectrum result.

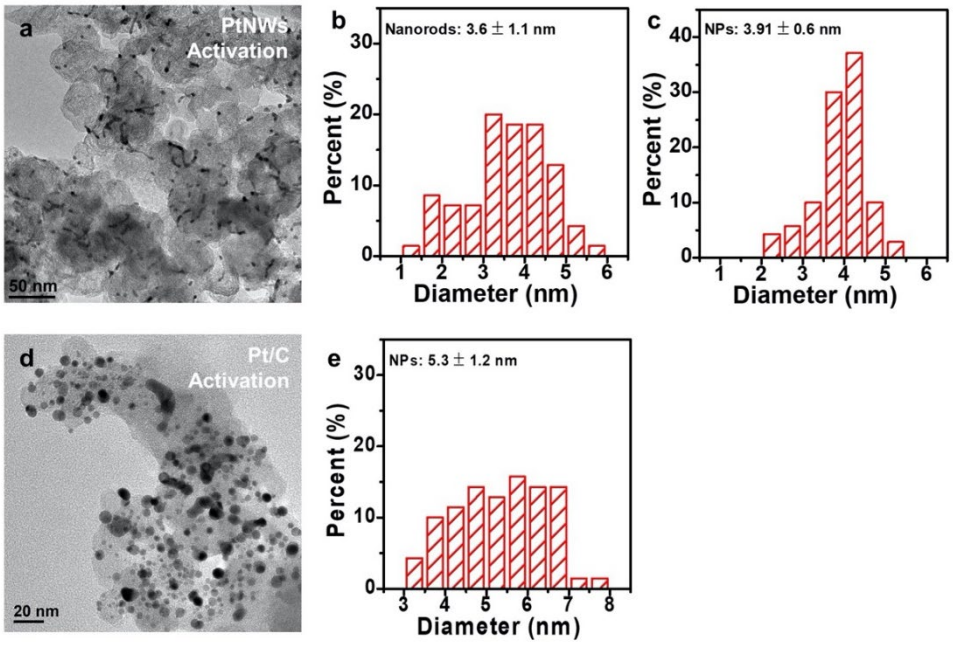


**Figure 3. 9** (**a** to **c**) TEM image and size distribution of nanorods and nanoparticles (NPs) from PtNWs after activation process and MA measurement. (**d** to **e**) TEM image and size distribution of Pt/C after activation process and MA measurement, suggesting the growth of Pt NPs after activation and MA measurement.

The outstanding MA and large ECSA enabled the PtCoNWs to exhibit high power density in $H_2$-air tests (Figure 3. 6b). The PtCoNWs and PtNWs showed higher current density than that of Pt/C at all potential regions. The PtCoNWs delivered a current density of 1.4 A/cm$^2$ at 0.6 V cell voltage[10, 35] and reached a peak power density of 1016 mW/cm$^2$, outperforming the PtNWs (1.1 A/cm$^2$ at 0.6 V and 830 mW/cm$^2$) and Pt/C (0.67 A/cm$^2$ at 0.6 V and 773 mW/cm$^2$). At an even higher current density of 2.5 A/cm$^2$, PtCoNWs still delivered a power density of 1000 mW/cm$^2$, while PtNWs only showed a power density of 666 mW/cm$^2$, comparable to that of Pt/C (626 mW/cm$^2$). The above power density performance analysis suggested that 1D PtCoNWs showed lower $O_2$ transport resistance than the nanoparticle Pt/C. We also evaluated the rated power, at which the heat rejection balance ($Q/\Delta T_i$ <1.45) should be considered for practical operation yet rarely reported and

overlooked. The rated power was determined at 0.76 V for cells operated at 80 °C. The PtCoNWs delivered a rated power of 0.37 W/cm$^2$, which is 5.2 times that of Pt/C (0.071 W/cm$^2$) and 2.2 times that of the PtNWs (0.17 W/cm$^2$). This corresponds to an ultrahigh total effective Pt utilization of 5.14 $W_{rated}/mg_{Pt}$ for PtCoNWs, which is 5.4 times that of Pt/C (0.95 $W_{rated}/mg_{Pt}$), surpassing all the state-of-the-art Pt-alloy catalysts in MEA (Figure 3. 6d). The high Pt utilization demonstrated the efficiency of 1D PtCoNW structures in MEA, which can significantly reduce the usage of Pt while delivering high performance in PEMFCs.

We followed the DOE suggested protocol[7] to evaluate the durability of the catalysts by applying the square wave potential cycling between 0.60 and 0.95 V for 30,000 cycles. The PtCoNWs showed an impressive EOL MA of 0.45 $A/mg_{Pt}$, which is still above the BOL MA target of DOE (0.44 $A/mg_{PGM}$) (Figure 3. 6c). On the other hand, the after AST MA of PtNWs and Pt/C decayed to 0.21 $A/mg_{Pt}$ and 0.1 $A/mg_{Pt}$, respectively, both below the DOE end of life (EOL) target of 0.26 $A/mg_{PGM}$ (Figure 3. 6c). To investigate the degradation behavior, we also performed the characterizations on the catalysts after AST in MEA. Severe aggregation and shape deformation was observed in all catalyst groups. We observed that considerable PtCoNWs maintained the 1D structure, while some tended to evolve into nanoparticles (Figure 3. 10b, c), which might contribute to the performance loss. Impressively after AST, the Pt-skin on PtCoNWs still remained as suggested by the inverse FFT and EDX line scan results (Figure 3. 11c, g). The mean diameter of PtCoNWs increased from 3.1 ± 0.9 nm to 6.6 ± 1.9 nm (Figure 3. 10a, b), leading to a decreased ECSA of 36.2 $m^2/g_{Pt}$ (Figure 3. 7), which, however, was still larger than the initial ECSA of Pt/C (33.0 $m^2/g_{Pt}$). For the PtNWs, a more pronounced morphology change was observed after

AST, where nearly all PtNWs evolved into spherical NPs (4.6 ± 1.2 nm) and showed a low ECSA of 15.4 $m^2/g_{Pt}$ (Figures 3. 7, Figure 3. 12a, c). Likewise, the Pt/C suffered significant aggregation after AST with average size increasing from 5.3 ± 1.2 nm to 8.8 ± 6.4 nm, and the ECSA dropped from 33.0 $m^2/g_{Pt}$ to 11.7 $m^2/g_{Pt}$ (Figures 3. 7, Figure 3. 12b and d). In addition to aggregation, the activity loss could also be partly attributed to the nonoptimal attachment between the catalysts and the carbon support. After AST, the density of nanocatalysts on carbon support decreased (Figures 4.12c), indicating detachment and the loss of catalyst. This problem is commonly reported in the degradation mechanism of fuel cell catalysts.[36-38]

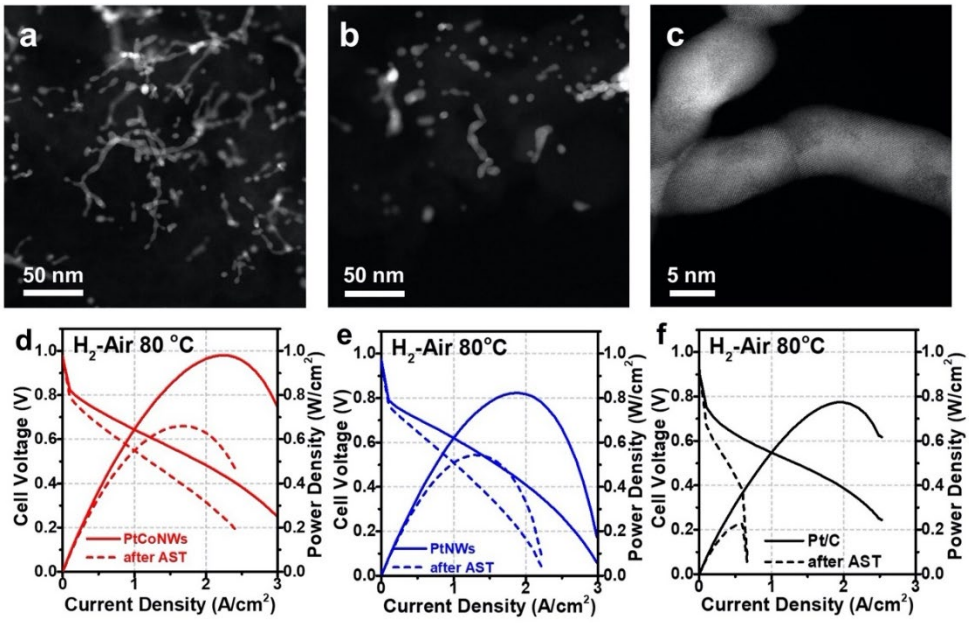


**Figure 3. 10** Durability analysis of catalysts. (a and b) HAADF-TEM images of PtCoNWs (a) at BOL and (b) at EOL. (c) High-resolution STEM image of PtCoNWs after AST. (d to f) Comparison of $H_2$-air performance of (d) PtCoNWs, (e) PtNWs, and (f) Pt/C catalysts at the BOL (solid line) and EOL (dashed line) stage.

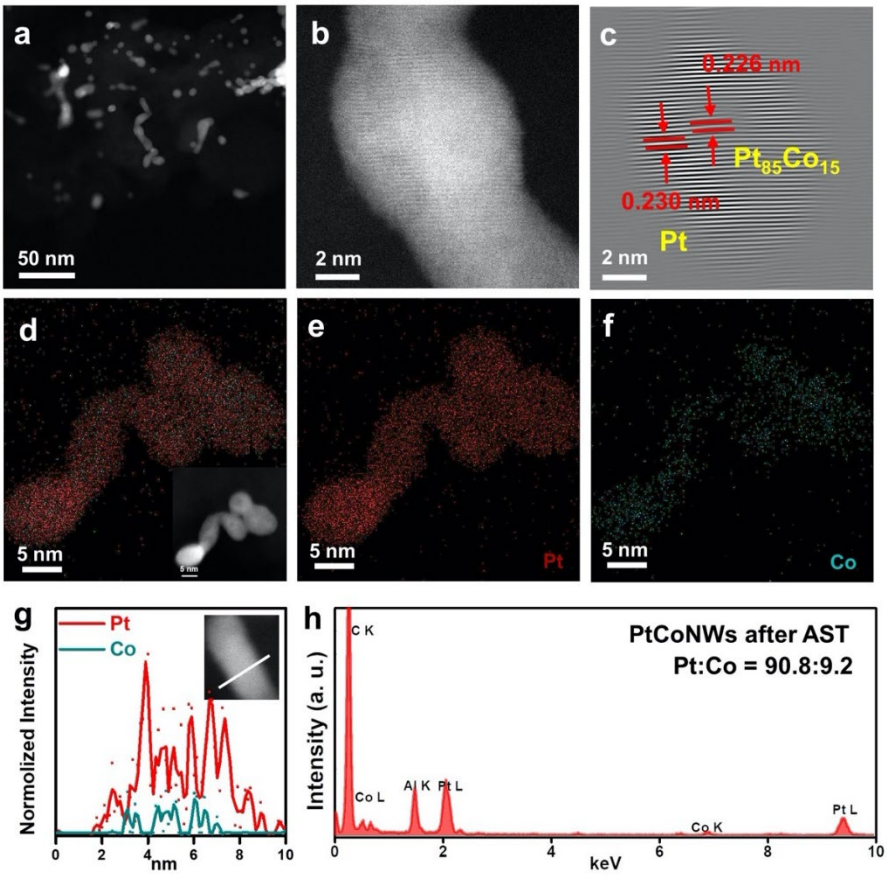


**Figure 3. 11** Characterizations of the PtCoNWs after the AST. (**a**) STEM low magnification image. (**b**) High resolution STEM image. (**c**) Inverse FFT of the STEM in panel (**b**). (**d, e** and **f**) EDX mapping results. (**g**) EDX line-scan profiles. (**h**) Representative EDX spectrum result.

Overall, both PtCoNWs and PtNWs demonstrated better structural stability than Pt/C. And the PtCoNWs demonstrated much better structural stability compared to Pt/C, which may be attributed to their uniform alloying Pt-Co core. In addition, EDX analysis revealed that PtCoNWs retained most of the Co after AST, where the composition of Co only slightly changed from 14% to 9% (Figures 3.11h), indicating composition stability. After AST, the PtCoNWs still delivered a peak power density of 662 $mW/cm^2$ (Figures 3.10d), while the peak power of PtNWs and Pt/C decayed to 546 $mW/cm^2$ and 220 $mW/cm^2$, respectively (Figures 3.10e, f). 1D NW structures demonstrated much better performance

in both MA and power performance compared to nanoparticles (Pt/C), while PtCo alloy demonstrated superiority over pure Pt, confirming the advantages and better structural durability of 1D Pt-alloy catalysts in PEMFC applications. Through the comparison of the structures and compositions of all catalyst groups, it becomes more evident that 1D morphology showed better structural stability than the nanoparticle Pt/C, and that PtCo alloy core further contributed to the higher stability of PtCoNWs, which resulted in the decent activity and power density after AST and can potentially overcome the dilemma between low loading and high-power density.

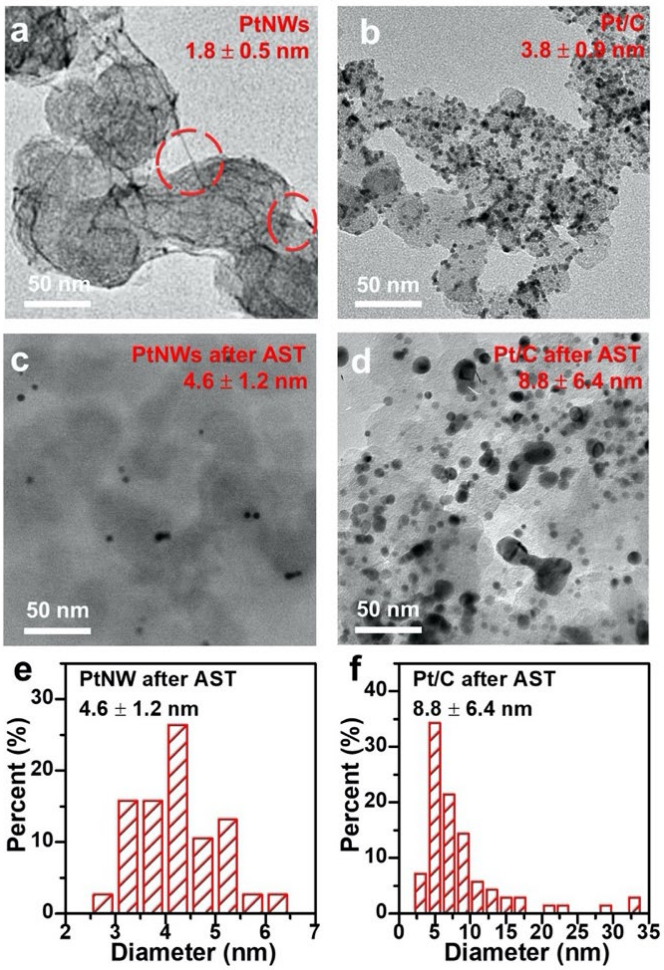


**Figure 3. 12** MEA stability analysis of the PtNWs and Pt/C. (a,b) Low magnification TEM image of PtNWs (a) and Pt/C (b) before MEA measurements. (c,d) Low magnification TEM image of

PtNWs (c) and Pt/C (d) after AST. (e,f) Size distribution analysis of PtNWs (e) and Pt/C (f) after AST.

### 3.4 Conclusion

In summary, we demonstrated an ultralow Pt loading and high-performance MEA using ultrathin PtCoNWs. The PtCoNWs showed a high BOL ECSA of 73.2 $m^2/g_{Pt}$, a record-high MA of 1.06 $A/mg_{Pt}$, and excellent structural and composition stability in a MEA, outperforming most state-of-the-art Pt-alloy catalysts in MEA reported to date (Table 1) and surpassing DOE set 2020 targets. PtCoNWs also delivered an impressively high Pt utilization of 5.14 $W_{rated}/mg_{Pt}$ at 80 °C, with ultralow Pt loading of 0.047 $mg_{Pt}/cm^2$, suggesting a valid pathway to overcome the dilemma between low loading and high-power density using ultrathin 1D catalysts.

### 3.5 References


1. Debe, M. K., Electrocatalyst approaches and challenges for automotive fuel cells. *Nature* **2012,** *486* (7401), 43-51.

2. Wang, X. X.; Swihart, M. T.; Wu, G., Achievements, Challenges and Perspectives on Cathode Catalysts in Proton Exchange Membrane Fuel Cells for Transportation. *Nat. Catal.* **2019,** *2* (7), 578-589.

3. Kodama, K.; Nagai, T.; Kuwaki, A.; Jinnouchi, R.; Morimoto, Y., Challenges in applying highly active Pt-based nanostructured catalysts for oxygen reduction reactions to fuel cell vehicles. *Nature Nanotechnology* **2021,** *16* (2), 140-147.

4. Wu, J. B.; Yang, H., Platinum-based oxygen reduction electrocatalysts. *Acc. Chem. Res.* **2013,** *46* (8), 1848-1857.

5. Whiston, M. M.; Azevedo, I. L.; Litster, S.; Whitefoot, K. S.; Samaras, C.; Whitacre, J. F., Expert Assessments of the Cost and Expected Future Performance of Proton Exchange Membrane Fuel Cells for Vehicles. *Proc. Natl. Acad. Sci. U. S. A.* **2019,** *116* (11), 4899-4904.

6. Kongkanand, A.; Mathias, M. F., The priority and challenge of high-power performance of low-platinum proton-exchange membrane fuel cells. *J. Phys. Chem. Lett.* **2016,** *7* (7), 1127-1137.

7. DRIVE, U. S. Fuel Cell Technical Team Roadmap. https://www.energy.gov/sites/prod/files/2017/11/f46/FCTT_Roadmap_Nov_2017_FINAL.pdf (accessed November).

8. Kriston, A.; Xie, T. Y.; Gamliel, D.; Ganesan, P.; Popov, B. N., Effect of Ultra-Low Pt Loading on Mass Activity of Polymer Electrolyte Membrane Fuel Cells. *J. Power Sources* **2013,** *243*, 958-963.

9. Fan, J.; Chen, M.; Zhao, Z.; Zhang, Z.; Ye, S.; Xu, S.; Wang, H.; Li, H., Bridging the gap between highly active oxygen reduction reaction catalysts and effective catalyst layers for proton exchange membrane fuel cells. *Nat. Energy* **2021,** *6* (5), 475-486.

10. Tian, X. L.; Zhao, X.; Su, Y. Q.; Wang, L. J.; Wang, H. M.; Dang, D.; Chi, B.; Liu, H. F.; Hensen, E. J. M.; Lou, X. W.; Xia, B. Y., Engineering Bunched Pt-Ni Alloy Nanocages for Efficient Oxygen Reduction in Practical Fuel Cells. *Science* **2019,** *366* (6467), 850-856.

11. Li, J. R.; Sharma, S.; Liu, X. M.; Pan, Y. T.; Spendelow, J. S.; Chi, M. F.; Jia, Y. K.; Zhang, P.; Cullen, D. A.; Xi, Z.; Lin, H. H.; Yin, Z. Y.; Shen, B.; Muzzio, M.; Yu, C.; Kim, Y. S.; Peterson, A. A.; More, K. L.; Zhu, H. Y.; Sun, S. H., Hard-Magnet $L1_0$-CoPt Nanoparticles Advance Fuel Cell Catalysis. *Joule* **2019,** *3* (1), 124-135.

12. Liu, Z. Y.; Zhao, Z. P.; Peng, B. S.; Duan, X. F.; Huang, Y., Beyond Extended Surfaces: Understanding the Oxygen Reduction Reaction on Nanocatalysts. *J. Am. Chem. Soc.* **2020,** *142* (42), 17812-17827.

13. Li, M. F.; Zhao, Z. P.; Cheng, T.; Fortunelli, A.; Chen, C. Y.; Yu, R.; Zhang, Q. H.; Gu, L.; Merinov, B. V.; Lin, Z. Y.; Zhu, E. B.; Yu, T.; Jia, Q. Y.; Guo, J. H.; Zhang, L.; Goddard, W. A.; Huang, Y.; Duan, X. F., Ultrafine jagged platinum nanowires enable ultrahigh mass activity for the oxygen reduction reaction. *Science* **2016,** *354* (6318), 1414-1419.

14. Sandbeck, D. J. S.; Secher, N. M.; Inaba, M.; Quinson, J.; Sorensen, J. E.; Kibsgaard, J.; Zana, A.; Bizzotto, F.; Speck, F. D.; Paul, M. T. Y.; Dworzak, A.; Dosche, C.; Oezaslan, M.; Chorkendorff, I.; Arenz, M.; Cherevko, S., The Dissolution Dilemma for Low Pt Loading Polymer Electrolyte Membrane Fuel Cell Catalysts. *J. Electrochem. Soc.* **2020,** *167* (16).

15. Lu, Y. X.; Du, S. F.; Steinberger-Wilckens, R., One-Dimensional Nanostructured Electrocatalysts for Polymer Electrolyte Membrane Fuel Cells-A Review. *Appl Catal B-Environ* **2016,** *199*, 292-314.

16. Chen, Y.; Cheng, T.; Goddard III, W. A., Atomistic Explanation of the Dramatically Improved Oxygen Reduction Reaction of Jagged Platinum Nanowires, 50 Times Better than Pt. *J. Am. Chem. Soc.* **2020,** *142* (19), 8625-8632.

17. Fuchs, T.; Drnec, J.; Calle-Vallejo, F.; Stubb, N.; Sandbeck, D. J. S.; Ruge, M.; Cherevko, S.; Harrington, D. A.; Magnussen, O. M., Structure dependency of the atomic-scale mechanisms of platinum electro-oxidation and dissolution. *Nat. Catal.* **2020,** *3* (9), 754-761.

18. Bu, L. Z.; Guo, S. J.; Zhang, X.; Shen, X.; Su, D.; Lu, G.; Zhu, X.; Yao, J. L.; Guo, J.; Huang, X. Q., Surface Engineering of Hierarchical Platinum-Cobalt Nanowires for Efficient Electrocatalysis. *Nat. Commun.* **2016,** *7*.

19. Jiang, K. Z.; Zhao, D. D.; Guo, S. J.; Zhang, X.; Zhu, X.; Guo, J.; Lu, G.; Huang, X. Q., Efficient Oxygen Reduction Catalysis by Subnanometer Pt Alloy Nanowires. *Sci. Adv.* **2017,** *3* (2), 1-8.

20. Stephens, I. E. L.; Rossmeisl, J.; Chorkendorff, I., Toward sustainable fuel cells. *Science* **2016,** *354* (6318), 1378.

21. Sievers, G. W.; Jensen, A. W.; Quinson, J.; Zana, A.; Bizzotto, F.; Oezaslan, M.; Dworzak, A.; Kirkensgaard, J. J. K.; Smitshuysen, T. E. L.; Kadkhodazadeh, S.; Juelsholt, M.; Jensen, K. M. O.; Anklam, K.; Wan, H.; Schafer, J.; Cepe, K.; Escudero-Escribano, M.; Rossmeisl, J.; Quade, A.; Bruser, V.; Arenz, M., Self-Supported Pt-CoO Networks Combining High Specific Activity with High Surface Area for Oxygen Reduction. *Nat. Mater.* **2020**.

22. Arruda, T. M.; Shyam, B.; Ziegelbauer, J. M.; Mukerjee, S.; Ramaker, D. E., Investigation into the competitive and site-specific nature of anion adsorption on Pt using in situ X-ray absorption spectroscopy. *J. Phys. Chem. C* **2008,** *112* (46), 18087-18097.

23. Jia, Q.; Liang, W.; Bates, M. K.; Mani, P.; Lee, W.; Mukerjee, S., Activity Descriptor Identification for Oxygen Reduction on Platinum-Based Bimetallic Nanoparticles: In Situ Observation of the Linear Composition–Strain–Activity Relationship. *ACS Nano* **2015,** *9* (1), 387-400.

24. Newville, M., IFEFFIT: interactive XAFS analysis and FEFF fitting. *J Synchrotron Radiat* **2001,** *8* (Pt 2), 322-4.

25. Ravel, B.; Newville, M., ATHENA, ARTEMIS, HEPHAESTUS: data analysis for X-ray absorption spectroscopy using IFEFFIT. *J. Synchrotron Radiat.* **2005,** *12* (Pt 4), 537-41.

26. Newville, M.; Līviņš, P.; Yacoby, Y.; Rehr, J. J.; Stern, E. A., Near-edge x-ray-absorption fine structure of Pb: A comparison of theory and experiment. *Phys. Rev. B* **1993,** *47* (21), 14126-14131.

27. Ankudinov, A. L.; Ravel, B.; Rehr, J. J.; Conradson, S. D., Real-space multiple-scattering calculation and interpretation of x-ray-absorption near-edge structure. *Phys. Rev. B* **1998,** *58* (12), 7565-7576.

28. Hlil, E. K.; BaudoingSavois, R.; Moraweck, B.; Renouprez, A. J., X-ray absorption edges in platinum-based alloys. 2. influence of ordering and of the nature of the second metal. *J. Phys. Chem.* **1996,** *100* (8), 3102-3107.

29. Jia, Q. Y.; Caldwell, K.; Ramaker, D. E.; Ziegelbauer, J. M.; Liu, Z. Y.; Yu, Z. Q.; Trahan, M.; Mukerjee, S., *In Situ* Spectroscopic Evidence for Ordered Core–Ultrathin Shell $Pt_1Co_1$

Nanoparticles with Enhanced Activity and Stability as Oxygen Reduction Electrocatalysts. *J. Phys. Chem. C* **2014,** *118* (35), 20496-20503.

30. Hwang, B. J.; Sarma, L. S.; Chen, J. M.; Chen, C. H.; Shih, S. C.; Wang, G. R.; Liu, D. G.; Lee, J. F.; Tang, M. T., Structural Models and Atomic Distribution of Bimetallic Nanoparticles as Investigated by X-ray Absorption Spectroscopy. *J. Am. Chem. Soc.* **2005,** *127* (31), 11140-11145.

31. Kim, H. Y.; Kim, J. M.; Ha, Y.; Woo, J.; Byun, A.; Shin, T. J.; Park, K. H.; Jeong, H. Y.; Kim, H.; Kim, J. Y.; Joo, S. H., Activity Origin and Multifunctionality of Pt-Based Intermetallic Nanostructures for Efficient Electrocatalysis. *ACS Catal.* **2019,** *9* (12), 11242-11254.

32. Wang, Z. X.; Yao, X. Z.; Kang, Y. Q.; Miao, L. Q.; Xia, D. S.; Gan, L., Structurally Ordered Low-Pt Intermetallic Electrocatalysts toward Durably High Oxygen Reduction Reaction Activity. *Adv. Funct. Mater.* **2019,** *29* (35).

33. Han, B. H.; Carlton, C. E.; Kongkanand, A.; Kukreja, R. S.; Theobald, B. R.; Gan, L.; O'Malley, R.; Strasser, P.; Wagner, F. T.; Shao-Horn, Y., Record Activity and Stability of Dealloyed Bimetallic Catalysts for Proton Exchange Membrane Fuel Cells. *Energy Environ. Sci.* **2015,** *8* (1), 258-266.

34. Mardle, P.; Thirunavukkarasu, G.; Guan, S. L.; Chiu, Y. L.; Du, S. F., Comparative Study of PtNi Nanowire Array Electrodes toward Oxygen Reduction Reaction by Half-Cell Measurement and PEMFC Test. *ACS Appl. Mater. Interfaces* **2020,** *12* (38), 42832-42841.

35. Chong, L.; Wen, J.; Kubal, J.; Sen, F. G.; Zou, J.; Greeley, J.; Chan, M.; Barkholtz, H.; Ding, W.; Liu, D.-J., Ultralow-loading platinum-cobalt fuel cell catalysts derived from imidazolate frameworks. *Science* **2018,** *362* (6420), 1276.

36. Shao, Y. Y.; Yin, G. P.; Gao, Y. Z., Understanding and Approaches for the Durability Issues of Pt-Based Catalysts for PEM Fuel Cell. *J. Power Sources* **2007,** *171* (2), 558-566.

37. Beermann, V.; Holtz, M. E.; Padgett, E.; de Araujo, J. F.; Muller, D. A.; Strasser, P., Real-Time Imaging of Activation and Degradation of Carbon Supported Octahedral Pt-Ni Alloy Fuel Cell Catalysts at the Nanoscale Using *In situ* Electrochemical Liquid Cell STEM. *Energy Environ. Sci.* **2019,** *12* (8), 2476-2485.

38. Takao, S.; Sekizawa, O.; Samjeske, G.; Kaneko, T.; Higashi, K.; Yoshida, Y.; Zhao, X.; Sakata, T.; Yamamoto, T.; Gunji, T.; Uruga, T.; Iwasawa, Y., Observation of Degradation of Pt and Carbon Support in Polymer Electrolyte Fuel Cell Using Combined Nano-X-ray Absorption Fine Structure and Transmission Electron Microscopy Techniques. *ACS Appl. Mater. Interfaces* **2018,** *10* (33), 27734-27744.

# Chapter 4. Ultrafine Pt nanoparticles with endohedral oxide clusters for durable fuel cells

## 4.1 Introduction

Proton-exchange-membrane fuel cells (PEMFCs) that directly convert the chemical energy in hydrogen to electricity represent an attractive zero-emission power generation technology [1-3]. The implementation of PEMFCs requires costly platinum group metal (PGM) catalysts to facilitate the sluggish cathodic oxygen reduction reaction (ORR), which accounts for up to 50% of the total system cost and represents a critical sustainability roadblock preventing widespread adoption of PEMFCs [2-3]. To ensure the competitiveness of PEMFCs in the transportation sector, the US Department of Energy (DOE) has set a series of technical targets for PEMFC catalysts [4]. Generally, fuel cell performance should be evaluated at both low current density (LCD) and high current density (HCD) regimes for different operation scenarios. The kinetic-dominated LCD region strongly affects the fuel efficiency in vehicle applications, since the cells predominantly (90% of the time) operate in a low-power mode during cruising [5], while the performance in HCD regime determines the maximum power output available for the start-up or aggressive acceleration [3], and generally dictates performance retention and the PEMFC lifetime. Performance retention is especially critical in the emerging heavy-duty vehicle applications, which requires traveling six times further than typical light-duty applications and thus demands a much longer lifetime [2, 6].

However, the key performance metrics of PEMFEC catalysts (e.g., activity vs. lifetime durability) often display an intrinsic trade-off relationship and is difficult to achieve simultaneously. These challenges have motivated immense efforts to improve the catalyst activity and durability [7-16]. In particular, various nanostructured (nanowires, nanoframes, nanocages, core-shell, etc.) Pt-based alloy (Pt-M, M = Co, Ni, etc.) catalysts with tailored strain and ligand effects

have been explored to modulate the oxygen binding energy and the ORR catalytic activity [17-18]. However, the application of these elaborate designs in practical fuel cells is commonly challenged by their limited stability and/or difficulties in mass production [3]. For example, the Ostwald ripening of typical nanostructured catalysts could lead to rapid loss of electrochemical surface area (ECSA) and overall mass activity (MA). The Pt-M alloy catalysts often suffer from additional durability penalties associated with the dissolution of non-precious metal cations [2-3, 19], which could occupy the proton sites in the ionomers and lead to cation poisoning effects [20-22] that substantially impede mass transport and compromise the fuel cell performance. To this end, it has been shown that structurally ordered intermetallic Pt-M alloys could improve stability and deliver satisfactory MA retention (> 60%) in LCD region. However, the metal leaching and the associated cation poisoning effects remain a persistent challenge [2, 22], particularly in the HCD region where mass transport could dominate the device performance, as highlighted by an unsatisfactory rated power loss (>10%) [13, 23-28].

Considerable efforts have been made to mitigate metal leaching and cation poisoning effects in Pt-M alloy catalysts [3, 29-32]. For example, it has been shown that oxide-supported Pt catalysts can exhibit improved activity and stability due to the strong metal-oxide interaction [31, 33-34]. Although the role of the oxide support in modifying the electronic structure and stabilizing the Pt has been well corroborated [33, 35], the typically poor conductivity and limited stability of the oxide support itself under acidic conditions prevent its practical implementation in PEMFCs [36]. Inspired by these pioneering studies, herein we report a unique design of ultrafine Pt nanocatalysts with embedded atomically dispersed Co oxide clusters to form a $CoO_x$@Pt core-shell nanostructure as a highly durable ORR electrocatalyst in PEMFCs (Figure 4. 1). This endohedral-oxide design takes full advantage of the strong Pt-oxide interaction to modify the electronic

structure of Pt, thus simultaneously (i) suppressing the Pt atom dissolution, and (ii) enhancing the catalytic activity. Meanwhile, with the unstable and less conductive oxide species fully enclosed by the metallic Pt shells, this design also effectively (i) mitigates the $CoO_x$ dissolution and the consequent cation poisoning effect, and (ii) bypasses the charge transport limitations of typical oxide support (Figure 4. 1).

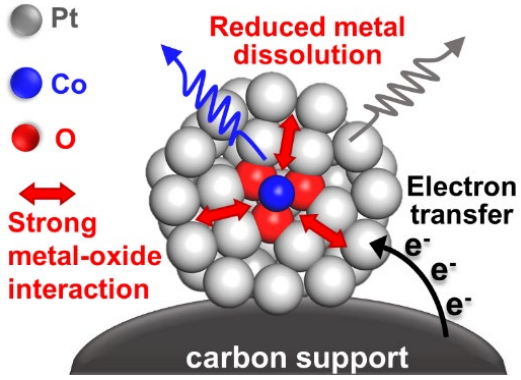


**Figure 4. 1** Schematic illustration of the design and advantages of the ultrafine $CoO_x$@Pt core-shell nanocatalysts supported on carbon.

These combined merits deliver superior PEMFC performance and durability. With the embedded $CoO_x$ retarding Pt leaching and Oswald ripening, the resulting $CoO_x$@Pt exhibits extraordinary stability at an ultrafine size (≈1.5 nm) and displays a compressive surface strain to enable superior performance compared to commercial Pt or PtCo alloy catalysts. The membrane electrode assembly (MEA) made with the $CoO_x$@Pt nanocatalyst demonstrates an outstanding initial MA of 1.10 $A/mg_{PGM}$ and a high rated power density of 1.04 $W/cm^2$ (10.4 $W/mg_{PGM}$) at only 0.10 $mg/cm^2$ total PGM loading. With minimized metal dissolution, the developed MEAs deliver the best durability reported to date: achieving an MA retention of 88.2%, a voltage loss of only 13.3 mV at 0.8 $A/cm^2$, and an exceptionally small rated-power loss of 7.5% after the accelerated degradation test (ADT), greatly exceeding the relevant DOE technical targets [4]. The

exceptional durability makes the $CoO_x$@Pt nanocatalyst a highly promising material especially for heavy-duty fuel cell applications, where the catalyst durability represents a most critical roadblock.

## 4.2 Methods

### Materials and chemicals

Platinum(II) acetylacetonate [$Pt(acac)_2$], aquivion D83-06A ionomer dispersion were purchased from Sigma Aldrich. Cobalt(II) acetylacetonate [$Co(acac)_2$], 10% Pt/C (weight ratio of Pt: 10%), Pt/C (weight ratio of Pt: 40%) were purchased from Alfa Aesar. Commercial PtCo/C (c-PtCo/C) catalyst was purchased from Premetek. Acetone and isopropanol (IPA) were purchased from Fisher Scientific. Freudenberg H14C7 gas diffusion layer (GDL) and polytetrafluoroethylene (PTFE) gasket were purchased from Fuel Cell Store. Carbon support (Ketjenblack EC-300J) was purchased from Fitz Chem LLC. The water was Ultrapure Millipore (18.2 MΩ·cm)

### Synthesis of $CoO_x$@Pt/C

The carbon support (Ketjenblack EC-300J) was activated in hydrogen ($H_2$)/argon (Ar) mixture before use as noted in the literature[1]. A typical synthesis includes 150-180 mg carbon support, 150-170 mg $Pt(acac)_2$, 150-160 mg $Co(acac)_2$, and 15ml acetone mixed under ultrasonication for 20 minutes. After acetone evaporation, the resultant metal precursor adsorbed carbon support was collected and then annealed in a quartz tube in Ar gas tube, whereby the temperature is heated from room temperature (20 °C) to 250 °C and maintained at 250 °C for 8 hours. The sample was collected after it was cooled to room temperature. Then the obtained powder was washed in $N_2$-saturated 0.05M $H_2SO_4$ solution at 80 ºC for 12-16 h. After acid washing, the catalyst was rinsed with ultrapure water till the pH was neutral and collected *via* centrifugation. After thoroughly drying in a vacuum, the obtained catalyst was further annealed in $H_2$/Ar mixture at 180 °C for 1.5

h. After cooling to room temperature, the sample collected was the $CoO_x$@Pt/C catalyst, which was ready for the test.

**Structure and composition characterization**

Transmission electron microscopy (TEM) images were taken with a JEOL JEM 2800 transmission electron microscope operated at 200 kV. Atomic resolution high-angle annular dark-field (HAADF) images, as well as energy-dispersive spectroscopy (EDS) maps, were taken using a JEOL Grand ARM300CF scanning/transmission electron microscopy (S/TEM) operated at 300 kV. The TEM/STEM sample grids were prepared by dispersing the sample in a mixture of water and ethanol, then drop casting the dispersion onto lacey carbon film-coated copper grids (for high-resolution STEM and EDS analysis) using a pipette and drying under ambient conditions. The concentration of catalysts was determined by inductively coupled plasma atomic emission spectroscopy (ICP-AES, Shimadzu ICPE-9000) as well as by EDS coupled in JEOL Grand ARM300CF. X-ray powder diffraction (XRD) patterns were collected with a Panalytical X'Pert Pro X-ray powder diffractometer with Cu-Kα radiation. X-ray photoelectron spectroscopy (XPS) tests were done with Kratos AXIS Ultra DLD spectrometer. XPS depth profiling was conducted using the instrument's $Ar^+$ ion source operated at 4kV, 50uA, and rastered over a 3×3 mm area for 4 minutes. The atomic composition was determined based on photoelectron peak areas and the relative sensitivity factors provided in CasaXPS.

**X-ray absorption spectroscopy (XAS) data collection and analysis**

The electrode inks for the XAS electrodes were composed of 60% ethanol, 40% water, 5 wt % Nafion solution, and the catalyst powder. The ink was spray-coated onto a carbon paper with a total catalyst loading of about 12.5 mg/cm$^2$ (with Co loading of 0.05 mg/cm$^2$ and Pt loading of 2.7 mg/cm$^2$). The XAS experiments were conducted at room temperature in an *in-situ* spectro-

electrochemical half-cell circulated with a continuously $O_2$ purged 0.1 M $HClO_4$ aqueous solution[2], at the beamline ISS 6-BM and 8-ID in National Synchrotron Light Source II (NSLS-II) (Brookhaven National Laboratory, NY). Before being transferred into the cell, the electrodes were conditioned in 0.1 M $HClO_4$ under vacuum for 40 minutes without applying the potential to remove surface contaminants. Potentiostatic control was maintained with an Autolab PGSTAT30 potentiostat (Metrohm USA, formerly Brinkman Instruments). Data were collected on the same electrode in transmission mode at the Pt $L_3$-edge, and fluorescence mode at the Co K-edge, with a Pt/Co reference foil positioned between I2 and I3 as a reference. The voltage cycling limits were 0.05 to 1.00 V vs. RHE. Data collection was performed at the chosen potentials held during anodic sweeps. The electrode was fully cycled following each potential hold to clean the electrode surface after each potential hold. Typical experimental procedures were utilized with details provided in the previous work[3]. The data were processed and fitted using the Ifeffit−based Athena[4] and Artemis[5] programs. Scans were calibrated, aligned, and normalized with background removed using the IFEFFIT suite[6]. The $\chi(R)$ were modeled using single scattering paths calculated by FEFF6[7].

**Membrane Electrode Assemblies (MEA) Fabrication**

The MEA fabrication followed the protocol in the previous work of our group[8]. The catalyst ink was made by mixing the catalysts with the ionomer solution (Aquivion D83-06A) and water-IPA solvent through ultrasonication. The catalyst ink was then spray-coated onto a reinforced perfluorosulfonic acid (PFSA) membrane (12 μm thickness) using a Sono-Tek ultrasonic spray system to form a catalyst-coated membrane (CCM).

For a fair comparison, cell components and fabrication conditions were the same in all MEAs except for the cathode catalysts. Accordingly, the MEAs were labeled by the cathode catalysts.

The anode catalyst was the commercial 10% Pt/C with platinum group metal (PGM) loading fixed to be 0.01 $mg_{PGM}/cm^2$. The anode ionomer to carbon mass ratio was 0.6. The commercial 40% Pt/C (c-Pt/C) and 40% PtCo/C (c-PtCo/C) were used as benchmark of cathode catalyst. The ionomer to carbon ratio was 0.6 for c-Pt/C and c-PtCo/C, while 0.7 for $CoO_x$@Pt/C. The cathode catalyst loading was controlled to be about 0.09 $mg_{PGM}/cm^2$. The PGM loading on anode/cathode were confirmed by the ICP-AES measurements. The fabricated CCM was dried under vacuum for an hour to evaporate the solvents. For the MEA fabrication, two gas diffusion layers (GDLs), two PTFE gaskets, and the prepared CCM were pressed together. The thickness of the PTFE gasket is 127 μm (5 mil). The thickness of GDL, which includes a microporous layer, is 175 μm (Freudenberg H14C7).

**MEA activity tests**

The MEA was loaded in Fuel Cell Technology 5 $cm^2$ or 25 $cm^2$ single-cell fixture and tested in the Scribner 850e fuel cell test stand. Firstly, MEA activation was conducted by holding the voltage at 0.5 V under $H_2$/Air flow of 100/100 standard cubic centimeters per minute (sccm) for 5 $cm^2$ cell and 500/500 sccm for 25 $cm^2$ cell at 80 °C, 100% relative humidity (RH), 150 $kPa_{abs}$ (all pressure noted in this work refer to the absolute pressure) until the current reached plateau (usually about 30 minutes). Then, the MEA was further activated at oversaturated conditions, where the fuel temperate was set at 80 °C for both cathode and anode before entering the cell (hold at 60 °C). The mass activity (MA) tests were at 80 °C, 100% RH, 150 $kPa_{abs}$ with a flow rate of 835 ($H_2$)/2000 ($O_2$) sccm.

The rated power at BOL and EOL was tested in Scribner 850e fuel cell fixture under 94 °C, 250 $kPa_{abs,}$ and 100% RH.[9] The $H_2$/Air gas flow rate was 126/400 sccm for 5 $cm^2$ cell and 630/2000 sccm for 25 $cm^2$ cell, equivalent to the stoichiometry of 1.5/2.0 at 2.4 $A/cm^2$ (endpoint of current

density plot). The DOE has set a heat-rejection limit of $Q/\Delta T_i$ <1.45 for light-duty vehicles, assuming 90 kW stack gross power ($P_{stack}$) required for 80 kW net power and ambient temperature of 40 °C as the baseline. Power density at rated voltage ($V_{rated}$) is defined as the rated power, which is the maximum power aligned with heat management capability. The rated voltage is defined by equation 1 (Eq. 1)[9].

$$\frac{Q}{\Delta T_i} = \frac{P_{stack}(1.25 - V_{rated})}{V_{rated}(T_{stack} - T_{ambient})} \qquad \text{Eq. 1}$$

The DOE protocol assumes $P_{stack}$ = 90 kW and $T_{ambient}$ =40 °C, if $T_{stack}$ =94 °C, $Q/\Delta T_i$ =1.445, which meets the target ($Q/\Delta T_i$ of ≤1.45), the $V_{rated}$ will be around 0.67 V. Thus, the rated power will be measured at 0.67 V.[9]

All of the MEA's BOL and EOL performance metrics, such as MA, ECSA, and $H_2$ crossover, were recorded by the Scribner 850e fuel cell test station and the Scribner 885 potentiostat. The ECSA was determined by integrating the CO stripping peak, assuming 420 $\mu C/cm^2_{Pt}$. The CO stripping test in MEA followed the protocol in the literature.[10]

For the accelerated degradation test (ADT), we adopted the more aggressive 30,000-cycle square wave protocol with each cycle holding the MEA at the voltage of 0.6 V for 3 seconds and then 0.95 V for 3 seconds. The full ADT is carried at 80 °C, ambient pressure, 100% RH with $H_2/N_2$ flow 100/100 sccm for anode and cathode, respectively. We noted that our ADT protocol strictly followed the DOE protocol for PGM-based catalysts.[11, 12]

**Computational Studies**

Density-Functional Global Optimizations (DF-GO) simulations were performed employing the Basin Hopping (BH) algorithm [16,17] as implemented in an in-house python code. In each BH step, starting from a given locally relaxed initial structure, defined by 3N atomic coordinates

(where N is the number of atoms in the cluster), the GO algorithm generates a new configuration via a random perturbation of the coordinates which is then subjected to a local geometry optimization, after which the new configuration is accepted or rejected according to a Metropolis criterion, i.e., with probability min(1,exp(ΔE/T), where ΔE is the energy difference between the initial and the new locally relaxed configurations and T is a fictitious temperature (in our simulations varying between 3500 and 5000 K). The procedure starts from a sample of 3N arbitrary or selected atomic coordinates and iteratively continues with the random generation of new local minima starting from the currently accepted one, eventually providing a putative Global Minimum (GM) as the lowest-energy configuration. All the local minima, which belong to a DFT-PBE[18] Potential Energy Hyper-Surface (PES), were generated employing the OPENMX code[19], which solves the Kohn-Sham equations within the pseudopotential-LCAO framework by using localized pseudo-atomic numerical basis sets[20], whereas the Hartree potential is evaluated with the aid of a fast FFT solver, which relies on the use of a plane-wave basis set whose size depends on a chosen cut-off energy[21]. In our simulations, the Kohn-Sham energies were evaluated by feeding OPENMX with 'Quick'-type basis sets, norm-conserving pseudopotentials, and an energy cutoff of 150 Ry [22].

Starting from the OPENMX DF-GO database, a more accurate approach was used to predict energies and atomic equilibrium configurations by local geometry relaxation of candidate low-energy GO structures using the plane-wave Quantum Espresso (QE) code[24]. All the energies reported in the main text refer to the QE approach. The QE calculations were conducted spin unrestricted at the DFT/PBE level augmented with both Grimme-D3 dispersion and Hubbard-U corrections (U=3.5 eV for Co and U=0.0 for the other atomic species). We employed a cut-off energy of 40 Ry for describing the wave functions, a cut-off energy of 200 Ry for describing the

electron density, and GBRV ultra-soft pseudopotentials[25]. Work functions were evaluated according to the procedure proposed in literature[26,27]. Transmission Electron Microscopy (TEM) images were simulated using the QSTEM code[28].

### 4.3 Results and discussion

#### Structure of $CoO_x$@Pt/C core-shell nanocatalysts.

The designed $CoO_x$@Pt/C core-shell nanocatalysts were prepared by mixing carbon support with platinum acetylacetonate ($Pt(acac)_2$) and cobalt acetylacetonate ($Co(acac)_2$) in acetone under stirring, followed by evaporation of the solvent to obtain a dried powder mixture. The mixture was then annealed at 250 ℃ under Ar atmosphere and followed by an acid washing and annealing treatment at 180 ℃ to produce the final catalysts (see Methods). The scanning transmission electron microscopy (STEM) and high-resolution transmission electron microscopy (HRTEM) images reveal that the resulted $CoO_x$@Pt/C product (Figure 4. 2a and Figure 4. 3a) are uniformly dispersed on the carbon support with average diameters of 1.5 ± 0.2 nm (Figure 4. 2a inset). Powder X-ray diffraction (XRD) studies show a similar XRD pattern to that of the commercial Pt (c-Pt/C) and commercial PtCo (c-PtCo/C) catalysts with a face-centered cubic (fcc) structure (Figure 4. 3b). We see a notably broader peak in the XRD pattern, based on which we can estimate an average size of 1.5 nm, consistent with microscopic size analysis (Figure 4. 3c).

The composition analysis via inductively coupled plasma atomic emission spectroscopy (ICP-AES) shows that the $CoO_x$@Pt/C has a Co:Pt atomic ratio of 4.7:95.3. The energy dispersive X-ray spectroscopies (EDS) reveal a consistent Co:Pt ratio of 4.9:95.1, and the spatially resolved EDS mapping shows that the Co content is sparsely dispersed inside the nanoparticle (Figure 4. 2b). Interestingly, X-ray photoelectron spectroscopy (XPS) analysis of the $CoO_x$@Pt/C shows no Co 2p peak (Figure 4. 2c), indicating an essentially pure metallic Pt shell (Figure 4. 4). This is not

surprising considering the acid washing process could remove most surface $CoO_x$ species, and the remaining $CoO_x$ is likely fully enclosed by the Pt shell and thus less sensitive to surface-sensitive XPS studies. Indeed, the Co 2p peak (consistent with $Co^{2+}$) emerged after removing the surface atomic layer by in-situ $Ar^+$ etching (Figure 4. 2c and Figure 4. 5), confirming that the resulting material has a core-shell structure with the $CoO_x$ clusters embedded in a Pt shell.

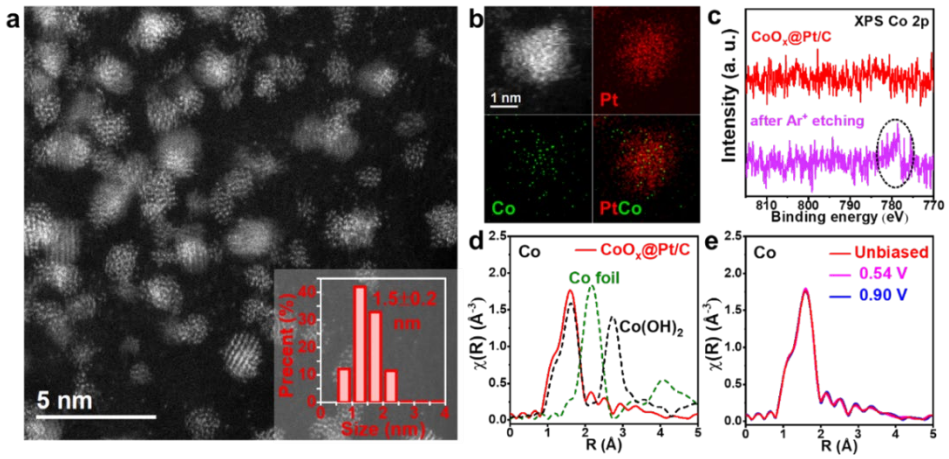


**Figure 4. 2** Synthesis and structural characterization of CoOx@Pt supported on carbon. (a) HAADF STEM images of the CoOx@Pt/C nanocatalyst. Inset: corresponding size distributions and the averaged size measured in particle diameter. (b) HAADF STEM image and corresponding EDS elemental maps with red representing Pt and green representing Co. (c) XPS depth profiling with spectra of Co 2p for CoOx@Pt/C before and after Ar+ etching. In situ Fourier transform EXAFS of CoOx@Pt/C collected at Co edge: (d) unbiased spectrum (red solid line) compared with Co foil (green dot line) and Co(OH)2 (black dot line) references; and (e) potential dependent spectra compared with unbiased one, showing unchanged signals under varied applied potentials.

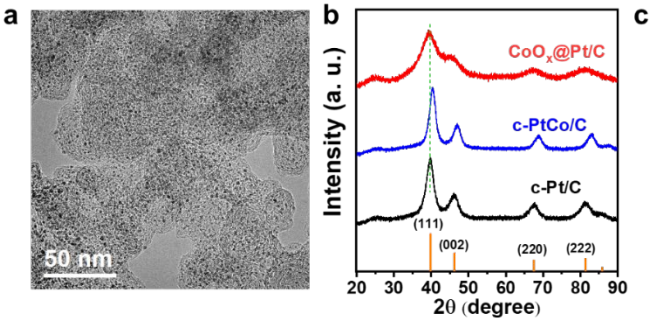


| Catalyst | XRD | |
|---|---|---|
| | FWHM | Size |
| c-Pt/C | 2.36° | 3.68 nm |
| c-PtCo/C | 1.94° | 4.51 nm |
| $CoO_x$@Pt/C | 5.65° | 1.51 nm |

**Figure 4. 3** TEM and XRD characterizations. (a) TEM image of the $CoO_x$@Pt/C catalyst. (b) XRD patterns and (c) the averaged XRD size of $CoO_x$@Pt, and benchmarking commercial c-Pt/C, c-PtCo catalysts. They were calculated from the full width at half maximum (FWHM) of the XRD peaks using the Scherrer equation.

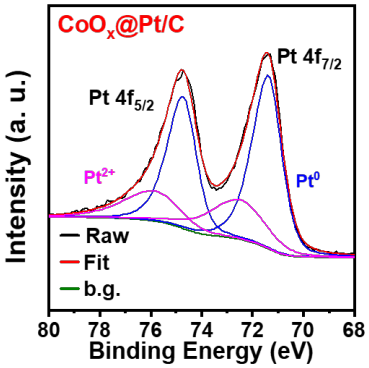


**Figure 4. 4** XPS spectra and its fitting of Pt 4f $CoO_x$@Pt/C.

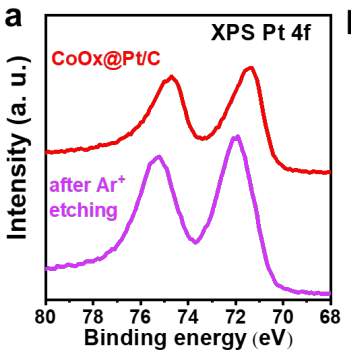


b

| Sample | Relative atomic ratio based on XPS (%) | |
|---|---|---|
| | Pt | Co |
| $CoO_x$@Pt/C | 100 | 0 |
| After $Ar^+$ etching | 93.4 | 6.6 |

**Figure 4. 5** $Ar^+$ etching depth profiling. (a) XPS Pt 4f spectra of $CoO_x$@Pt and $Ar^+$-etched $CoO_x$@Pt. (b) the weight percent of Pt and Co based on the integration of corresponding XPS peaks.

We further conducted in-situ X-ray absorption spectroscopy (XAS) studies in 0.1 M $HClO_4$ aqueous solution to understand the local atomistic and electronic structures (Figure 4. 2d and e). The Pt $L_3$-edge X-ray absorption near-edge structure (XANES) spectra show that the majority of Pt is in the metallic phase (Figure 4. 6a). The extended X-ray absorption fine structure (EXAFS) fitting result gives a Pt-Pt bond length of 2.74 Å (Figure 4. 6b and c, Table 4. 1), which is 1.4% smaller than that in bulk Pt (2.78 Å in Pt foil), suggesting the existence of compressive strain that is beneficial for ORR[8, 37]. The Co K-edge XANES result confirms the Co(II) oxidation state (Figure 4. 7). Importantly, the Co EXAFS and fitting results show a single Co-O peak with a coordination number of 6 ± 1, with no obvious Co-Co and Co-O-Co interactions (Figure 4. 2d,

Table 4. 2), indicating atomically dispersed $Co(II)O_6$ clusters. Moreover, the Co K-edge is independent of the applied potentials (Figure 4. 2e and Figure 4. 7b), suggesting the $Co(II)O_6$ clusters are well-protected inside the nanoparticles and do not directly interact with electrolytes. Meanwhile, the intensity of Pt-O interaction reduced with decreasing potential from 0.90 V to 0.54 V, which is consistent with the desorption of oxygenated species on Pt surface in this potential regime (Figure 4. 8a and c). Interestingly, a clear Pt-O interaction remains at 0.54 V (Figure 4. 8c, red arrow) where the electrode surface is presumably free of oxygenated adsorbates (Figure 4. 8d red arrow, Table 4. 2) [38]. Such remaining Pt-O interaction is attributable to the interaction between Pt atoms and the embedded $Co(II)O_6$ species. These combined STEM-EDS, XPS, and in-situ XAS characterizations robustly demonstrate the formation of a unique design of ultrafine Pt nanocatalysts with embedded atomically dispersed $Co(II)O_6$ clusters well-protected by the Pt shell.

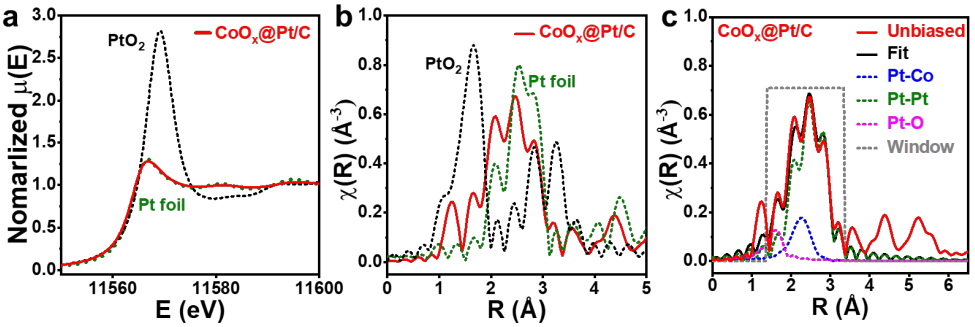


**Figure 4. 6** The *in-situ* X-ray absorption (XAS) spectra of $CoO_x$@Pt/C at Pt $L_3$-edge without applied potential (Unbiased). (a) X-ray absorption near-edge structure (XANES) spectra, and (b) Fourier transform extended X-ray absorption fine structure (EXAFS) spectra with references noted as Pt foil (green dot line) and $PtO_2$ (black dot line). (c) Fitting of the Fourier transform EXAFS spectrum. The *in-situ* data were collected in 0.1 M $HClO_4$ electrolyte without applied potential (unbiased).

| Sample | Relative Atomic Ratio (%) | | | | | |
|---|---|---|---|---|---|---|
| | Based on ICP-AES | | Based on XPS | | Based on EDS | |
| | Pt | Co | Pt | Co | Pt | Co |
| $CoO_x$@Pt/C | 95.3 | 4.7 | 100 | 0 | 95.1 | 4.9 |

| | | | | | | |
|---|---|---|---|---|---|---|
| c-PtCo/C | 75.0 | 25.0 | 70.7 | 29.3 | 73.6 | 26.4 |

**Table 4. 1** Atomic ratios of Pt and Co in catalysts measured by ICP-AES, XPS, and EDS.

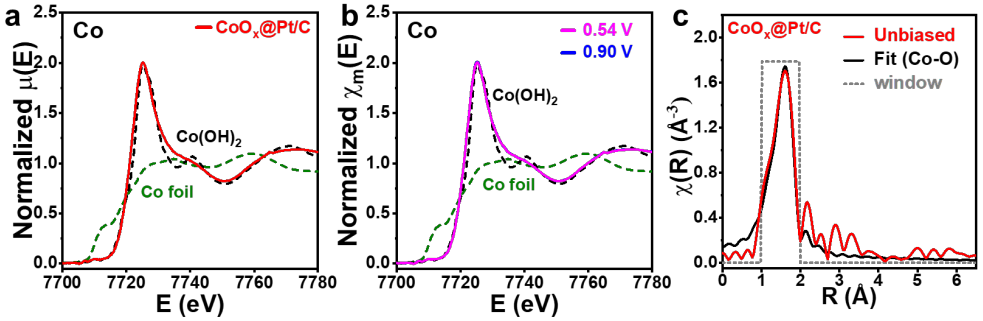


**Figure 4. 7** The *in-situ* X-ray absorption (XAS) spectra of $CoO_x$@Pt/C at Co K-edge. XANES spectrum (a) without applied potential (unbiased), and (b) under 0.54 V and 0.90 V. (c) Fitting of the unbiased Fourier transform EXAFS spectrum. The *in-situ* data were collected in 0.1 M $HClO_4$ electrolyte without applied potential (unbiased), at 0.54 V, and 0.90 V versus RHE.

| Pt $L_3$-edge EXAFS fitting | | | | | | |
|---|---|---|---|---|---|---|
| Sample | Scattering path | CN | R (Å) | $\sigma^2$ ($10^{-3}$ Å$^2$) | $E_0$ (eV) | R factor |
| $CoO_x$@Pt/C unbiased | Pt-Pt | 6±1 | 2.74±0.01 | 7±1 | 7±1 | 0.01 |
| | Pt-Co | 0.8±0.7 | 2.61±0.03 | 8±8 | | |
| | Pt-O | 0.4±0.3 | 2.02±0.03 | 4±7 | | |
| $CoO_x$@Pt at 0.54 V | Pt-Pt | 7±1 | 2.74±0.01 | 7±1 | 8±1 | 0.01 |
| | Pt-Co | 0.3±0.4 | 2.61±0.03 | 2±7 | | |
| | Pt-O | 0.4±0.2 | 2.00±0.03 | 0.3±3 | | |
| Commercial Pt/C at 0.54 V | Pt-Pt | 9.2±0.7 | 2.755±0.003 | 5.9±0.6 | 7.8±0.5 | 0.006 |
| | Pt-O | - | - | - | | |
| Co K-edge EXAFS fitting | | | | | | |
| Sample | Scattering path | CN | R (Å) | $\sigma^2$ ($10^{-3}$ Å$^2$) | $E_0$ (eV) | R factor |
| $CoO_x$@Pt/C unbiased | Co-O | 6±1 | 2.08±0.01 | 5±2 | -2±1 | 0.010 |

**Table 4. 2** Summaries of structural parameters extracted from *in-situ* EXAFS fitting of $CoO_x$@Pt at the Pt $L_3$-edge and Co K-edge and commercial Pt/C reference. CN is the coordination number; R is the interatomic distance (the bond length between Pt or Co central atoms and surrounding coordination atoms); $\sigma^2$ is the Debye-Waller factor (a measure of thermal and static disorder in absorber-scatterer distances); $E_0$ is edge-energy shift (the difference between the zero kinetic energy value of the sample and that of the theoretical model). R factor is used to value the goodness of the fitting.

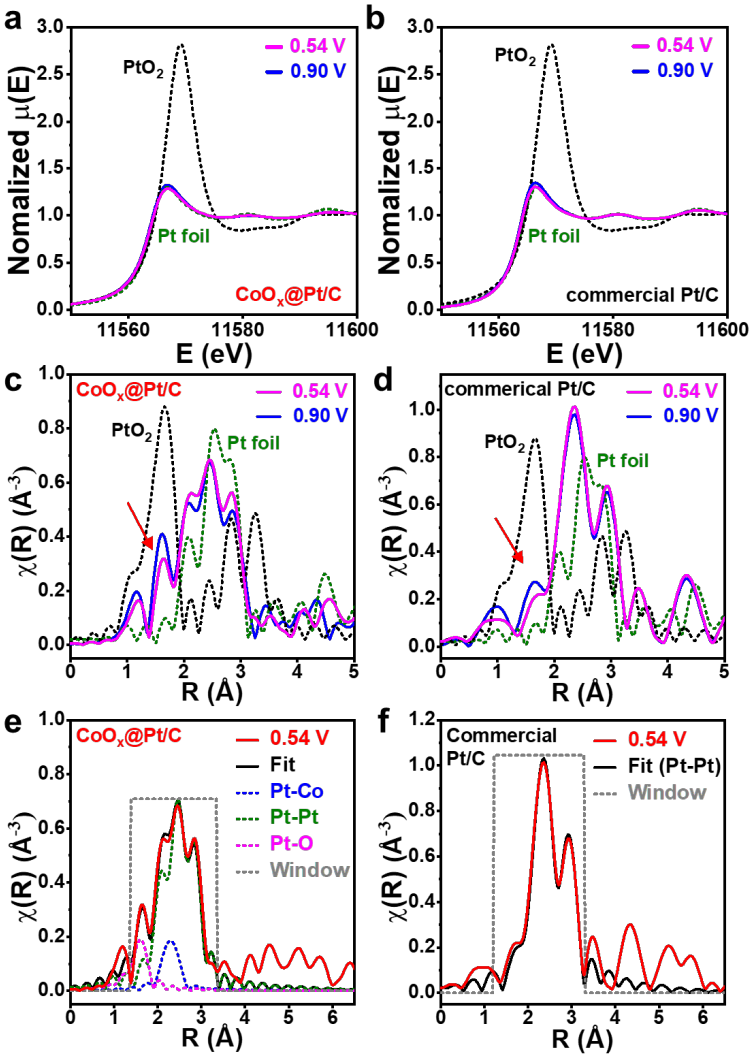


**Figure 4. 8** The *in-situ* XAS spectra of $CoO_x$@Pt/C and reference commercial Pt/C at the Pt $L_3$-edge. *In-situ* XANES spectra at 0.54 V and 0.90 V of (a) $CoO_x$@Pt/C, and (b) commercial Pt/C. *In-situ* Fourier transform EXAFS spectra at 0.54 V and 0.90 V of (c) $CoO_x$@Pt/C, and (d) commercial Pt/C. Fitting of the Fourier transform EXAFS spectrum at 0.54 V of (e) $CoO_x$@Pt/C, and (f) commercial Pt/C; noted that no Pt-O interaction is observed at 0.54 V in the commercial Pt/C, which suggests that the existence of Pt-O interaction at 0.54 V in the $CoO_x$@Pt/C catalyst is from the interaction with the embedded $CoO_x$.

**Fuel cell performance**

The practical fuel cell performance of the $CoO_x$@Pt/C was evaluated in a 5 $cm^2$ single-cell fuel cell fixture. The MEA was prepared by directly coating the catalyst ink on the proton exchange membrane using the ultrasonic spray at the cathode loading of 0.09 $mg_{PGM}/cm^2$ and anode loading

of 0.01 $mg_{PGM}/cm^2$ (see Methods). The performance is benchmarked against commercial c-Pt/C and c-PtCo/C under identical conditions. Notably, the $CoO_x$@Pt/C exhibits an initial MA of 1.10 $A/mg_{PGM}$ (Figure 4. 9a), considerably higher than those of the c-Pt/C (0.34 $A/mg_{PGM}$), c-PtCo (0.57 $A/mg_{PGM}$) and DOE target (0.44 $A/mg_{PGM}$). Furthermore, the $CoO_x$@Pt/C retains 88.2% of its initial MA after the aggressive square wave ADT (Figure 4. 9a), which is much higher than the 22.5% and 36.8% MA retentions observed in c-Pt/C and c-PtCo, respectively. It represents the state-of-the-art MA retention achieved in the demanding square wave ADT test (Table 4. 3) [39]. Significantly, the end-of-life (EOL) MA (0.97 $A/mg_{PGM}$) is 3.7 times of the DOE target (0.264 $A/mg_{PGM}$), 4.6 times the c-PtCo/C catalyst (0.21 $A/mg_{PGM}$), and 13.1 times of the c-Pt/C catalysts (0.07 $A/mg_{PGM}$), and represents the highest EOL MA reported in MEA tests to date (Table 4. 3) [23-27, 40-42].

While the MA test under pure oxygen evaluates the intrinsic activity of catalysts with little impact from mass transport issues, the rated power measured in the $H_2$-air test directly reflects the practical performance. The $H_2$-air fuel cell with $CoO_x$@Pt/C catalyst delivers a rated power of 1.04 $W/cm^2$, outperforming those with c-Pt/C (0.88 $W/cm^2$) and c-PtCo (0.92 $W/cm^2$) (Figure 4. 9b), and exceeding the DOE target of 1.0 $W/cm^2$. In addition, a useful metric to evaluate the PGM utilization in fuel cells is to normalize the power by the total PGM loading ($W/mg_{PGM}$). In this regard, the $CoO_x$@Pt/C MEA delivers a high Pt utilization of 10.4 $W/mg_{PGM}$ (Figure 4. 9c), well above the DOE target (8.0 $W/mg_{PGM}$). Furthermore, the $CoO_x$@Pt/C demonstrated notably better performance than c-Pt/C or c-PtCo/C throughout the entire current density regime (Figure 4. 9d and e). These power performances of the $CoO_x$@Pt/C are among the best reported performance for Pt-based catalysts (Table 4. 3). More importantly, the $CoO_x$@Pt/C exhibits a record high EOL

rated power (Pt utilization) of 0.96 W/cm$^2$ (9.6 W/mg$_{PGM}$) (Figure 4. 9b, Table 4. 3), far higher than those of c-Pt/C (0.32 W/cm$^2$, 3.2 W/mg$_{PGM}$) and c-PtCo (0.61 W/cm$^2$, 6.1 W/mg$_{PGM}$).

The stability can be further evaluated by the voltage loss at a given current density (e.g., 0.8 A/cm$^2$). The DOE 2020 target suggested a voltage loss <30 mV at 0.8 A/cm$^2$. When comparing the BOL and EOL polarization curves, the $CoO_x$@Pt/C exhibits superior durability greatly outperforming the c-Pt/C or c-PtCo, with only 13.3 mV loss at 0.8 A/cm$^2$ (Figure 4. 9f), which is substantially smaller than that of Pt/C (162.5 mV) or c-PtCo/C (61.3 mV). Moreover, there was only a slight drop throughout the entire curve after the ADT for $CoO_x$@Pt/C (Figure 4. 9f), even in the more challenging HCD region (*e.g.*, 11.1 mV loss at 1.0 A/cm$^2$ and 12.0 mV loss at 1.25 A/cm$^2$), clearly highlighting the exceptional stability of the $CoO_x$@Pt/C catalysts. With a high MA retention of 88.2% and remarkably low rated power loss of 7.5%, the $CoO_x$@Pt/C nanocatalyst represents the first catalyst satisfying both MA and the more challenging power durability targets (light green area in Figure 4. 9g). It is interesting to note that such a small voltage loss in the HCD region can be translated into an extraordinary projected lifetime of around 15,000 hours (see Methods), which is three times of the DOE 2020 target (5,000 hours) for light-duty transportation applications [4].

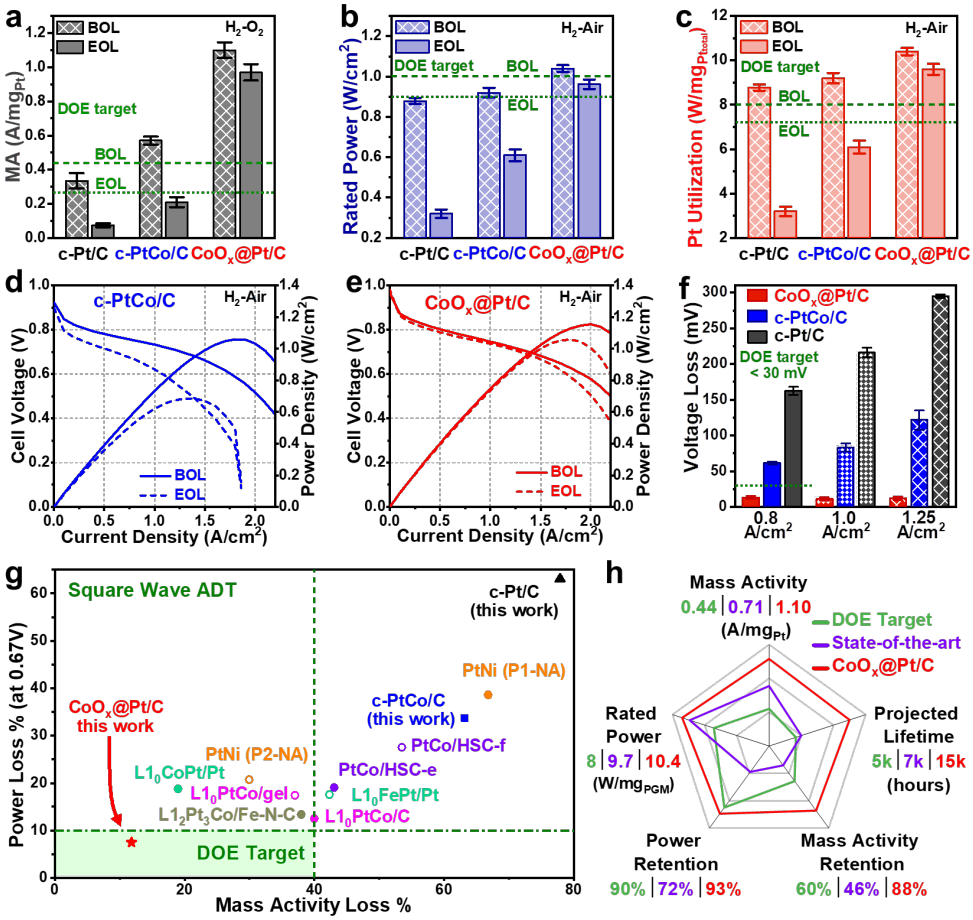


**Figure 4. 9** MEA performance of $CoO_x$@Pt/C, commercial PtCo (c-PtCo/C), commercial Pt/C (c-Pt/C. (a) Comparison of mass activity (MA) obtained in $H_2/O_2$ tests at the beginning of life (BOL; before ADT) and end of life (EOL; after ADT). Comparison of (b) rated power density and (c) Pt utilization obtained in $H_2$/air tests at BOL and EOL. DOE targets are represented by green dash (BOL) and green dot (EOL) lines. (d, e) Polarization plots (left axis) and power density plots (right axis) of (d) c-PtCo/C and (e) $CoO_x$@Pt/C obtained in $H_2$/air tests at BOL and EOL, highlighting extraordinary power performance and stability of the MEA with $CoO_x$@Pt/C. (f) Voltage loss at current density of 0.8, 1.0 and 1.25 mA/cm$^2$. (g) The comparison of MA loss and power loss between $CoO_x$@Pt/C and the state-of-the-art catalysts reported in the literature: PtCo/HSC-e, PtCo/HSC-f [24]; PtNi P1-NA, PtNi P2-NA [23]; $L1_0$PtCo/C, $L1_0$PtCo/gel [42]; $L1_0$CoPt/Pt, $L1_0$FePt/Pt [27]; $L1_2Pt_3$Co/Fe-N-C [25]. It highlights that $CoO_x$@Pt/C is the only catalyst that can meet both durability targets (light green square). The $CoO_x$@Pt/C represents the only catalyst simultaneously satisfying the MA loss and power loss target. (h) The comparison of major fuel cell performance metrics among DOE target, the state-of-the-art catalyst (PtCo/HSC-e/f DOE selected as current status reference) [4, 24], and the $CoO_x$@Pt/C in this work.

| Catalyst | Total Loading ($mg_{Pt}$ $cm^{-2}$) | Mass Activity ($A/mg_{Pt}$) | | MA Retention (%) | ADT Condition | Power@0.67V ($W/cm^2$) | | Rated Power Loss (%) | Pt utilization ($kW_{rated}/g_{Pt}$) | | Potential Loss at 0.8 $A/cm^2$ (mV) |
|---|---|---|---|---|---|---|---|---|---|---|---|
| | | BOL | EOL | | | BOL | EOL | | BOL | EOL | |
| DOE 2020 Target[4] | ≤ 0.125 | > 0.44 | > 0.264 | > 60 | Square Wave | >1.0 | >0.9 | <10 | > 8 | > 7.2 | <30 |
| Pt/C **(this work)** | 0.10 | 0.335 ±0.045 | 0.074 ±0.012 | 22.5 | Square Wave | 0.878 ±0.014 | 0.320 ±0.021 | 63.6 | 8.8 | 3.2 | 162.5 ±5.7 |
| c-PtCo/C **(this work)** | 0.10 | 0.570 ±0.023 | 0.21 ±0.028 | 36.8 | Square Wave | 0.92 ±0.024 | 0.61 ±0.029 | 33.7 | 9.2 | 6.1 | 61.3±1.3 |
| **$CoO_x$@Pt/C (this work)** | **0.10** | **1.10 ±0.046** | **0.970 ±0.048** | **88.2** | **Square Wave** | **1.040 ±0.017** | **0.962 ±0.025** | **7.5** | **10.4** | **9.6** | **13.3 ±1.8** |
| PtNi (P1-NA)[23] | 0.15 | 0.50 | 0.17 | 33.2 | Triangle Wave | 0.75* | 0.46* | 38.6 | 5.0 | 3.1 | 58* |
| PtNi (P2-NA)[23] | 0.15 | 0.63 | 0.44 | 70.0 | Triangle Wave | 0.75* | 0.59* | 20.7 | 5.0 | 3.9 | 39* |
| PtCo/HSC-e[24] | 0.125 | 0.65 | 0.37 | 56.9 | Square Wave | 1.10* | 0.889* | 19.0 | 9.27 | 7.5 | 20* |
| PtCo/HSC-f[24] | 0.125 | 0.71 | 0.33 | 46.5 | Square Wave | 1.22* | 0.886* | 27.5 | 10.4 | 7.4 | 20* |
| $L1_0$-CoPt/Pt[27] | 0.205 | 0.56 | 0.45 | 81.0 | Square Wave | 0.52* | 0.42* | 18.8 | 2.5 | 2.0 | 70* |
| $L1_0$-FePt/Pt[27] | 0.22 | 0.29 | 0.17 | 57.7 | Square Wave | 0.50* | 0.41* | 17.6 | 2.3 | 1.9 | 38* |
| $L1_2$ $Pt_3Co$/FeNC[25] | 0.20 | 0.72 | 0.44 | 62 | Square Wave | 0.83* | 0.72* | 13.4 | 4.2 | 3.6 | 21 |
| $L1_0$-PtCo[42] | 0.206 | 0.6 | 0.36 | 60.0 | Square Wave | 0.89 | 0.78* | 12.5 | 4.3 | 3.8 | 26 |
| $L1_0$-PtCo /Hydrogel[42] | 0.208 | 0.79 | 0.498 | 63.0 | Square Wave | 0.77 | 0.63* | 17.4 | 3.7 | 3.0 | 31 |
| i-NPs PtCo[28] | 0.10 (0.04)[a] | 1.52 | NA | 77[b] | Triangle Wave | 0.45* | NA | NA | 11.3 | NA | NA |
| i-NPs PtFe[28] | 0.10 (0.04)[a] | 1.27 | NA | 79[b] | Triangle Wave | 0.35* | NA | NA | 8.7 | NA | NA |
| PtCo/C3[40] | 0.15 | 0.72 | 0.44 | 61 | Square Wave | 1.16 | NA | NA | 7.7 | NA | 16.9 |
| LP@PF-1[41] | 0.383 | 1.08 | 0.67 | 62 | Triangle Wave | NA | NA | NA | NA | NA | NA |
| LP@PF-2[41] | 0.385 | 1.77 | 0.26 | 15 | Triangle Wave | NA | NA | NA | NA | NA | NA |

**Table 4. 3** Comparison of key fuel cell performance metrics with the state-of-the-art catalysts. Notably, the MEA with $CoO_x$@Pt/C catalyst exceeds all DOE performance metrics and shows the highest EOL performances, highlighting its extraordinary activity and durability. *: value extracted from performance plots. [a]: the total loading of 0.10 mg/cm$^2$ is for $H_2$-$O_2$ test and 0.04 mg/cm$^2$ is for $H_2$-Air test. [b]: MA retention value is recorded from a different MEA with a thicker membrane.

To the best of our knowledge, our catalyst represents the only catalyst with both BOL and EOL performance metrics simultaneously exceeding the DOE targets (Figure 4. 9h, Table 4. 3)[18, 43-44]. It should be highlighted that although many advanced catalyst designs have led to impressive BOL performance previously, durability has been a persistent challenge and the EOL performance is generally far from satisfactory [41, 44]. In particular, there is no report of catalyst system that can deliver a rated power retention of 90 % and MA retention of 60% while satisfying all BOL performance metrics set in DOE targets [4]. As the fuel cells must meet performance requirements throughout their service lifetime, the EOL instead of BOL performance ultimately determines the amount of Pt needed [2]. In this regard, the exceptional EOL performance achieved in our design is particularly important for enabling PEMFCs with substantially reduced lifetime-adjusted cost in practical applications.

**Understanding of the exceptional durability**

We have analyzed the nanocatalyst size distribution before and after the ADT in MEA (Figure 4. 10a, b, Figure 4. 11, Figure 4. 12, and Table 4. 4). Overall, the size of c-Pt/C increased dramatically from 3.5 ± 0.8 nm at BOL to 7.2 ± 3.6 nm at EOL (Figure 4. 11a-d and Figure 4. 12), and a similar size growth was also observed in c-PtCo/C (from 4.7 ± 1.4 nm at BOL to 8.1 ± 3.5 nm at EOL) (Figure 4. 10b and Figure 4. 11e-h). Such a substantial size increase can be attributed to (i) nanoparticle detachment, movement, and coalescence, and (ii) oxidative dissolution, diffusion, and Ostwald ripening process[19]. In contrast, the average size of the $CoO_x$@Pt/C only increased moderately from 1.5 ± 0.2 nm at BOL to 2.5 ± 1.2 nm at EOL (Figure 4. 10a, Figure 4. 11i-l). Similarly, the $CoO_x$@Pt catalyst exhibits a considerably higher EOL ECSA (35.9 ± 0.9 $m^2/g_{PGM}$) from CO stripping experiments at 80°C in MEAs than those of commercial Pt (8.9 ± 1.8 $m^2/g_{PGM}$) and PtCo alloy (12.3 ± 1.0 $m^2/g_{PGM}$) catalysts (Table 4. 4). These analyses clearly

highlight the benefit of our design to effectively restrain the size growth and improve the overall durability. In particular, the embedded $CoO_x$ strengthens the interactions with surface Pt atoms due to the strong metal-oxide interaction, greatly slowing down the oxidation and dissolution of surface Pt atoms and retarding the Ostwald ripening process (Figure 4. 1). This stabilization effect is supported by the simulation results to be discussed later.

In addition to size analyses, the EDS composition analyses also confirm that the Co content of $CoO_x$@Pt nanoparticles was well retained during the ADT with a minor decrease from 4.9 at.% at BOL to 4.5 at.% at EOL (Figure 4. 10c, Figure 4. 13, Table 4. 5), with the Co content remaining sparsely embedded inside the nanoparticle (Figure 4. 14). In contrast, there was a drastic composition change from 26.4 at.% to 9.8 at.% in the c-PtCo nanoparticles (Fig. 4c, Figure 4. 13, Table 4. 5), indicating substantial leaching of Co cations that may cause considerable loss in intrinsic activity and cation poisoning effects on the mass transport and overall device performance.[20-21]

Moreover, CO stripping experiments were also used to probe the change in the chemisorption behavior of different catalysts. Previous studies have shown that the lower the peak potential of CO oxidation, the weaker the CO binding strength, which indicates a lower Pt *d*-band center and weaker oxygen adsorption energy favorable for ORR kinetics [45]. Interestingly, after the ADT, both c-Pt/C and c-PtCo/C show a notable shift to higher binding energy, while such a shift is not observed in the $CoO_x$@Pt/C (Figure 4. 10d), indicating the retainment of the favorable weak oxygen adsorption characteristics for excellent EOL performance.

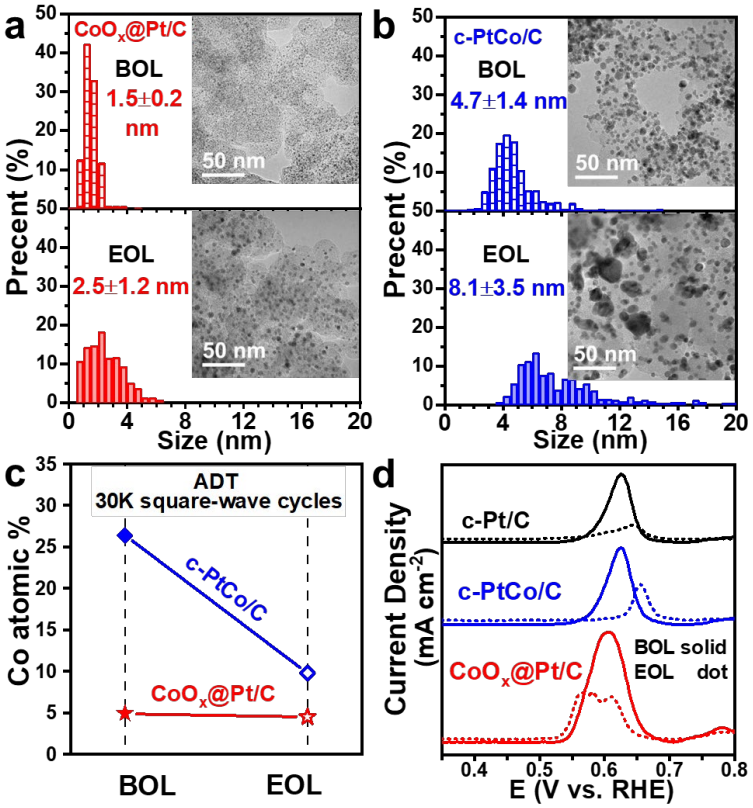


**Figure 4. 10** Size, composition and CO stripping analyses of catalysts at BOL and EOL. Histogram of particle size distribution at BOL and EOL (a) $CoO_x$@Pt/C and (b) c-PtCo/C catalysts. The inset shows the corresponding TEM images. (c) The change of Co atomic composition based at BOL and EOL. (d) Comparison of CO stripping experiments at 80°C in MEAs, showing the change of oxidation peaks at BOL (solid lines) and EOL (dotted lines) of the commercial and $CoO_x$@Pt/C catalysts.

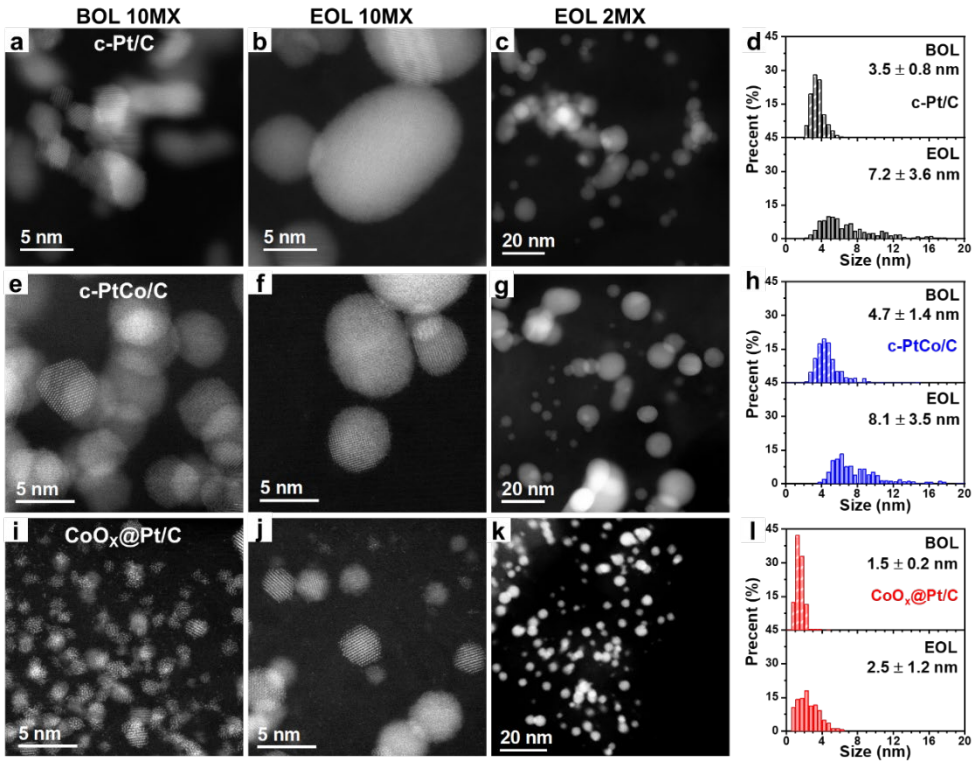


**Figure 4. 11** STEM images and size distribution at both BOL and EOL. (a-d) c-Pt/C. (e-h) c-PtCo/C. (i-l) $CoO_x$@Pt/C.

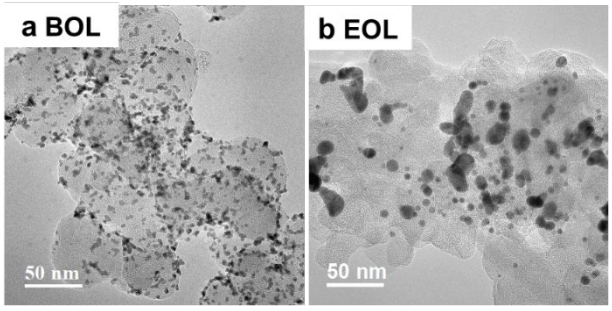


**Figure 4. 12** TEM images of c-Pt/C catalysts at BOL and EOL.

| Sample | Size (nm) | | ECSA ($m^2/g_{PGM}$) | | |
|---|---|---|---|---|---|
| | BOL | EOL | BOL | EOL | loss (%) |
| c-Pt/C | 3.5 ± 0.8 | 7.2 ± 3.6 | 31.8 ± 1.9 | 8.9 ± 1.8 | 72.0 |
| c-PtCo/C | 4.7 ± 1.4 | 8.1 ± 3.5 | 37.4 ± 1.1 | 12.3 ± 1.0 | 67.1 |
| **$CoO_x$@Pt/C** | **1.5 ± 0.2** | **2.5 ± 1.2** | **73.1 ± 1.5** | **35.9 ± 0.9** | **50.9** |

**Table 4. 4** Comparison of Pt nanoparticle size and ECSA at both BOL and EOL tested in MEA.

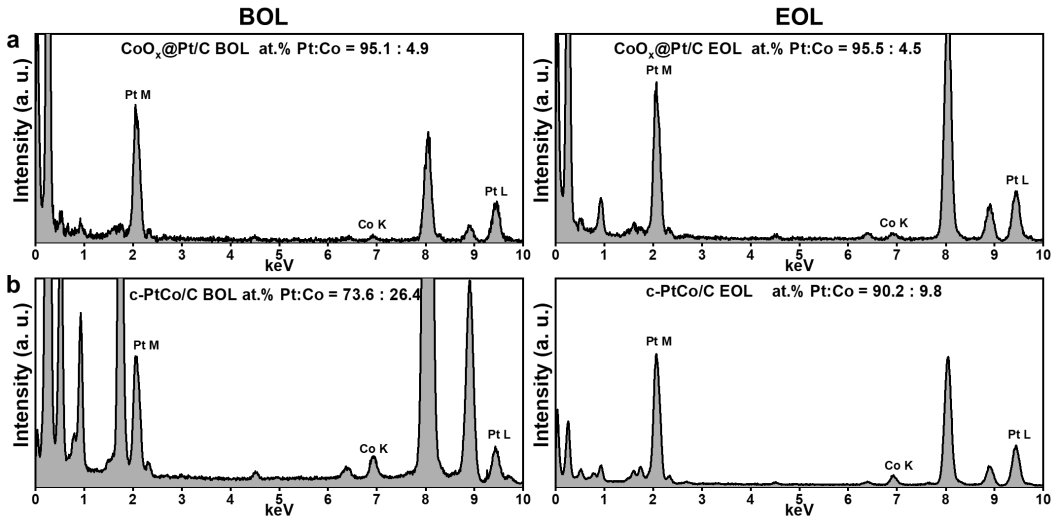


**Figure 4. 13** EDS spectra of catalysts at BOL and EOL. (a) $CoO_x$@Pt/C. (b) c-PtCo/C.

| sample | EDS Co atomic ratio (%) | |
|---|---|---|
| | BOL | EOL |
| $CoO_x$@Pt/C | 4.9 | 4.5 |
| c-PtCo/C | 26.4 | 9.8 |

**Table 4. 5** The averaged atomic ratio (at. %) of Co (Co:Pt) measured by EDS at BOL and EOL of MEA tests.

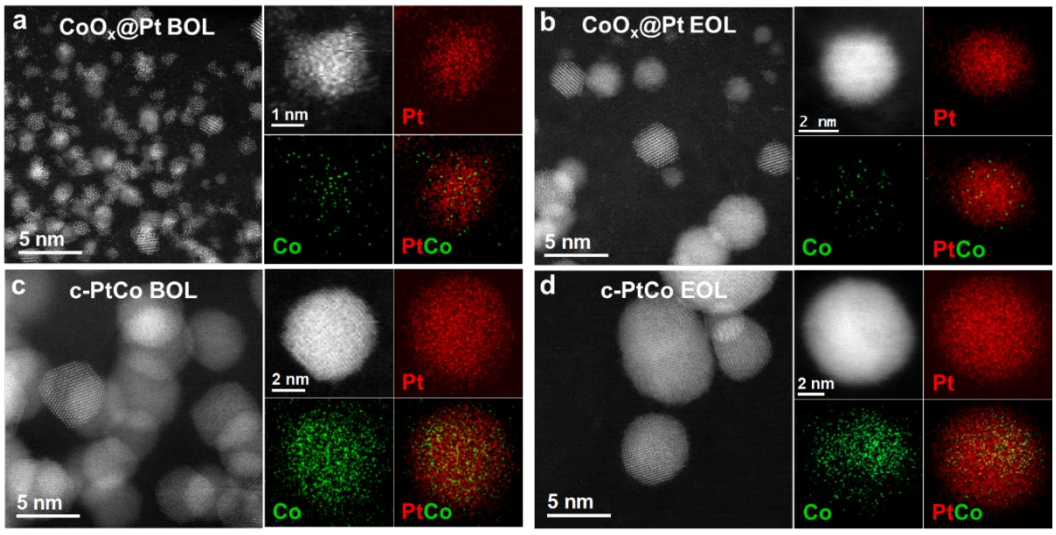


**Figure 4. 14** Characterization of catalysts at BOL and EOL, HAADF STEM, and corresponding EDS elemental mappings of (a-b) $CoO_x$@Pt/C. (c-d) c-PtCo/C.

To further understand the fundamental origin of their exceptional stability, we computationally predicted the atomistic configurations, energetics, and electronic structure of the ultrafine Pt nanoparticles with endohedral $CoO_x$ clusters to compare their thermodynamic and kinetic stability with pure Pt and PtCo alloy nanoparticles. We focused on the size large enough to accommodate a single $CoO_x$ unit (typically, $CoO_6$, see below) with a complete shell of Pt atoms, around 80 atoms. Our calculations indicated that the preferred stoichiometry of the $CoO_x$ unit was $CoO_6$ (Figure 4. 15), in agreement with experimental EXAFS studies.

No rigorous information exists in the literature on the atomistic configurations of Pt-based nanoparticles in this size regime, not even pure Pt, which must be predicted *ab initio*. We therefore performed extensive Density-Functional Global Optimization (DF-GO) [46] on nanoparticles with different atom numbers and stoichiometry, to determine their Global Minimum (GM) configurations, the corresponding energetics, electronic structure, and interaction with oxygen adatoms (see Methods). Interestingly, our DF-GO studies reveal that the most stable structure in this size range (e.g., $Pt_{78}$, $Pt_{77}Co$, and $Pt_{77}CoO_6$) typically exhibits a barrel-like structural motif (Figure 4. 16, Figure 4. 17), which is energetically more stable by several eV with respect to other motifs, such as the truncated octahedron $Pt_{79}$ with a closed-shell crystalline-like Wulff shape (Figure 4. 18). Moreover, the Lowdin analysis reveals a positive charge of +0.45 on Co atoms, which compares well with the Lowdin charge of +0.39 for Co in bulk CoO, consistent with $Co^{2+}$ status observed in XAS studies (Figure 4. 6b). We also note that the predicted oxygen and platinum coordination numbers of Pt (evaluated with a cut-off distance of 3.00 Å) are 0.21 and 6.23, in agreement with the experimental values of 0.4 ±0.3 and 6 ± 1, respectively (Table 4. 2).

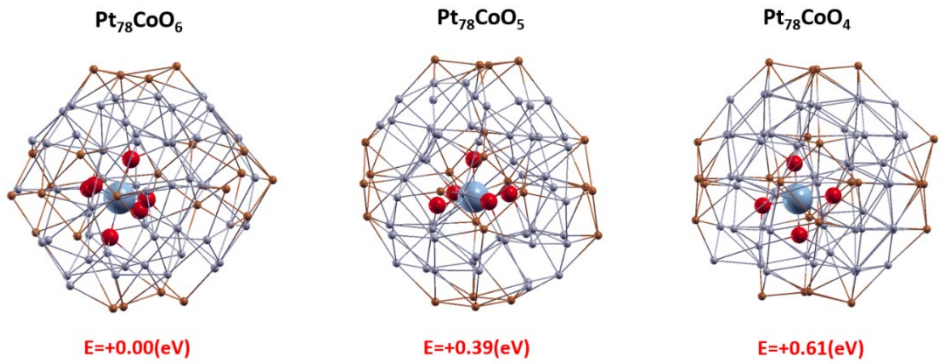


**Figure 4. 15** Energetics of initial structures of $Pt_{78}CoO_x$ clusters generated from the TO configuration with different oxygen content (x). Note the increase in energy when reducing the oxygen content of the $Pt_{79}CoO_6$ cluster (whose initial configuration was obtained encapsulating an octahedral $CoO_6$ unit inside a $Pt_{79}$ Truncated Octahedron structure). Note that the encapsulation of $CoO_x$ inside the host Pt structure strongly deforms the initial TO shape where Pt atoms belonging to 100 facets (reddish brown color in the figure) and 111 facets can hardly be singled out.

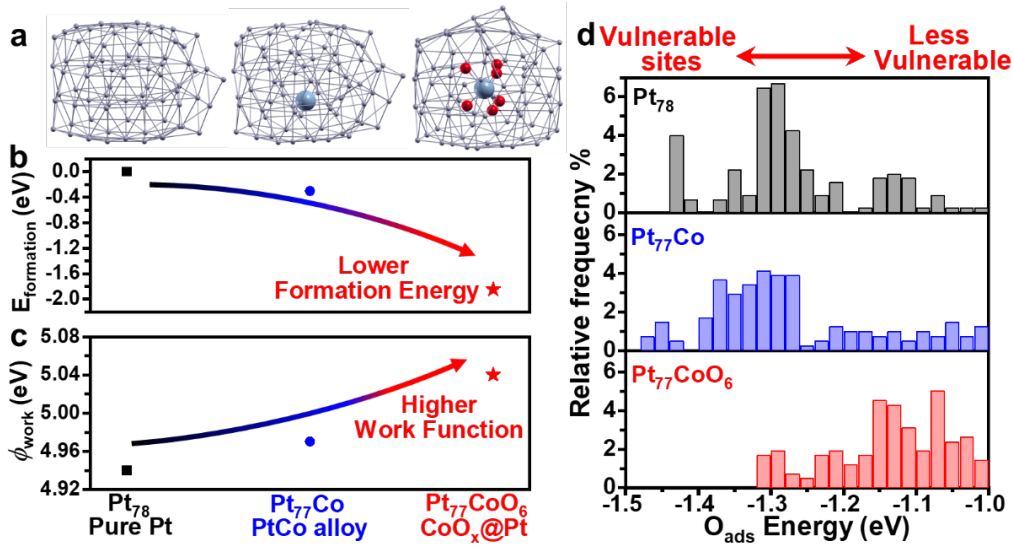


**Figure 4. 16** Simulation results for the Global Mimumum (GM) configurations of pure Pt, PtCo alloy, and $CoO_x$@Pt clusters with similar size. (a) Atomistic configurations: $Pt_{78}$, $Pt_{77}Co$, and $Pt_{77}CoO_6$. (b, c) Comparison of the formation energy $E_{formation}$ (b) and the work function $\phi$ (c) of the GM clusters, indicating the $CoO_x$@Pt is thermodynamically and kinetically the most stable. (d) Distribution of oxygen adsorption energy at surface sites, showing that $CoO_x$@Pt has fewer sites with strong oxygen adsorption energy that are kinetically vulnerable to oxidative dissolution.

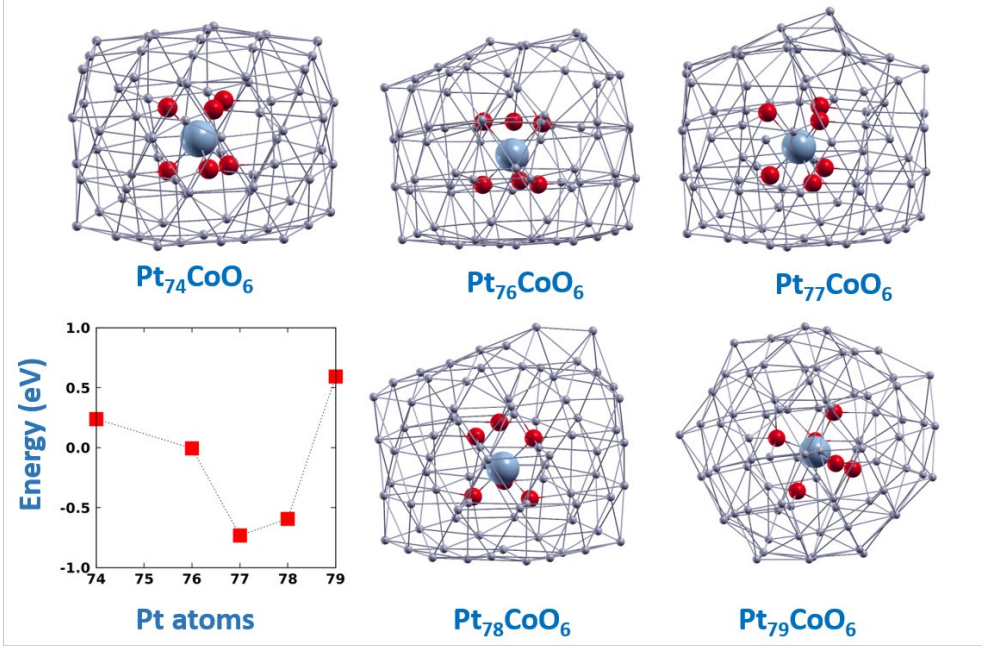


**Figure 4. 17** Schematic atomistic configurations and relative energetics of $Pt_{79-x}CoO_6$ GM clusters as derived from DF-GO simulations. The figure shows the GM structures obtained by varying the number of Pt atoms in $Pt_nCoO_6$ clusters, together with the corresponding formation energies (red squares in the graph on the left-bottom-panel) calculated taking as a reference Pt chemical potential the energy per atom of Pt in the $Pt_{79}$ cluster. All the minima, except $Pt_{79}$, clearly show a barrel-like shape in which top-Pt atoms tail-off by reducing the Pt content, finally leading to a $Pt_{74}CoO_6$ symmetric cylindrical structure. The energy trend shown in the left-bottom-panel indicates that maximum stability is achieved for the cluster with composition $Pt_{77}CoO_6$.

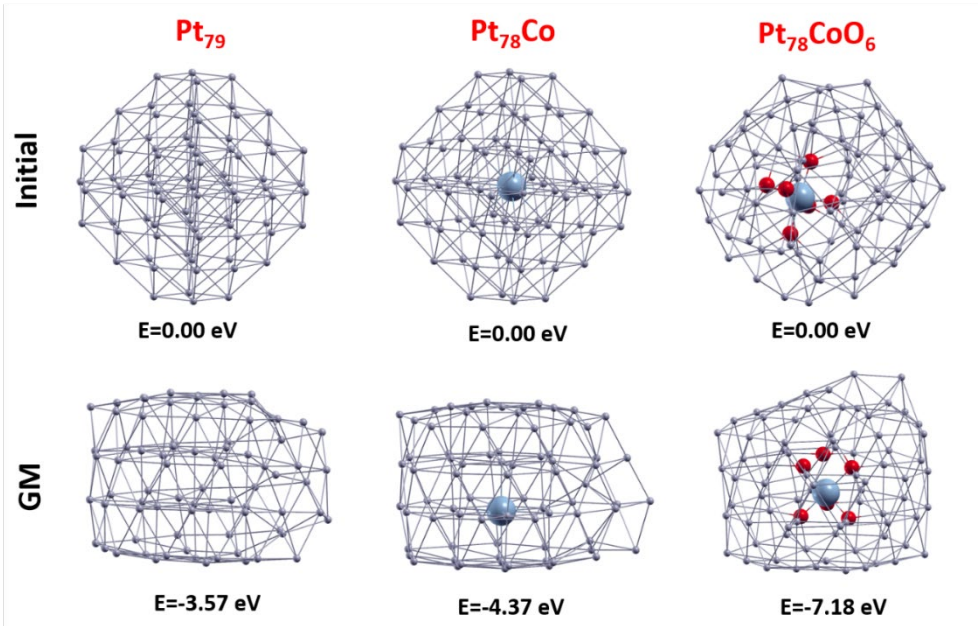


**Figure 4. 18** Energy stabilization of initial crystalline-like (truncated octahedra, TO) structures of $Pt_{79}$, $Pt_{78}Co$, and $Pt_{78}CoO_6$ clusters to the final ("barrel-like-motif") configurations. We report

atomistic configurations of the putative GM of $Pt_{79}$, $Pt_{78}Co$ and $Pt_{78}CoO_6$ clusters and the energy differences between the starting and the GM structures. The initial configurations were generated by relaxing the crystalline TO structure. Note that all the GM minima exhibit a quasi-cylindrical "barrel-like" structure, deformed sideways in the case of pure Pt and PtCo alloy or bearing Pt protruding species on top of one (111) facet in the case of $Pt_nCoO_x$. Note that the stabilization energies increase in absolute value after alloying or subsequent oxidation of the pure Pt cluster, showing on the one hand the effectiveness of the GO algorithm in exploring the PES of the system, and on the other hand indicating that structural stress in the Pt TO structure increase with nestling the Co species at the center and favor the Co oxidation.

More importantly, our calculation shows that the free energy of the Pt nanoparticle with endohedral $CoO_6$ ($Pt_{77}CoO_6$) is 1.85 and 1.55 eV lower than that of pure Pt ($Pt_{78}$) and PtCo alloy ($Pt_{77}Co$) structures with a similar size (Figure 4. 16b), respectively. We have further calculated the work function of these structures and found the order: $Pt_{78}$ (4.94 eV) < $Pt_{77}Co$ (4.97 eV) < $Pt_{77}CoO_6$ (5.04 eV) (Figure 4. 16c), which correlates well with the experimentally observed order of stability under bias (Figure 4. 9). Indeed, the nanocatalysts need to adjust their work function via oxygen adsorption and/or adding positive charge so that their work function equalizes with the target electrode potential under operating conditions (e.g., 0.90-0.95 V) [47]. A larger work function implies a lower positive charge density and makes the cluster less liable to oxidation, which contributes to improved stability against oxidative dissolution.

Next, we further explored the relative kinetic stability of these clusters under ORR conditions. Previous studies have revealed that the Pt dissolution during fuel cell operation mainly goes through an oxidative/reductive dissolution mechanism [3]. Therefore, we have calculated the oxygen adsorption energies on the surface sites of $Pt_{78}$, $Pt_{77}Co$, and $Pt_{77}CoO_6$ nanocatalysts to probe the kinetics of Pt dissolution. It is interesting to note that both $Pt_{78}$ and $Pt_{77}Co$ alloy have a considerably higher population of surface sites with stronger oxidation adsorption energy (Figure 4c, black and blue), which are considered to be more vulnerable sites, i.e., more prone to oxidation and oxidative dissolution.[32, 48-49] In contrast, the surface Pt sites on $Pt_{77}CoO_6$ generally show

weaker oxygen adsorption energy and thus have a higher kinetic barrier for oxidative dissolution (Figure 4. 16, red). Overall, these calculations explain the exceptional stability of the $CoO_x$@Pt/C against the oxidative dissolution of surface Pt atoms and the Oswald ripening process, which further prevents the embedded $CoO_x$ from leaching out, as observed in experiment (Figure 4. 10).

**4.4 Conclusion**

Overall, by embedding near atomically dispersed $CoO_x$ clusters inside ultrafine Pt nanoparticles to induce strong metal-oxide interaction against both size and composition degradation, we have created a unique design of ultrafine $CoO_x$@Pt/C nanocatalysts. Both experiments and simulations corroborate the existence of a set of $CoO_x$-endohedral-doped Pt nanoparticles with unique thermodynamic stability and reduced tendency to oxidative dissolution. This $CoO_x$@Pt/C nanocatalysts show remarkable fuel cell performance, delivering a high MA of 1.10 $A/g_{PGM}$, a high power density of 1.04 $W/cm^2$ at a low total PGM loading of 0.1 $mg_{Pt}/cm^2$, an unprecedentedly MA retention of 88.2%, and power retention of 92.5% after the aggressive 30,000 cycles of square wave ADT, all exceeding the current state-of-the-art catalysts and the relevant DOE targets for the first time. The remarkable power retention performance projects a record-breaking fuel cell lifetime of 15,000 hours. Lastly, we should note that the atomically dispersed $CoO_x$ species embedded in the Pt nanoparticle are conceptually distinct from conventional oxide supported catalysts. Our design takes advantage of the strong metal-oxide interaction while avoiding the common drawbacks of the oxide as a support, such as oxide dissolution and low conductivity. Considering fuel cell system cost and lifetime represent the two major roadblocks, our study presents a major leap in fuel cell catalyst development and holds significant potential for improving the commercial viability of PEMFCs, particularly for heavy-duty applications.

## 4.5 References


1. Debe, M. K., Electrocatalyst approaches and challenges for automotive fuel cells. *Nature* **2012,** *486*, 43-51.

2. Cullen, D. A.; Neyerlin, K. C.; Ahluwalia, R. K.; Mukundan, R.; More, K. L.; Borup, R. L.; Weber, A. Z.; Myers, D. J.; Kusoglu, A., New roads and challenges for fuel cells in heavy-duty transportation. *Nature Energy* **2021,** *6* (5), 462-474.

3. Kodama, K.; Nagai, T.; Kuwaki, A.; Jinnouchi, R.; Morimoto, Y., Challenges in applying highly active Pt-based nanostructured catalysts for oxygen reduction reactions to fuel cell vehicles. *Nature Nanotechnology* **2021,** *16* (2), 140-147.

4. *Fuel cell technologies office multi-year research, development, and demonstration plan*; U.S. Department of Energy, 2017.

5. Lohse-Busch, H.; Stutenberg, K.; Duoba, M.; Liu, X.; Elgowainy, A.; Wang, M.; Wallner, T.; Richard, B.; Christenson, M., Automotive fuel cell stack and system efficiency and fuel consumption based on vehicle testing on a chassis dynamometer at minus 18 °C to positive 35 °C temperatures. *Int J Hydrogen Energ* **2020,** *45* (1), 861-872.

6. *Average Annual Vehicle Miles Traveled by Major Vehicle Category*; EERE Alternative Fuels Data Center: https://afdc.energy.gov/data/, 2020.

7. Li, M.; Zhao, Z.; Cheng, T.; Fortunelli, A.; Chen, C.-Y.; Yu, R.; Zhang, Q.; Gu, L.; Merinov, B. V.; Lin, Z.; Zhu, E.; Yu, T.; Jia, Q.; Guo, J.; Zhang, L.; Goddard, W. A.; Huang, Y.; Duan, X., Ultrafine jagged platinum nanowires enable ultrahigh mass activity for the oxygen reduction reaction. *Science* **2016,** *354* (6318), 1414-1419.

8. Escudero-Escribano, M.; Malacrida, P.; Hansen, M. H.; Vej-Hansen, U. G.; Velázquez-Palenzuela, A.; Tripkovic, V.; Schiøtz, J.; Rossmeisl, J.; Stephens, I. E. L.; Chorkendorff, I.,

Tuning the activity of Pt alloy electrocatalysts by means of the lanthanide contraction. *Science* **2016,** *352* (6281), 73-76.

9. Chen, C.; Kang, Y.; Huo, Z.; Zhu, Z.; Huang, W.; Xin, H. L.; Snyder, J. D.; Li, D.; Herron, J. A.; Mavrikakis, M.; Chi, M.; More, K. L.; Li, Y.; Markovic, N. M.; Somorjai, G. A.; Yang, P.; Stamenkovic, V. R., Highly crystalline multimetallic nanoframes with three-dimensional electrocatalytic surfaces. *Science* **2014,** *343* (6177), 1339-1343.

10. Zhang, L.; Roling, L. T.; Wang, X.; Vara, M.; Chi, M.; Liu, J.; Choi, S.-I.; Park, J.; Herron, J. A.; Xie, Z.; Mavrikakis, M.; Xia, Y., Platinum-based nanocages with subnanometer-thick walls and well-defined, controllable facets. *Science* **2015,** *349* (6246), 412-416.

11. Seh, Z. W.; Kibsgaard, J.; Dickens, C. F.; Chorkendorff, I.; Nørskov, J. K.; Jaramillo, T. F., Combining theory and experiment in electrocatalysis: Insights into materials design. *Science* **2017,** *355* (6321), eaad4998.

12. Li, W.; Chen, Z.; Xu, L.; Yan, Y., A solution-phase synthesis method to highly active Pt-Co/C electrocatalysts for proton exchange membrane fuel cell. *Journal of Power Sources* **2010,** *195* (9), 2534-2540.

13. Wang, X. X.; Hwang, S.; Pan, Y.-T.; Chen, K.; He, Y.; Karakalos, S.; Zhang, H.; Spendelow, J. S.; Su, D.; Wu, G., Ordered Pt3Co intermetallic nanoparticles derived from metal–organic frameworks for oxygen reduction. *Nano Letters* **2018,** *18* (7), 4163-4171.

14. Huang, L.; Zheng, C. Y.; Shen, B.; Mirkin, C. A., High-index-facet metal-alloy nanoparticles as fuel cell electrocatalysts. *Advanced Materials* **2020,** *32* (30), 2002849.

15. Ge, Y.; Wang, X.; Huang, B.; Huang, Z.; Chen, B.; Ling, C.; Liu, J.; Liu, G.; Zhang, J.; Wang, G.; Chen, Y.; Li, L.; Liao, L.; Wang, L.; Yun, Q.; Lai, Z.; Lu, S.; Luo, Q.; Wang, J.; Zheng, Z.; Zhang, H., Seeded Synthesis of Unconventional 2H-Phase Pd Alloy Nanomaterials for Highly

Efficient Oxygen Reduction. *Journal of the American Chemical Society* **2021,** *143* (41), 17292-17299.

16. Liu, H.; Zhong, P.; Liu, K.; Han, L.; Zheng, H.; Yin, Y.; Gao, C., Synthesis of ultrathin platinum nanoplates for enhanced oxygen reduction activity. *Chemical Science* **2018,** *9* (2), 398-404.

17. Liu, Z.; Zhao, Z.; Peng, B.; Duan, X.; Huang, Y., Beyond Extended Surfaces: Understanding the Oxygen Reduction Reaction on Nanocatalysts. *Journal of the American Chemical Society* **2020,** *142* (42), 17812-17827.

18. Zhao, Z.; Chen, C.; Liu, Z.; Huang, J.; Wu, M.; Liu, H.; Li, Y.; Huang, Y., Pt-based nanocrystal for electrocatalytic oxygen reduction. *Advanced Materials* **2019,** *31* (31), 1808115.

19. Borup, R. L.; Kusoglu, A.; Neyerlin, K. C.; Mukundan, R.; Ahluwalia, R. K.; Cullen, D. A.; More, K. L.; Weber, A. Z.; Myers, D. J., Recent developments in catalyst-related PEM fuel cell durability. *Current Opinion in Electrochemistry* **2020,** *21*, 192-200.

20. Braaten, J. P.; Xu, X.; Cai, Y.; Kongkanand, A.; Litster, S., Contaminant Cation Effect on Oxygen Transport through the Ionomers of Polymer Electrolyte Membrane Fuel Cells. *Journal of The Electrochemical Society* **2019,** *166* (16), F1337-F1343.

21. Dumont, J. H.; Baker, A. M.; Maurya, S.; Kim, Y. S.; Mukundan, R.; Myers, D. J.; Borup, R. L., Effect of Cerium, Cobalt and Nickel Contaminants on the Oxygen Reduction Reaction at Platinum Electrodes. *ECS Transactions* **2017,** *80* (8), 861-867.

22. Cai, Y.; Kongkanand, A.; Gu, W.; Moylan, T. E., Effects of Cobalt Cation on Low Pt-loaded PEM Fuel Cell Performance. *ECS Transactions* **2015,** *69* (17), 1047-1061.

23. Han, B.; Carlton, C. E.; Kongkanand, A.; Kukreja, R. S.; Theobald, B. R.; Gan, L.; O'Malley, R.; Strasser, P.; Wagner, F. T.; Shao-Horn, Y., Record activity and stability of dealloyed

bimetallic catalysts for proton exchange membrane fuel cells. *Energy & Environmental Science* **2015,** *8* (1), 258-266.

24. Ko, M.; Padgett, E.; Yarlagadda, V.; Kongkanand, A.; Muller, D. A., Revealing the Nanostructure of Mesoporous Fuel Cell Catalyst Supports for Durable, High-Power Performance. *Journal of The Electrochemical Society* **2021,** *168* (2), 024512.

25. Qiao, Z.; Wang, C.; Li, C.; Zeng, Y.; Hwang, S.; Li, B.; Karakalos, S.; Park, J.; Kropf, A. J.; Wegener, E. C.; Gong, Q.; Xu, H.; Wang, G.; Myers, D. J.; Xie, J.; Spendelow, J. S.; Wu, G., Atomically dispersed single iron sites for promoting Pt and Pt3Co fuel cell catalysts: performance and durability improvements. *Energy & Environmental Science* **2021,** *14* (9), 4948-4960.

26. Duan, X.; Cao, F.; Ding, R.; Li, X.; Li, Q.; Aisha, R.; Zhang, S.; Hua, K.; Rui, Z.; Wu, Y.; Li, J.; Li, A.; Liu, J., Cobalt-Doping Stabilized Active and Durable Sub-2 nm Pt Nanoclusters for Low-Pt-Loading PEMFC Cathode. *Advanced Energy Materials* **2022,** *12* (13), 2103144.

27. Li, J.; Sharma, S.; Liu, X.; Pan, Y.-T.; Spendelow, J. S.; Chi, M.; Jia, Y.; Zhang, P.; Cullen, D. A.; Xi, Z.; Lin, H.; Yin, Z.; Shen, B.; Muzzio, M.; Yu, C.; Kim, Y. S.; Peterson, A. A.; More, K. L.; Zhu, H.; Sun, S., Hard-magnet L10-CoPt nanoparticles advance fuel cell catalysis. *Joule* **2019,** *3* (1), 124-135.

28. Yang, C.-L.; Wang, L.-N.; Yin, P.; Liu, J.; Chen, M.-X.; Yan, Q.-Q.; Wang, Z.-S.; Xu, S.-L.; Chu, S.-Q.; Cui, C.; Ju, H.; Zhu, J.; Lin, Y.; Shui, J.; Liang, H.-W., Sulfur-anchoring synthesis of platinum intermetallic nanoparticle catalysts for fuel cells. *Science* **2021,** *374* (6566), 459-464.

29. Qiu, H. J.; Gao, J. J.; Wen, Y. R.; Shang, B.; Wang, J. Q.; Lin, X.; Wang, Y., Platinum Cluster/Nanoparticle on CoO Nanosheets with Coupled Atomic Structure and High Electrocatalytic Durability. *ACS Applied Energy Materials* **2018,** *1* (5), 1840-1845.

30. Xu, S.; Wang, Z.; Dull, S.; Liu, Y.; Lee, D. U.; Lezama Pacheco, J. S.; Orazov, M.; Vullum, P. E.; Dadlani, A. L.; Vinogradova, O.; Schindler, P.; Tam, Q.; Schladt, T. D.; Mueller, J. E.; Kirsch, S.; Huebner, G.; Higgins, D.; Torgersen, J.; Viswanathan, V.; Jaramillo, T. F.; Prinz, F. B., Direct Integration of Strained-Pt Catalysts into Proton-Exchange-Membrane Fuel Cells with Atomic Layer Deposition. *Advanced Materials* **2021,** *33* (30), 2007885.

31. Sievers, G. W.; Jensen, A. W.; Quinson, J.; Zana, A.; Bizzotto, F.; Oezaslan, M.; Dworzak, A.; Kirkensgaard, J. J. K.; Smitshuysen, T. E. L.; Kadkhodazadeh, S.; Juelsholt, M.; Jensen, K. M. Ø.; Anklam, K.; Wan, H.; Schäfer, J.; Čépe, K.; Escudero-Escribano, M.; Rossmeisl, J.; Quade, A.; Brüser, V.; Arenz, M., Self-supported Pt–CoO networks combining high specific activity with high surface area for oxygen reduction. *Nature Materials* **2021,** *20* (2), 208-213.

32. Zhu, E.; Wu, M.; Xu, H.; Peng, B.; Liu, Z.; Huang, Y.; Li, Y., Stability of Platinum-Group-Metal-based Electrocatalysts in Proton Exchange Membrane Fuel Cells. *Advanced Functional Materials* **2022,** *n/a* (n/a), 2203883.

33. Bertram, M.; Prössl, C.; Ronovský, M.; Knöppel, J.; Matvija, P.; Fusek, L.; Skála, T.; Tsud, N.; Kastenmeier, M.; Matolín, V.; Mayrhofer, K. J. J.; Johánek, V.; Mysliveček, J.; Cherevko, S.; Lykhach, Y.; Brummel, O.; Libuda, J., Cobalt Oxide-Supported Pt Electrocatalysts: Intimate Correlation between Particle Size, Electronic Metal–Support Interaction and Stability. *The Journal of Physical Chemistry Letters* **2020,** *11* (19), 8365-8371.

34. Zeng, Z.; Chang, K.-C.; Kubal, J.; Markovic, N. M.; Greeley, J., Stabilization of ultrathin (hydroxy)oxide films on transition metal substrates for electrochemical energy conversion. *Nature Energy* **2017,** *2* (6), 17070.

35. Schmies, H.; Bergmann, A.; Drnec, J.; Wang, G.; Teschner, D.; Kühl, S.; Sandbeck, D. J. S.; Cherevko, S.; Gocyla, M.; Shviro, M.; Heggen, M.; Ramani, V.; Dunin-Borkowski, R. E.;

Mayrhofer, K. J. J.; Strasser, P., Unravelling Degradation Pathways of Oxide-Supported Pt Fuel Cell Nanocatalysts under In Situ Operating Conditions. *Advanced Energy Materials* **2018,** *8* (4), 1701663.

36. Xu, C.; Yang, J.; Liu, E.; Jia, Q.; Veith, G. M.; Nair, G.; DiPietro, S.; Sun, K.; Chen, J.; Pietrasz, P.; Lu, Z.; Jagner, M.; Gath, K. K.; Mukerjee, S.; Waldecker, J. R., Physical vapor deposition process for engineering Pt based oxygen reduction reaction catalysts on NbOx templated carbon support. *Journal of Power Sources* **2020,** *451*, 227709.

37. Luo, M.; Guo, S., Strain-controlled electrocatalysis on multimetallic nanomaterials. *Nature Reviews Materials* **2017,** *2* (11), 17059.

38. Jia, Q.; Liang, W.; Bates, M. K.; Mani, P.; Lee, W.; Mukerjee, S., Activity Descriptor Identification for Oxygen Reduction on Platinum-Based Bimetallic Nanoparticles: In Situ Observation of the Linear Composition–Strain–Activity Relationship. *ACS Nano* **2015,** *9* (1), 387-400.

39. Stariha, S.; Macauley, N.; Sneed, B. T.; Langlois, D.; More, K. L.; Mukundan, R.; Borup, R. L., Recent Advances in Catalyst Accelerated Stress Tests for Polymer Electrolyte Membrane Fuel Cells. *Journal of The Electrochemical Society* **2018,** *165* (7), F492-F501.

40. Zhao, Z.; Hossain, M. D.; Xu, C.; Lu, Z.; Liu, Y.-S.; Hsieh, S.-H.; Lee, I.; Gao, W.; Yang, J.; Merinov, B. V.; Xue, W.; Liu, Z.; Zhou, J.; Luo, Z.; Pan, X.; Zaera, F.; Guo, J.; Duan, X.; Goddard, W. A.; Huang, Y., Tailoring a three-phase microenvironment for high-performance oxygen reduction reaction in proton exchange membrane fuel cells. *Matter* **2020,** *3* (5), 1774-1790.

41. Chong, L.; Wen, J.; Kubal, J.; Sen, F. G.; Zou, J.; Greeley, J.; Chan, M.; Barkholtz, H.; Ding, W.; Liu, D.-J., Ultralow-loading platinum-cobalt fuel cell catalysts derived from imidazolate frameworks. *Science* **2018,** *362* (6420), 1276-1281.

42. Spendelow, J. S. *Advanced Electro-Catalysts through Crystallographic Enhancement*; U.S. Department of Energy: https://www.hydrogen.energy.gov/pdfs/review19/fc161_spendelow_2019_o.pdf, 2019.

43. Yarlagadda, V.; Carpenter, M. K.; Moylan, T. E.; Kukreja, R. S.; Koestner, R.; Gu, W.; Thompson, L.; Kongkanand, A., Boosting fuel cell performance with accessible carbon mesopores. *ACS Energy Letters* **2018,** *3* (3), 618-621.

44. Zhao, Z.; Liu, Z.; Zhang, A.; Yan, X.; Xue, W.; Peng, B.; Xin, H. L.; Pan, X.; Duan, X.; Huang, Y., Graphene-nanopocket-encaged PtCo nanocatalysts for highly durable fuel cell operation under demanding ultralow-Pt-loading conditions. *Nature Nanotechnology* **2022**.

45. Nilsson, A.; Pettersson, L. G. M.; Hammer, B.; Bligaard, T.; Christensen, C. H.; Nørskov, J. K., The electronic structure effect in heterogeneous catalysis. *Catalysis Letters* **2005,** *100* (3), 111-114.

46. Aprà, E.; Ferrando, R.; Fortunelli, A., Density-functional global optimization of gold nanoclusters. *Physical Review B* **2006,** *73* (20), 205414.

47. Sundararaman, R.; Goddard, W. A.; Arias, T. A., Grand canonical electronic density-functional theory: Algorithms and applications to electrochemistry. *The Journal of Chemical Physics* **2017,** *146* (11), 114104.

48. Lopes, P. P.; Strmcnik, D.; Tripkovic, D.; Connell, J. G.; Stamenkovic, V.; Markovic, N. M., Relationships between Atomic Level Surface Structure and Stability/Activity of Platinum Surface Atoms in Aqueous Environments. *ACS Catalysis* **2016,** *6* (4), 2536-2544.

49. Huang, J.; Sementa, L.; Liu, Z.; Barcaro, G.; Feng, M.; Liu, E.; Jiao, L.; Xu, M.; Leshchev, D.; Lee, S.-J.; Li, M.; Wan, C.; Zhu, E.; Liu, Y.; Peng, B.; Duan, X.; Goddard, W. A.; Fortunelli,

A.; Jia, Q.; Huang, Y., Experimental Sabatier plot for predictive design of active and stable Pt-alloy oxygen reduction reaction catalysts. *Nature Catalysis* **2022,** *5* (6), 513-523.

## Chapter 5. Concluding remarks

The work presented in this dissertation is focused on exploring new catalyst design strategies for more efficient and stable ORR catalysts with the goal of integrating them into real-world applications. In my first work, we found that surface modification can change the behavior and concentration at the catalyst-electrolyte interface, which can promote the reaction and protect the catalysts, thus leading to activity enhancement and extension of the catalyst lifetime. It should be noted that this method is proven to be general and can be applied to different catalysts, and this idea opens new exciting avenues to further enhance activities for other catalytic reactions, like hydrogen oxidation reaction, $CO_2/N_2$ reduction reaction, etc. My second work represents one of our initial efforts to translate the promising RDE performance of advanced catalysts into practical fuel cells. We incorporated the highly promising Pt-alloy nanowires into practical MEA, showing excellent activity under stressing ultralow loading condition. In my third work, we designed a unique Pt nanoparticle with embedded cobalt oxide clusters, utilizing the strong interaction between Pt and oxide to mitigate metal dissolution. This new catalyst design addresses the durability and cost changes in fuel cell technology. By combing advanced characterization techniques and simulations, we have identified and rationalized several performance enhancement strategies of catalyst design principles. My PhD studies have helped to advance the development of cost-effective and durable Pt-based catalysts in hydrogen fuel cell technology, which I believe is crucial for a clean energy future.